Mesoscopic Modelling of Mechanically-Modulated Electrical Conductivity in Zinc Oxide Varistors

Taylor, Kyle Aaron

(2020)

Mesoscopic Modelling of Mechanically-Modulated Electrical Conductivity in Zinc Oxide Varistors

Mesoskopische Modellierung der mechanisch modulierten elektrischen Leitfähigkeit in Zinkoxidvaristoren

zur Erlangung des akademischen Grades Doktor-Ingenieur (Dr.-Ing.)

genehmigte Dissertation von Kyle Aaron Taylor aus Croydon, United Kingdom

Tag der Einreichung: 16. März 2020, Tag der mündlichen Prüfung: 15. Juni 2020

Darmstadt — D 17

1. Gutachten: PD Dr. rer. nat. Erion Gjonaj
2. Gutachten: Prof. Dr.-Ing. Herbert De Gersem
3. Gutachten: Prof. Dr. Jürgen Rödel

TECHNISCHE UNIVERSITÄT DARMSTADT

Mesoscopic Modelling of Mechanically-Modulated Electrical Conductivity in Zinc Oxide Varistors
Mesoskopische Modellierung der mechanisch modulierten elektrischen Leitfähigkeit
in Zinkoxidvaristoren

Genehmigte Dissertation von Kyle Aaron Taylor aus Croydon, United Kingdom

1. Gutachten: PD Dr. rer. nat. Erion Gjonaj
2. Gutachten: Prof. Dr.-Ing. Herbert De Gersem
3. Gutachten: Prof. Dr. Jürgen Rödel

Tag der Einreichung: 16. März 2020
Tag der mündlichen Prüfung: 15. Juni 2020
Jahr der Veröffentlichung der Dissertation auf TUprints: 2020

Technische Universität Darmstadt
Darmstadt — D 17

Erklärung laut Promotionsordnung

§8 Abs. 1 lit. c PromO

Ich versichere hiermit, dass die elektronische Version meiner Dissertation mit der schriftlichen Version übereinstimmt.

§8 Abs. 1 lit. d PromO

Ich versichere hiermit, dass zu einem vorherigen Zeitpunkt noch keine Promotion versucht wurde. In diesem Fall sind nähere Angaben über Zeitpunkt, Hochschule, Dissertationsthema und Ergebnis dieses Versuchs mitzuteilen.

§9 Abs. 1 PromO

Ich versichere hiermit, dass die vorliegende Dissertation selbstständig und nur unter Verwendung der angegebenen Quellen verfasst wurde.

§9 Abs. 1 PromO

Die Arbeit hat bisher noch nicht zu Prüfungszwecken gedient.

Darmstadt, den 16. März 2020,

Kyle Aaron Taylor

Kurzfassung

Diese Arbeit stellt ein elektromechanisch gekoppeltes Modell für die Simulation des elektrischen Stromflusses in Zinkoxidvaristoren vor. Das Modell basiert auf einer Ersatzschaltbildrepräsentation der Varistormikrostruktur, in welcher die Korngrenzen als nichtlineare Widerstände modelliert werden. Diese Vorgehensweise baut auf existierenden Schaltkreismodellen auf und erweitert sie durch die Berücksichtigung des Einflusses der mechanischen Spannungen auf die elektrische Leitfähigkeit der Korngrenzen. Die dreidimensionale mechanische Spannungsverteilung im Material wird mit der Finite-Elemente-Methode (FEM) berechnet. Anhand dieser Verteilung wird der elektrische Widerstand jeder Korngrenze bestimmt. Dies erfordert ein selbstkonsistentes Modell für die Grenzflächenladung, die durch piezoelektrische Polarisation induziert wird. Zum Schluss werden die Verteilung des elektrischen Stroms und Leitfähigkeit des gesamten Varistors mittels des nichtlinearen Schaltkreismodells berechnet.

Die simulierten Stromspannungscharakteristiken zeigen deutlich, dass die elektrische Leitfähigkeit von ZnO Varistoren stark von der angewandten mechanischen Spannung abhängig ist. Die Simulationen stellen außerdem den Effekt der Stromkonzentration entlang dünner hochleitfähiger Pfade dar. Dieser Effekt hängt von den mikrostrukturellen Eigenschaften sowie vom mechanischen Spannungszustand des Materials ab. Zusätzlich wird der Effekt residualer thermomechanischer Spannungen in polykristallinen Mikrostrukturen berücksichtigt und der Einfluss solcher Spannungen auf die Leitfähigkeit wird charakterisiert. Weiterhin werden der inverse piezoelektrische Effekt auf Korngrenzen und seine Auswirkung auf die makroskopische elektrische Charakteristik in der Arbeit untersucht.

Abstract

An electromechanically-coupled model for the simulation of electric current flow in zinc oxide varistors is presented. The model is based on an equivalent circuit representation of the varistor microstructure, where the grain boundaries are modelled as non-linear resistors in the circuit. This approach extends previous circuit models by including the effect of mechanical stress on grain boundary conductivity. The three-dimensional mechanical stress distribution in the material is calculated by the finite element method (FEM). Using this distribution, the electrical resistance of each grain boundary is determined by applying a self-consistent model for the trapped interface charge induced by piezoelectric polarisation. Finally, the electric current flow patterns and the bulk conductivity of the material are computed using a non-linear circuit model.

The simulated IV-characteristics reveal a significant sensitivity of electrical conductivity to applied stress. For 2D and 3D ZnO varistor models, the simulations demonstrate the effect of current concentration along thin conducting paths, depending on microstructural properties and on the mechanical stress condition of the material. The effect of residual thermal stress in polycrystalline structures on the electrical conductivity is also considered. Just as in the case of applied stress, the electrical conductivity is highly sensitive to the accumulation of thermal stress within the material. Furthermore, the effect of the inverse piezoelectric effect is examined and accounted for in the computation of the macroscopic varistor characteristics.

Contents

1 Introduction

Zinc oxide (ZnO) is a piezoelectric semiconducting ceramic, which has been used for decades as a functional material in a broad variety of engineering fields. Just a few examples of these are low-wavelength light-emitting diodes [1], solar-blind photodetectors [2] and transparent thin-film transistors [3]. One area of application that is of interest to this thesis is ZnO's role as a varistor, such as those used as components in voltage surge protectors for low-voltage electronic circuits [4] and power transmission lines [5]. The term varistor is a portmanteau of 'variable resistor', referring to the material's ability to change its resistance depending on the applied voltage. These components are connected in parallel to an external circuit so that, if a voltage surge occurs, the current will be redirected through the resistor as its total resistance falls below that of the vulnerable circuit. ZnO is the material of choice for varistor applications, and this is a consequence of its ability to rapidly absorb large amounts of electrical energy. This property is rooted in the material's diode-like current-voltage (IV) characteristic curve, which occurs due to the double Schottky barriers that form along the boundaries between individual ZnO grains within a polycrystal. These boundaries exhibit an electrical response equivalent to that of a back-to-back pair of Zener diodes [6] and are highly non-linear, displaying resistance jumps of several orders of magnitude that take place over a comparatively narrow voltage range.

For surge protection applications, this non-linearity is ZnO's greatest strength. The ability to almost instantaneously decrease resistance is, of course, invaluable when dealing with a sudden voltage surge. However, this effect leads to a strong current concentration effect in certain regions of the material [7]. Such inhomogeneous current distribution results in reduced energy absorption capacity, and, potentially, material failure if the component is operated in this voltage range for too long [8]. Market pressure to keep costs low and new technological challenges, such as ultra-high voltage networks, push these surge protection systems to their limits with ever increasing regularity. As such, a detailed understanding of their inner workings and failure mechanisms is vital.

Contemporary research into ZnO frequently concerns itself with the electromechanical tunability of the material. The ability to utilise applied mechanical stress to modulate ZnO's electrical conductivity arises from the piezotronic effect [9,10] and results from a stress-induced piezoelectric charge that modifies the height of potential barriers in semiconductor devices [11]. This occurs when the distribution of trapped interface charges at the grain boundaries

is modified by the strain-induced piezoelectric polarisation. As a result, the effective grain boundary potential barriers are changed, leading to a modification of the IV-characteristics of the material. Studies in recent times have investigated the workings of this effect in the context of photonic strain mapping [12], strain-gated transistors [13] and novel nanowire strain sensors [14]. In particular, Baraki, Rödel et al. studied the stress sensitivity of electrical conductivity in ZnO varistor ceramics in [15, 16]. Here, gauge factors extending into the high hundreds were found. Such values identify ZnO as appropriate for use in macroscopic pressure sensors. The samples investigated were of conventionally manufactured ZnO varistor material subjected to uniaxial compressive stresses of the order of 100 MPa. To the author's knowledge, so far no pressure sensing devices based on the piezotronic effect in ZnO varistors have been manufactured. However, the large gauge factors observed experimentally clearly qualify the material for such applications [16]. A simple scheme for a pressure sensor based on a varistor structure with a properly tailored combination of grain orientations was recently proposed by Zhou at al. [17].

Verghese et al. [18] originally proposed the mechanism behind the mechanical modification of ZnO grain boundary potential barriers in their study of the effect of internal stress on the electrical conductivity of ZnO varistors. This remains the most current model to this day [19]. However, the piezoelectric contribution to grain boundary conductivity could not be experimentally verified until very recently. Raidl et al. [20] were able to demonstrate that the mechanical modulation of electrical conductivity for ZnO bicrystals depends on the reciprocal grain polarity, as previously postulated in Verghese's paper. In the interest of maximising stress sensitivity, efforts have also been made by Keil, Rödel et al. [21] to manufacture a single bicrystalline interface of optimal relative orientation.

The basic mechanism of the piezotronic effect for a single grain boundary is reasonably well understood. However, the electromechanical characterisation of bulk ceramic material remains a challenge to this day. In varistor samples of macroscopic size large numbers of grains of many different sizes, shapes and crystallographic orientations are present. As a result of this, each grain boundary within such a sample experiences a different mechanical stress. Subsequently, the conductivity of some grain boundaries rises and that of others falls, depending on the mechanical stress field within the material and the distribution of crystallographic orientations. In addition to this, the intrinsic properties of individual grain boundaries, such as dopant concentration and the presence of native defects, are generally different. Thus, the electrical conductivity of each boundary is different. Even for an ideal system containing only electrically identical grain boundaries, each would operate at a different working point along the IV-characteristic and thus manifest a different conductivity. All of these factors cause the electric

current distribution in the material to be highly inhomogeneous. Particularly in the breakdown varistor regime, the electrical current flowing through such materials is concentrated along a few highly conductive pathways with extremely high current density [22]. Thus, the effective electrical conductivity of the bulk varistor is determined by a complicated interplay between single boundary effects and the macroscopic properties of the polycrystalline structure.

This thesis introduces a modelling approach for the electromechanical characterisation of ZnO varistors on the mesoscopic scale. The model begins by expanding upon the work of Bavelis et al. [23], which is itself an improvement upon the model of Vojta et al. [24]. In this model, the varistor microstructure is represented by a large, non-linear electrical network. By solving a global set of circuit equations, this approach makes the computation of the current flow patterns in the material possible. Furthermore, the piezotronic effect is accounted for via computation of the mechanical stress field throughout the material for varying applied stresses. This is achieved using the finite element method. Using a self-consistent grain boundary model to describe the mechanical modulation of potential barriers due to piezoelectric polarisation, the influence of the local stress state at each individual grain boundary can then be accounted for.

2 Zinc Oxide Varistors and Applications

2.1 Overview

Varistor ceramics first came into use early in the 1930s, when they were developed as a replacement for selenium rectifiers. These first materials were composed of sintered blocks of compressed SiC powder, and it was not until 1969 that improvements in ceramic processing techniques led to the creation of the first ZnO varistors in Japan. These varistors were produced using many of the same processes that are considered vital to this day, including the addition of substitutional ions to enable the ZnO to act as a semiconductor, the densification of the ceramic powder by liquid-phase sintering with a Bi_2O_3-rich liquid phase, and the segregation of large ions to the grain boundaries [25]. The varistor material was further doped with cobalt and manganese to increase the non-linearity of its IV-characteristic curve. As research continued, aluminium was also found to be beneficial in this respect. These developments established ZnO as clearly superior to the older SiC varistors, which were gradually made obsolete and replaced for most applications worldwide.

Since that time, techniques for the production of high performance varistor ceramics have been steadily refined. Modern components feature greater resistance to degradation, improved microstructural uniformity, and increased reliability. This has been, in part, made possible by a finer level of control over the manufacturing process. Furthermore, increased understanding of the reactions between the various ingredients has allowed for chemical approaches to powder homogenisation and computational methods for the calculation of superior ceramic compositions [26]. Today, ZnO varistors are capable of protecting a broad variety of systems, ranging from low voltage semiconductor circuits, for which an 'over-voltage' is of the order of volts, to high voltage electrical power distribution networks, which must withstand over-voltages of the order of tens of kilovolts.

The primary function of a varistor is to curb transient voltage surges. For many technological applications, this process must be non-destructive and repeatable. Varistors are used across broad ranges of both current (μA to kA) and voltage (V to kV), and in both AC and DC applications. Furthermore, a critical feature of an industrial varistor is its capability to rapidly absorb large quantities of energy, up into the kilojoule range. These properties have led to widespread adoption of ZnO varistors as surge arresters in the power transmission industry.

A surge arrester compensates for over-voltages that occur during power surges by absorbing electrical energy, directing it to earth and converting it into heat. These surges commonly occur due to switching errors or lightning strikes, and using surge arresters to limit damage to the power network can significantly reduce maintenance costs. Mains-born transient surges can also occur in industrial equipment, as well as domestic lighting and appliances. In such applications, varistors are commonly connected directly across mains supplies, or across semiconductor switches for the protection of transistors, MOSFETs and thyristor bridges.

Large scale surge arresters in power stations are typically composed of a column of cylindrical varistor blocks in series, which are protected by an external housing composed of plastic-coated porcelain. This housing is designed to shield the ceramic varistor components from environmental influences such as humidity and other contaminants. A gap is maintained between the varistor column and the housing, inside of which a hermetically sealed atmosphere is maintained as additional isolation. This atmosphere is usually composed of nitrogen, although sulphur hexafluoride or even solid isolators also sometimes see use. If the surge arrester is overloaded, this atmosphere can become highly pressurised and safety measures must be implemented to allow the gas to be released so that the arrester housing does not burst.

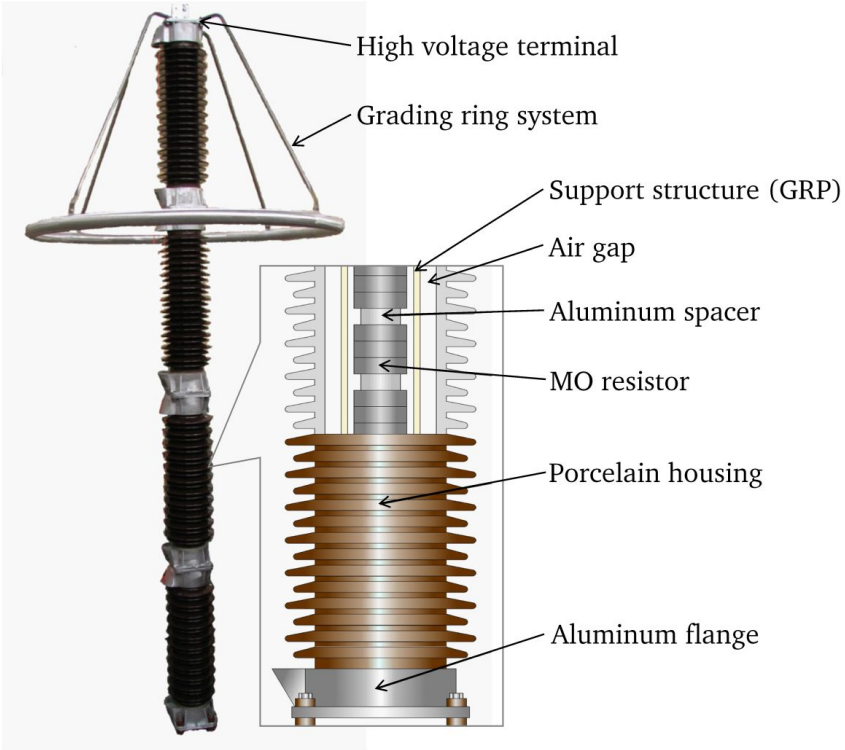

Figure 2.1.1.: Schematic of a four-segment station-class surge arrester with porcelain housing (reproduced from [27] with permission).

ZnO's semiconducting and piezoelectric properties also make it suited for applications in microelectronics. One example of this is strain-gated transistors, which can be produced using ZnO nanowires [13]. These are made possible by the piezotronic effect, which enables the Schottky contact with the nanowire to be manipulated using an applied force. This mechanical force is the transistor's gate signal, and is applied to one end of the metal-nanowire-metal structure. Aligned arrays of such nanowires can be manufactured such that each nanowire has its own gate voltage, and thus function as a transistor array.

In order to understand the electrical behaviour of varistors, some fundamentals must first be considered. In Figure 2.1.2, the DC IV-characteristic of a ZnO varistor is shown. The distinguishing feature of this characteristic is the sharp transition from the insulating to the conducting state at the breakdown voltage V_c. The switching effect observed here is mainly reversible and the transition occurs extremely rapidly (typically of the order of pico- to nano-seconds). In practice, this means that, immediately upon the applied voltage V dropping beneath V_c, current flow through the resistor is drastically reduced. The value of V_c can be engineered to take a specific value by manipulating parameters such as the varistor dimensions and geometry. The range of possible values is very broad. Typical values for V_c for a single grain boundary range from approximately 3.2 V to 3.4 V [25]. In a macroscopic scale varistor, large numbers of grain boundaries combine in series and in parallel to give the electrical characteristics of the varistor as a whole. The magnitude of V_c scales based on this configuration, and values of up to $>10^4$ V are possible. This allows for surge protection applications ranging from electronic circuits all the way to ultra high voltage systems.

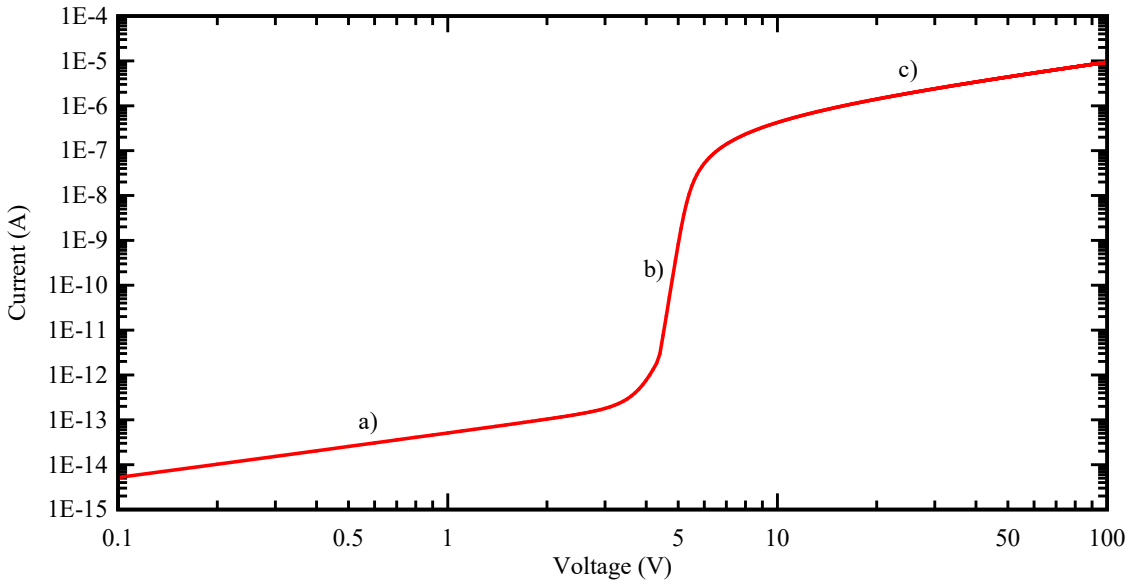

Figure 2.1.2.: Example IV-characteristic curve of a ZnO varistor, illustrating the leakage (a), breakdown (b) and upturn (c) regions.

Three distinct regions of the characteristic curve shown in Figure 2.1.2 can be discerned: leakage (a), breakdown (b) and upturn (c). Varistors for surge arrester applications typically operate under applied voltages that fall within the upper end of the leakage region, which is characterised by a very large Ohmic resistance. This resistance is determined almost entirely by the resistance of the grain boundaries within the material. The breakdown region is the region in which the highly non-linear behaviour of the varistor appears. Above V_c, the resistance of the varistors rapidly falls by several orders of magnitude. This occurs across a relatively small voltage range and results in a typical increase in the current density through the material of six or seven decades.

This non-linearity can be quantified using the non-linearity coefficient α. Assuming an exponential law for the varistor current in the breakdown region,

$$I \sim V^{\alpha}, \tag{2.1.1}$$

the non-linearity coefficient is given by,

$$\alpha = \frac{d\log_{10}(I)}{d\log_{10}(V)}. \tag{2.1.2}$$

The greater the value of α, the stronger the increase in current vs. voltage becomes. Thus, a varistor with high non-linearity coefficient can switch more quickly between the leakage (insulating) and upturn (conducting) regions. Usually, α has maximum values of the order of 30-80 [25]. In rare cases, values of 100 or higher have also been achieved. At the extreme ends of the curve, in the upturn region, the varistor displays Ohmic behaviour and α is close to one. However, the breakdown region can separate the two Ohmic regions by as many as 12 current decades [28, 29]. When a surge does occur, this can be considered as a transient over-voltage that triggers the varistor effect when it pushes the applied voltage across the breakdown and into the upturn region. Here, the resistance is determined almost entirely by the bulk material and the varistor once more displays Ohmic behaviour.

These different regions of the IV-curve are all capitalised upon in practical applications. The operating point under the application of a steady external voltage is determined by the power loss in the low-current leakage region. The clamping or critical voltage, at which the resistance grows rapidly, is determined by the location of the non-linear breakdown region. Finally, high current surges, such as those that occur when lightning strikes a power station, require a high capability for energy absorption. This is achieved by connecting varistors in parallel with the system they are designed to protect. Under normal operating conditions, the varistor's resistance is high, and almost all of the current flows through the protected device. However, when an over-voltage occurs, the varistor's resistance falls rapidly and the additional current is directed through the varistor and away from the sensitive circuits of the protected device.

2.2 Material Structure of Zinc Oxide Varistors

ZnO occurs in wurtzite, sphalerite and face-centered cubic crystals. However, under standard conditions for temperature and pressure, wurtzite is the thermodynamically stable phase. Crystallographically, this point group is known as $P6_3mc$ No. 186, and the associated coordination number for both zinc and oxygen atoms in this form is 4. The lattice constants of the wurtzite unit cell for ZnO are $a = 0.3249$ nm and $c = 0.5207$ nm, with a proportionality factor of 1.602, slightly lower than that of a perfect hexagonal close packed structure (1.633). In the crystal's c-direction, this results in a unit cell consisting of four alternating layers of zinc and oxygen. The crystal is zinc terminated in the (0001) direction and oxygen terminated in the $(000\overline{1})$ direction.

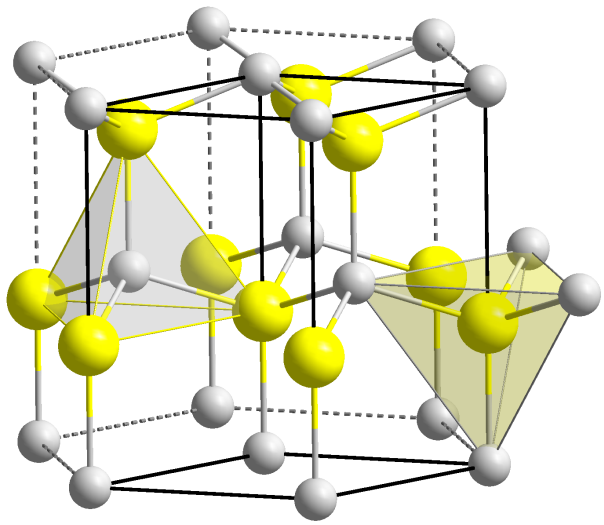

Figure 2.2.1.: Crystal structure of ZnO (wurtzite) with coordination polyhedra. The c-axis runs top to bottom and describes the 'height' of the unit cell. The a-axis consists of one side of the hexagonal base. [30]

In its pure form, ZnO contains intrinsic and extrinsic defects that make it an n-type semiconductor. These naturally occurring defects are typically point defects such as oxygen vacancies, zinc interstitials, or the substitution of an oxygen atom for zinc. Furthermore, impurities arising from hydrogen interstitials and zinc-nitrogen complexes have also been shown to result in an overall increased conductivity in ZnO [31,32]. The band gap of ZnO lies between 3.1 and 3.3 eV [33].

It is this crystalline structure and the ionic nature of the ZnO bonds that results in the directional polarity across the crystal. Within the bulk, the opposing charges are evenly

distributed, resulting in overall neutrality. However, both the zinc and oxygen terminated ends of the crystal carry a polarisation charge. Theoretically, the maximum polarisation at such a surface is -0.057 C/m^{-2}, with a charge carrier density of 3.6×10^{13} cm^{-2}.

The piezoelectric effect in ZnO is possible, because of the lack of inversion symmetry in the above structure (with exception of the point group (432)). In crystallography, thirty-two unique crystallographic point groups exist, forming the complete set of possible crystallographic unit cells. Of these, twenty are know to exhibit piezoelectricity, all of which are non-centrosymmetric. This can be observed in the electromechanical behaviour of thin films and heterostructures composed of non-centrosymmetric semiconductors, which are susceptible to the piezoelectric effect [34–36]. However, the piezoelectric modification of charge transport in polycrystalline semiconductors has not been studied extensively.

In order to produce the non-linear IV-behaviour necessary for a varistor, ceramic resistors composed of a mixture of metal-oxides are manufactured. These ceramics use ZnO as a base for the bulk of the material, specifically, 90% of the material's total mass. ZnO is chosen as the primary material in this context due to its wide band-gap and semiconducting behaviour. A few percent of selected elements, such as Bi, Sb, Co, and Mn, are typically added as dopants and combined by way of an appropriate sintering process in order to engineer the desired varistor characteristics. These elements make up the remaining 10% of the varistor, by mass. A list of common additives and their effects is shown in Table 2.2.1.

Table 2.2.1.: Common Dopants and their Uses [37–42]

Dopant	Effect
Al_2O_3	Increased non-linearity of the IV-characteristics.
Ag, B_2O_3 and Ni	Increased stability.
BeO and TiO_2	Increased grain growth.
Bi_2O_3	Lines grain boundaries. Significantly increased potential barrier. Increased grain growth. Homogeneous dopant distribution.
CoO and MnO	Greatly increased non-linearity of the IV-characteristics.
Cr_2O_3	Increased non-linearity and stability. Limited grain growth.
Ga	Increased non-linearity by donation of charge carriers.
Nb_2O_5	Increased non-linearity and electrical energy absorption.
Pr_6O_{11}, SrO and U_3O_8	Marginally increased potential barrier at the grain boundary.
Sb_2O_5 and SiO_2	Limited grain growth. Increased microstructural homogeneity.

At the triple points, at which the adjacent grain edges make contact, the majority of the admixed Bi_2O_3 collects as a separate phase. A spinel phase of very fine, regular, octahedral grains is also found at these triple points. Nevertheless, the grain boundaries also contain trace quantities of Bi in a monolayer lining the interface, and this is essential for the electrical function of a varistor [25, 38, 43–50].

When Bi_2O_3 melts to form a liquid phase during sintering, it dissolves a part of the other dopants and distributes them uniformly across the interface. Furthermore, this liquid phase promotes dense sintering and grain growth. This effect is counteracted by the spinel precipitates, which themselves inhibit grain growth. It is the balancing nature of these effects that helps to achieve a uniform distribution of ZnO grain sizes in the polycrystal. Another crucial factor for the grain growth mechanism are inversion or twin grain boundaries, as described by Bernik et al. [51].

Atomic defects that form at the grain boundaries are incorporated into the ceramic. The grain boundary states are dominated by acceptor defects and the depletion layer is dominated by donors. A defect model that accounts for the role of oxygen in the development of non-linear behaviour in ZnO was developed by Selim et al. [52]. In this model, V'_{Zn}, V''_{Zn}, $V^{\bullet}_{O}$, $V^{\bullet\bullet}_{O}$, $Zn^{\bullet}_{i}$, $Zn^{\bullet\bullet}_{i}$, $D^{\bullet}_{Zn}$ and D'_{i} are the relevant defect species as described using the Kröger-Vink notation. Here, $D^{\bullet}_{Zn}$ and D'_{i} are terms respectively covering all externally incorporated donor and acceptor atoms.

According to Matsuoka [53], a physically separate intergranular layer is not necessary to account for the potential barrier. In fact, it is the unequal migration of defects towards the grain boundary that results in a defect-induced potential barrier. During cooling from high fabrication temperatures, the concentrations of zinc vacancies and oxygen vacancies at the grain boundary grow and fall, respectively. This charge separation can only occur in the presence of a substantial donor doping, which, quantitatively, necessitates a deep donor concentration of approximately 10^{18} cm^{-3}. The resulting excess and deficit of zinc and oxygen vacancies, respectively, produces the potential barrier, thus removing the need for a separate interface layer at the grain boundary. There is also a notable depletion of mobile electrons near the grain boundary in comparison to the grain bulk. This is the source of ZnO's high electrical resistance at low applied voltages.

The basic steps of the manufacturing process for metal-oxide resistors are [28, 29, 54]:

- The production of a homogeneous slurry by the wet-mixing of oxide powders.
- The drying and granulation of the slurry in a spray-drier.
- The compacting of the granulate to form resistor blocks.
- The sintering of the resistor blocks to obtain dense ceramic bodies.

Before sintering, the organic additives mentioned above must be pyrolised. This step requires a continuous flow of fresh air, along with varying heat treatments. The sintering process is

performed at a temperature between 1400 K and 1600 K, and densifies the compacted powder into a solid ceramic body. This occurs by diffusion, as the microscopic powder particles merge and grow into larger single crystals or grains. This leads to the formation of grain boundaries between the single crystals, along which the dopants crystallise into lattices. Almost no porosity remains in the fully sintered ceramic body.

2.2.1 Grain Boundaries

ZnO's special electrical properties occur due to its microstructure. The microstructure is a configuration of densely-packed, microscopic ZnO crystals or 'grains' that resemble irregular polyhedrons, each of the order of 10 μm in size. The bulk material of each individual grain is a good electrical conductor with a conductivity of the order of 1 Scm^{-1}. However, it is the common interfaces, or grain boundaries, between these grains that are the electrically active part of the material.

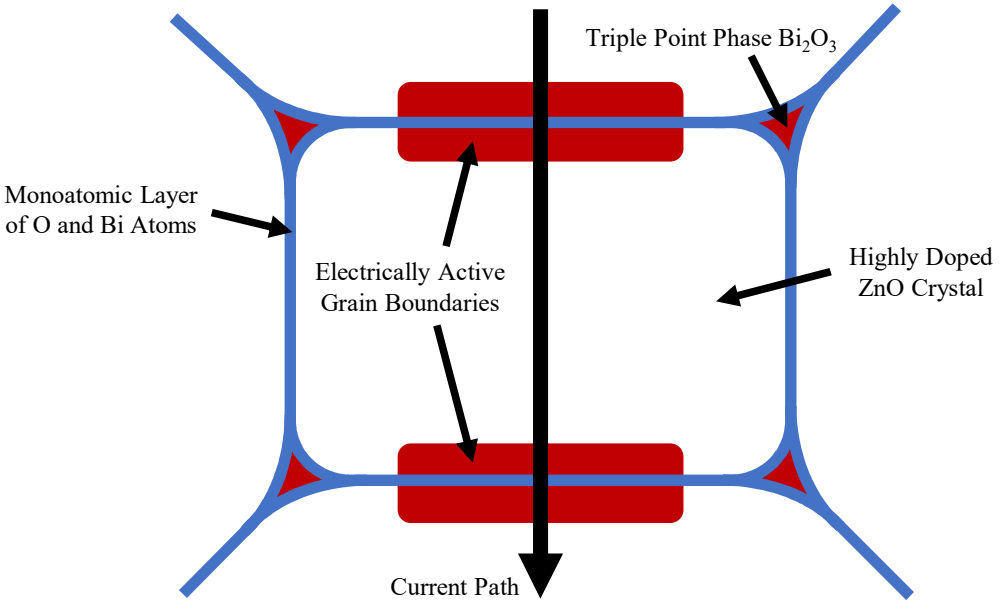

Figure 2.2.2.: Schematic view of the 'electrical' microstructure of a ZnO-varistor. Redrawn according to [8].

Highly insulating electrostatic potential barriers are present at the grain boundaries. These electrostatically repulsive barriers extend less than 100 nm from the interface, which is approximately 1 nm thick itself. Given the relatively high conductivity of the bulk material, current flow through a polycrystal at low voltages is limited by the high resistance of the grain boundaries, and must seek the path of least resistance. In the breakdown region, the conductivity of the individual grain boundaries rises enormously, until, in the upturn region, current flow is limited by the resistance of the grain bulk material.

In principle, the grain boundaries and the grain bulk are composed of the same semiconducting ceramic material. However, the grain boundaries are rich in defects and dopant species. These defects can be dangling bonds at the interface, or other interface defects that occur between neighbouring grains as a result of the mismatch in the crystal lattice. Furthermore, the various doping species gather near the grain boundary and contribute electrical donor and acceptor states. This results in additional interfacial electrical states within the band gap at the grain boundaries. Extra electrons are trapped at the grain boundaries in these defect states, resulting in electrostatic potential barriers. The macroscopic switching effect observed in ZnO varistors occurs due to these interfacial states at the individual grain boundaries. It is important to note that until the upturn region, when the bulk conductivity of the ZnO grains ($\approx 0.1 - 1\ \Omega$m) [54, 55] begins to contribute, the voltage drop only takes place on the positively biased side of the interface.

Nanoscale intergranular films of an amorphous Bi_2O_3-ZnO solid solution are consistently observed along all microstructural interfaces in ZnO [25, 38, 43–50]. This is considered to be a feature of the thermodynamic equilibrium. Based on the concentration of Bi present, these films must be approximately one atomic layer in thickness. The electrical activity of these interfaces is the result of an additional monolayer of excess oxygen atoms [38, 47]. This leads to a build-up of negative charge trapped at the grain boundaries. In order to maintain charge neutrality, positive, ionised donors in the depletion region must compensate for this charge, thus forming an electrostatic potential barrier, ϕ_B, at the grain boundary. The total width of these barriers is around 200 nm, two orders of magnitude less than the typical grain size of 10-20 μm.

The fact that non-linear varistor behaviour in ZnO is a grain boundary phenomenon has led to the development of a variety of models [25, 54, 56, 57]. As atomic level understanding of the nature of grain boundaries and their influence on the microstructure as a whole has improved, these models have been refined to better reflect the physics of grain boundaries [38, 43–50, 54, 57].

The hole-induced breakdown model was first proposed by Pike, Greuter and Blatter [57–62] and provides a semi-quantitative explanation for the unusual breakdown phenomena in ZnO varistors. It is in fact possible to directly observe the band-band recombination described by the model, due to the fraction of the holes that recombine with electrons in the conduction band. This process emits a measurable quantity of ultraviolet light, thereby providing direct evidence for the validity of the model [63–65]. The breakdown region can also be observed in the visibile spectrum due to defect levels in the band gap, which are ionised by the hot electrons. Cobalt is the dopant primarily responsible for this effect [63–68]. These emissions are, in fact, strong enough to be observed under an optical microscrope and function almost exactly like

miniature light-emitting diodes. As a result of this, it is possible to observe the filamentary nature of current flow through a varistor using electroluminescence and high speed infrared imaging techniques [57, 66, 69, 70].

One major motivation behind the development and refinement of such models is to minimise power loss due to the leakage current depicted in Figure 2.1.2. Leakage occurs due to thermally activated conduction electrons that jump across the potential barrier ϕ_B, and can be prevented by ensuring the barrier remains high with increasing voltage V. In order to achieve this, the interface states, $N_i(E)$, must have a suitable energy distribution and a high density across the band gap. If all interface states ever become filled, then the total interface charge, Q_i, becomes constant and ϕ_B decays, resulting in a poor varistor.

This effect can be avoided by ensuring the presence of both filled and unfilled interface states. This technique is known as 'pinning' the potential barrier and works by trapping additional electrons in the unfilled states. This contributes to the growth of Q_i, and counteracts the decay of the potential barrier, thus reducing the leakage current. Pinning techniques are widespread in semiconductor science and pinning states are commonly comprised of characteristic defect levels for the given material [57]. This is true of the ZnO crystal lattice and intergranular films, in which these defect levels can always be found at the same energies in the ZnO band gap [57, 71, 72]. ZnO is a prime material for such purposes, since its chemical make-up is never entirely stochiometric. At equilibrium, this generally means an excess of Zn atoms. However, the concentration of these pinning states can be adjusted by engineering a specific defect equilibrium, by choosing the correct dopants and via heat treatment during manufacturing.

Such adjustments naturally also come with differences in the potential barrier, and thus the IV-characteristics of the varistor materials. A true quantification of the defect equilibrium in ZnO, and how it changes with the addition of the dopants that lead to varistor behaviour, remains a challenge to this day [73–77]. However, in a qualitative sense, this model does explain why certain dopant 'recipes' produce usable varistors, and why their properties vary even with small changes to this complex chemical makeup [43, 44, 57, 71].

Strong pinning results in the build up of high electric fields on the positively biased side of the grain boundary. For industrially doped varistors, these fields are of the order of 1 MVcm^{-1}, which is sufficient to generate hot electrons with a high charge carrier mobility comparable to other high performance semiconductors, such as GaAs. Once the energy of the electrons near the edge of the space charge region is above that of the ZnO's band gap, holes are created in the valence band due to impact ionisation. This results in a compensation of the negative interface charge Q_i, as the positively charged holes diffuse back into the grain boundary. This entire process takes less than a nanosecond and results in a reduction in the potential barrier, thus

increasing the conductivity of the grain boundary and in turn promoting the generation of even more hot electrons. This feedback effect leads to a rapid decay of the potential barrier and is directly responsible for the high levels of non-linearity seen in ZnO varistors. In order to achieve such a pronounced varistor effect, not only is strong pinning of the potential barrier necessary, but the barrier must also suddenly decay upon reaching the critical voltage, as described above.

2.3 Electrical, Thermal and Mechanical Phenomena in Varistors

When a varistor is pushed into the breakdown region by an over-voltage, current-flow through the component is increased by several orders of magnitude. A significant proportion of this electrical energy is absorbed by the material and converted into thermal energy. Surge arrester columns of the kind introduced in section 2.1 have been developed explicitly for such purposes. However, this heating can also result in irreversible changes to the structure and thus the electrical properties of the varistor, which are detrimental to its function. Repeated power surges can cause a varistor to be so heavily damaged that its capability to absorb electrical energy falls so low that it can no longer fulfil its purpose and the component must be replaced. This is an expensive prospect, which can mean replacing the entire varistor column.

An extreme example of this kind of destructive mechanism is known as 'thermal runaway' [8]. In such a scenario, the increased temperature from the electrical energy absorbed during a power surge results in an increased leakage current through the varistor at its normal operating voltage. This is because the electrical conductivity of ZnO increases with temperature. If this increased leakage current generates more thermal energy in the varistor than the component can dissipate in a given time-frame, then the varistor temperature, and thus the current flow, will continually grow until the ceramic burns through. Furthermore, in practice, power surges are generally very short and intense, resulting in a sudden increase of temperature in the varistor along an isolated current-flow path. This occurs as a result of inhomogeneity in the ceramic's microstructure, and results in levels of thermomechanical stress that can lead to fracture.

Especially high temperatures resulting from protracted, high-intensity surges can even result in the melting of the material along the current-flow path, resulting in an electrical 'puncture' effect. As a result of this, it is vital that surge arresters be designed to optimise the rate of heat dissipation from the individual varistor blocks. Examples of how to achieve this include the use of varistor blocks of sufficiently large dimensions that the thermal energy can be well distributed, and also the addition of heat sinks, such as metal spacers, between varistor components.

Figure 2.3.1 (left) illustrates an example of failure inside a varistor component as a result of thermal runaway [78]. Figure 2.3.1 (right) shows an example of the kind of damage that can occur when the temperature along the current-flow path grows so high that melting occurs

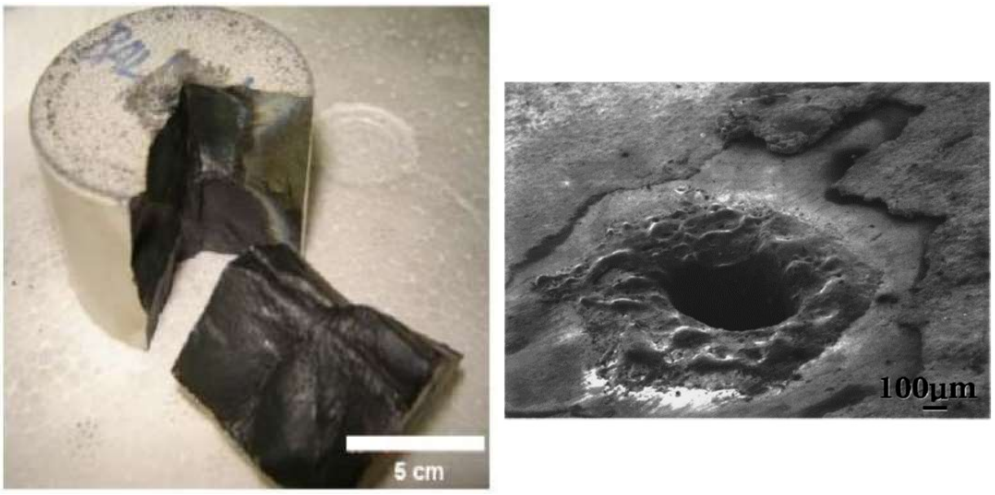

Figure 2.3.1.: Examples of damage found in ZnO varistors following thermomechanical failure. Left: ZnO varistor after catastrophic electrothermal runaway [78]. Right: Scanning electron micrograph of a ZnO varistor sample failed in puncture mode [7].

along it (puncture) [7]. If such a path makes contact with the outer edge of the varistor block, it can result in a surface fracture due to the build-up of pressure inside the ceramic. If the electric field is high enough, flashover may occur across such a region, or at the surface [8].

If the varistor block is perfectly homogeneous, then it can only fail if the mechanical stresses induced by the high current exceed the fracture strength of the material, or by thermal runaway. However, in practice, inhomogeneity is impossible to eliminate entirely. Whether they are present macroscopically, or on a microstructural level, such inhomogeneities inevitably lead to local hot spots within the material, which result in either fracturing due to mechanical stress concentration, puncturing, or melting. Such inhomogeneities commonly take the form of cavities within the microstructure or a broad distribution of grain sizes. Chemical inhomogeneity can also affect the electrical properties of individual grain boundaries, leading to further current concentration [8].

3 Grain Boundary Theory

3.1 Grain Boundary Potential

The grain boundary potential in ZnO varistors arises from the combination of the energy band structures of the two grains and the dopant species that sit along the interface between them. At room temperature, wurtzite ZnO exhibits the following energy band structure [79],

- The lowest valence band energy level is composed of the O 2s orbital.
- The higher valence band energy levels are a blend of the O 2p, Zn 4s and Zn 4p orbitals.
- The lowest conduction band energy level is composed of Zn 4s orbital.
- The highest conduction band energy level is composed of the Zn 4p orbital.

Furthermore, additional energy levels are introduced into the forbidden band by local defects and the aforementioned dopant species [11].

When two grains meet, these energy bands come into contact, forming the band structure of the individual grain boundary. In order to achieve thermodynamic equilibrium, electrons flow across the interface until the Fermi level is the same on both sides. Since the Fermi level of the grains is higher than that of the grain boundary material, electrons flow from the grains to the grain boundary. Here, they are trapped by dopant species and crystallographic defects, thus increasing the Fermi level until is even across the interface. This results in a negative sheet charge of trapped electrons at the grain boundary and leaves a layer of positively charged donor sites on each side of the boundary. This is known as the depletion layer. These positive charges cause an upward bending of the energy bands close to the grain boundary, which presents as an electrostatic field with a barrier at the grain boundary known as a 'double Schottky barrier' [80]. This is illustrated in Figure 3.1.1.

Since the interfacial region is typically approximately 1 nm wide, for modelling purposes, it is justified to idealise the interface as infinitely thin. Furthermore, the plane interface is translationally invariant, which makes it possible to reduce the problem to 1D [58]. The following model for the charge carrier transport in varistor grain boundaries has been proposed by Blatter et al. [57, 58]. In this model, the band bending profile at the boundary, induced by an applied potential, is calculated in the Schottky approximation. Blatter begins by calculating the

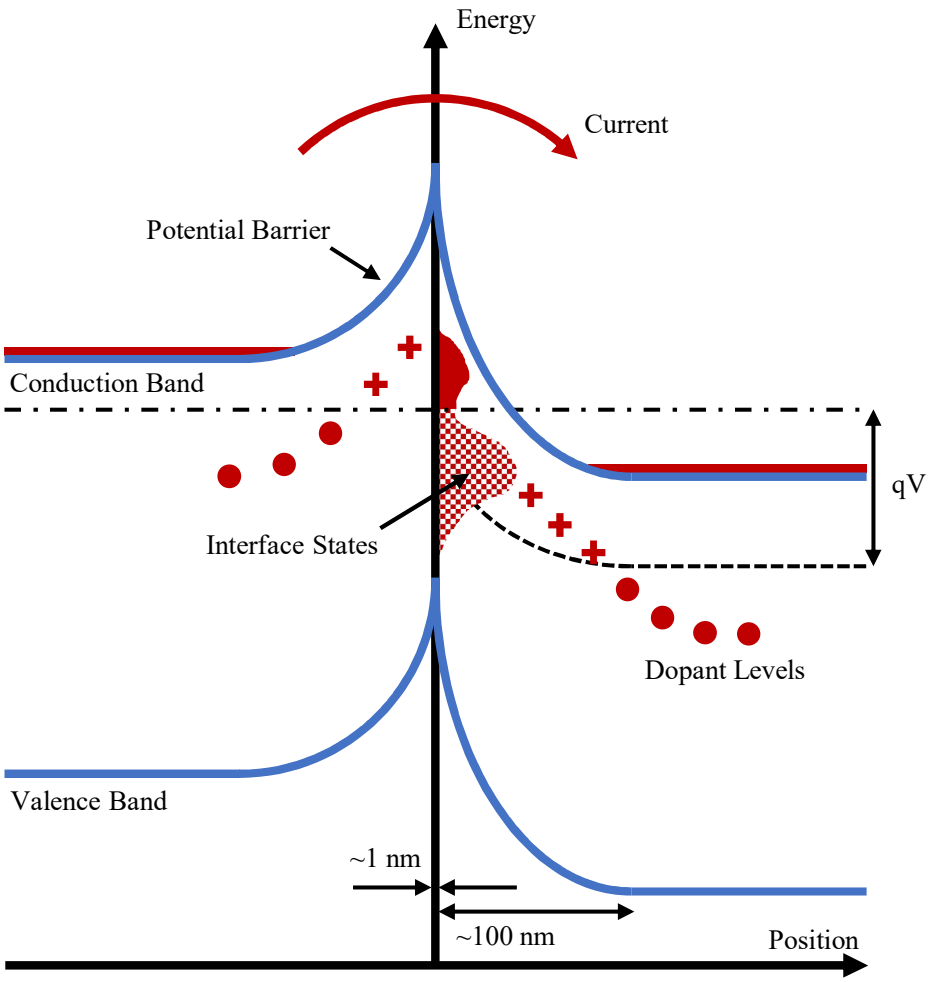

Figure 3.1.1.: Band diagram of a single grain boundary, showing the double Schottky Barriers formed by charge trapping in interface states. Redrawn according to [8].

geometry of the energy bands around a plane charged interface. In order to do this, the Poisson equation

$$\frac{d^2\phi(x)}{dx^2} = \frac{\rho(x)}{\varepsilon_0 \varepsilon_r}, \tag{3.1.1}$$

for the potential, $\phi(x)$, must be solved for the charge distribution

$$\rho(x) = q\sum_{\nu=0}^{n} N_\nu[\Theta(x + x_{l\nu}) - \Theta(x - x_{r\nu})] - Q_i\delta(x), \tag{3.1.2}$$

where ε_0 is the permittivity of vacuum, ε_r is the relative permittivity of the material, q is the positive unit charge, N_ν is the density of the deep trap states, $\Theta(x)$ is the Heaviside step function, $x_{l\nu}$ and $x_{r\nu}$ are the widths of the left and right depletion layers, respectively, Q_i is the net interface charge and $\delta(x)$ is the Dirac delta function [58]. Note that in (3.1.1), the convention $q = |q|$ is adopted, such that the potential energy of an electron is $q\phi(x)$.

When the boundary conditions

$$\phi(-\infty) = \phi(-x_{l0}) = 0\,, \tag{3.1.3}$$

and

$$\phi(\infty) = \phi(x_{r0}) = -V\,, \tag{3.1.4}$$

are imposed on the Poisson equation, where V is the voltage applied across the grain boundary, then the following double Schottky barrier configuration is obtained

$$\phi(x) = \begin{cases} \sum_{\nu=0}^{\mu} \frac{\gamma_\nu}{2}(x + x_{l\nu})^2, & -x_{l,\mu} \le x \le -x_{l,\mu+1} \\ \sum_{\nu=0}^{\mu} \frac{\gamma_\nu}{2}(x + x_{r\nu})^2 - V, & x_{r,\mu+1} \le x \le x_{r,\mu} \end{cases}, \tag{3.1.5}$$

where $\gamma_\nu = \frac{qN_\nu}{\varepsilon_0\varepsilon_r}$ and, for $\mu = \nu$, the following is defined,

$$x_{l,n+1} = x_{r,n+1} = 0\,. \tag{3.1.6}$$

The Blatter-Greuter model [58] determines the widths $x_{l\nu}$ and $x_{r\nu}$ from (3.1.5) using the following conditions

$$\phi(0^-) = \phi(0^+) = \phi_B\,, \tag{3.1.7}$$

$$\phi'(0^-) - \phi'(0^+) = \frac{Q_i}{\varepsilon_0\varepsilon_r}\,, \tag{3.1.8}$$

where ϕ_B is the barrier height. This is shown in the derivation given in the appendix of [58] and results in

$$x_{l0} = \frac{Q_i}{2\gamma_\nu\varepsilon_0\varepsilon_r}\left(1 - \frac{V}{V_c}\right), \tag{3.1.9}$$

$$x_{r0} = \frac{Q_i}{2\gamma_\nu\varepsilon_0\varepsilon_r}\left(1 + \frac{V}{V_c}\right), \tag{3.1.10}$$

as given explicitly in [11]. Thus, the general expression for ϕ_B can be derived (see the appendix of [58]) as

$$\phi_B(V) = \frac{1}{4}V_c\left(1 - \frac{V}{V_c}\right)^2 + \frac{1}{q\gamma}\sum_{\nu=1}^{n}\gamma_\nu(\epsilon_\nu - \epsilon_\xi), \quad V \le V_c\,, \tag{3.1.11}$$

where q is the positive unit charge, V is the applied voltage, V_c is a switching voltage and ϵ_ν and ϵ_ξ are, respectively, the deep trap energies and the bulk Fermi level relative to the conduction band. γ is the total charge in the deep trap states, defined as $\gamma = \sum_{\nu=0}^{n}\gamma_\nu$.

The self-consistent solution of the electrostatic problem and carrier density across the boundary yields a potential barrier with height given in (3.1.11). Furthermore, the switching voltage, V_c, is related to the interface charge trapped in the interface states at the grain boundary, Q_i, by

$$V_c = \frac{1}{2\gamma}\left(\frac{Q_i}{\varepsilon_r \varepsilon_0}\right)^2 . \tag{3.2.1}$$

Q_i is voltage-dependent, and so, when a voltage is applied, the barrier height is lowered accordingly, until, at V_c, it vanishes completely.

The interface charge in (3.2.1) is determined by the density of interfacial states, $N_i(E)$, assuming that the electron traps are filled up to the Fermi level, ξ_i^n, of the neutral interface,

$$Q_i = q\int_{\xi_i^n}^{\infty} N_i(E) f_i(E) dE\,, \tag{3.2.2}$$

where $f_i(E)$ is the Fermi-Dirac function,

$$f_i(E) = \frac{1}{1+e^{(E-\xi_i)/k_B T}}\,, \tag{3.2.3}$$

ξ_i is the quasi Fermi level of the interface, k_B is the Boltzmann constant and T is the temperature. When no voltage is applied, the Fermi level is constant throughout the grain boundary and $\xi = \xi_i$. However, when $V > 0$, the quasi-Fermi level is shifted relative to the bulk Fermi level, as depicted in Figure 3.1.1. This shift takes the form

$$\Delta\xi = \xi - \xi_i = k_B T \ln\left(\frac{2}{1+e^{\frac{-qV}{k_B T}}}\right), \tag{3.2.4}$$

and is determined by the interface's charge balance condition. That is, the number of electrons trapped and emitted by the interface must be equal [58].

In order to determine the interface charge (3.2.2), the modification of the interface density of states, $N_i(E)$, due to the presence of a grain boundary potential, ϕ_B, must be taken into account. In other words, Q_i and ϕ_B are mutually dependent. When a bias voltage V is applied to the junction, the interface states are shifted according to $N_i(E) = N_{i0}(E - \phi_B(V))$, where $N_{i0}(E)$ is the density of interface states in the absence of a grain boundary potential. Thus, in order to determine Q_i and ϕ_B, a self-consistent solution of the coupled equations (3.1.11)-(3.2.2)

is required. Generally, such a solution can only be obtained numerically, as described later in Section 4.1 and given in Appendix A.1.

Finally, given a solution for $\phi_B(V)$, the total current across the boundary is [58]

$$I = a_B A^* T^2 \exp\left(\frac{-q\phi_B + \epsilon_\xi}{k_B T}\right)\left[1 - \exp\left(\frac{-qV}{k_B T}\right)\right], \tag{3.2.5}$$

where A^* is the Richardson constant and a_B is the grain boundary area. This expression defines the non-linear electrical characteristic of the grain boundary.

3.3 The Piezotronic Effect

The piezotronic effect describes the principle of using a mechanically induced potential in a piezoelectric material as a gate voltage in order to tune and/or control the material's charge carrier transport properties. This mechanism takes advantage of the piezoelectric effect, which occurs in two forms.

When a mechanical stress, $\boldsymbol{\sigma}_{jk}$, on a material results in the accumulation of electric charge, and thus a polarisation, $\boldsymbol{P}_i$, within the material, this is direct piezoelectricity. This effect is described by

$$\boldsymbol{P}_i = \boldsymbol{d}_{ijk} \cdot \boldsymbol{\sigma}_{jk}\,, \tag{3.3.1}$$

where $\boldsymbol{d}_{ijk}$ is the tensor of piezoelectric stress constants for the material. In Voigt notation, $\boldsymbol{d}$ for ZnO is given by [81]

$$\boldsymbol{d} = \begin{bmatrix} 0 & 0 & 0 & 0 & -11.34 & 0 \\ 0 & 0 & 0 & -11.34 & 0 & 0 \\ -5.43 & -5.43 & 11.67 & 0 & 0 & 0 \end{bmatrix} \text{pC/N}\,. \tag{3.3.2}$$

This relationship can also be expressed in terms of the deformation, $\boldsymbol{S}_{jk}$, that the material experiences, as

$$\boldsymbol{P}_i = \boldsymbol{e}_{ijk} \cdot \boldsymbol{S}_{jk}\,, \tag{3.3.3}$$

where $\boldsymbol{e}_{ijk}$ is the tensor of piezoelectric strain constants for the material. In Voigt notation, $\boldsymbol{e}$ for ZnO is given by [81]

$$\boldsymbol{e} = \begin{bmatrix} 0 & 0 & 0 & 0 & -0.48 & 0 \\ 0 & 0 & 0 & -0.48 & 0 & 0 \\ -0.573 & -0.573 & 1.32 & 0 & 0 & 0 \end{bmatrix} \text{C/m}^2\,. \tag{3.3.4}$$

This effect occurs in materials in which a distortion of the crystal structure by an external force can lead to the creation of dipole charges, due to the charge distribution within said crystal structure. This results in a measurable electrical potential across the crystal.

When an electric field, $\boldsymbol{E}_i$, is applied across a material, resulting in a stress or deformation, this is known as the inverse piezoelectric effect, and is described by $\boldsymbol{\sigma}_{jk} = \boldsymbol{d'}_{ijk} \cdot \boldsymbol{E}_i$, or $\boldsymbol{S}_{jk} = \boldsymbol{e'}_{ijk} \cdot \boldsymbol{E}_i$, where $\boldsymbol{d'}_{ijk}$ and $\boldsymbol{e'}_{ijk}$ are the inverse piezoelectric tensors for stress and strain, respectively. In general, we have

$$\boldsymbol{D}_i = \boldsymbol{d}_{ijk} \cdot \boldsymbol{\sigma}_{jk} + \boldsymbol{\varepsilon}^{\sigma}_{ij} \cdot \boldsymbol{E}_j \,, \tag{3.3.5}$$

$$\boldsymbol{S}_{ij} = \boldsymbol{C}^{E}_{ijkl} \cdot \boldsymbol{\sigma}_{kl} + \boldsymbol{e'}_{kij} \cdot \boldsymbol{E}_k \,, \tag{3.3.6}$$

where $\boldsymbol{D}_i$ is the electric flux density, $\boldsymbol{\varepsilon}^{\sigma}_{ij}$ is the permittivity of ZnO in a zero, or constant, stress field, and $\boldsymbol{C}^{E}_{ijkl}$ is the stiffness tensor in a zero, or constant, electric field. In the following, we will first neglect the inverse piezoelectric effect, and consider it later in Chapter 8.

3.3.1 The Piezotronic Effect in Grain Boundaries

Since ZnO is not only piezoelectric, but also an n-type semiconductor, it is possible for the stress induced polarisation charges to affect the double Schottky barrier that occurs at the grain boundary. This occurs due to polarisation charges generated at the grain boundary, which form a charge sheet that alters the profile of the potential barrier at the grain boundary by modifying the total interface charge, Q_i. This can result in either an increase, or a decrease in the current flow through the grain boundary.

The piezotronic effect, originally suggested in [18], is based on the piezoelectric polarisation charge induced at the grain boundary when a mechanical stress is applied. This charge will add to (or subtract from) the interface charge, Q_i, thus resulting in an increase (or decrease) of the barrier height. This effect can be expressed by a modification of the switching voltage as

$$V_c = \frac{1}{2\gamma}\left(\frac{Q_i + Q_P}{\varepsilon_r \varepsilon_0}\right)^2 , \tag{3.3.7}$$

where

$$Q_P = \boldsymbol{n}_{gb} \cdot (\boldsymbol{P}_l - \boldsymbol{P}_r) \,, \tag{3.3.8}$$

$\boldsymbol{n}_{gb}$ is the grain boundary normal and $\boldsymbol{P}_l$ and $\boldsymbol{P}_r$ are polarisation vectors defined in the two grains on the left and on the right hand side of the boundary, respectively. Furthermore, the polarisation vectors are obtained from the stress field, $\boldsymbol{\sigma}$, and the piezoelectric tensor, $\boldsymbol{d}$,

in the respective grain as in Equation 3.3.2. The effect thus depends on the reciprocal crystallographic orientations of the two grains sharing the boundary, as well as on the strength and orientation of the stress field. The scripts used to calculate this are given in Appendices A.2 and A.3. Note, furthermore, that not just the barrier height, but also the interface charge is affected by the presence of mechanical stress at the boundary. This is because of the implicit relationship between the two, which is now given by the self-consistent solution of (3.1.11), (3.2.2) and (3.3.7).

The simplest case featuring the piezotronic effect is that of a uniform uniaxial stress applied to a bicrystal with co-aligned grain orientations. The three possible bicrystal configurations corresponding to head-to-head, tail-to-tail and head-to-tail grain orientations, respectively, are depicted in Figure 3.3.1.

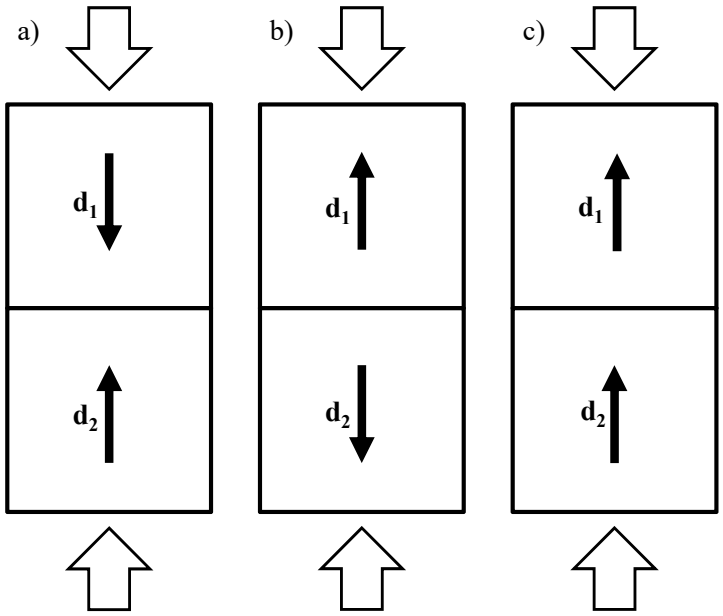

Figure 3.3.1.: Schematic representation of a bicrystal under uniaxial stress with head-to-head (a), tail-to-tail (b) and head-to-tail (c) reciprocal grain orientations, respectively.

According to the above coupling mechanism, when a compressive stress is applied, the grain boundary conductivity will increase in the head-to-head configuration and will decrease in the tail-to-tail configuration. In the head-to-tail case, the piezoelectric charges induced on both sides of the boundary cancel, such that the total polarisation charge (3.3.8) is zero. Thus, no piezoelectric coupling occurs. This behaviour was recently confirmed experimentally by Raidl et al. [20], who performed uniaxial compressive tests on low-voltage varistors made of only few (<1000) grains. Raidl's experiment was designed such that, considering the grain size and electrode spacing, only 2-3 grains were included between the electrodes. Thus, assuming that the electric current flows through a single grain boundary only, the single grain boundary

characteristics could be measured. The measurement data revealed the presence of three grain boundary types and their corresponding mechanical sensitivities.

3.3.2 The Macroscopic Influence of the Piezotronic Effect

When mechanical stress is applied to a polycrystal, both an increase in the leakage current and a decrease in the coefficient of non-linearity can be observed. This occurs as a result of the distribution of barrier heights introduced to the polycrystal by piezoelectric modification. Another consequence of this effect is the degradation of the switching effect observed in the non-linear region of the polycrystal's IV-characteristic, when compared to that of the polycrystal when no external stress is applied. These same effects can occur as a result of residual thermal stresses remaining within the crystal after manufacturing.

Stress-induced shifts in the IV-behaviour of ZnO varistors have been measured experimentally using uniaxial or compressive stresses [82–84]. For both cases, the degree of non-linearity and the switching voltage can be seen to fall with increasing compressive stress. Furthermore, microstructural inhomogeneities such as non-uniform grain sizes or non-equiaxed grains can result in local stress concentrations within samples subjected to external stress, which exacerbate the effects described above.

In the case of polycrystalline varistor structures, the effect of piezoelectric coupling becomes substantially more complicated as it now depends on the stress distribution within the material as well as on the distribution of individual grain orientations. The overall stress sensitivity of such materials can be quantified by means of the effective gauge factor:

$$GF = \frac{1}{S}\frac{R_0(V) - R(V)}{R_0(V)}, \tag{3.3.9}$$

where $R(V)$ and $R_0(V)$ are the effective electrical resistances of the material with and without applied stresses, respectively, and S is the strain.

4 Equivalent Network Model

4.1 Equivalent Circuit Representation of the Grain Boundary

In the equivalent network model, the electrical response of a single grain boundary is represented by the electrical circuit shown in Figure 4.1.1.

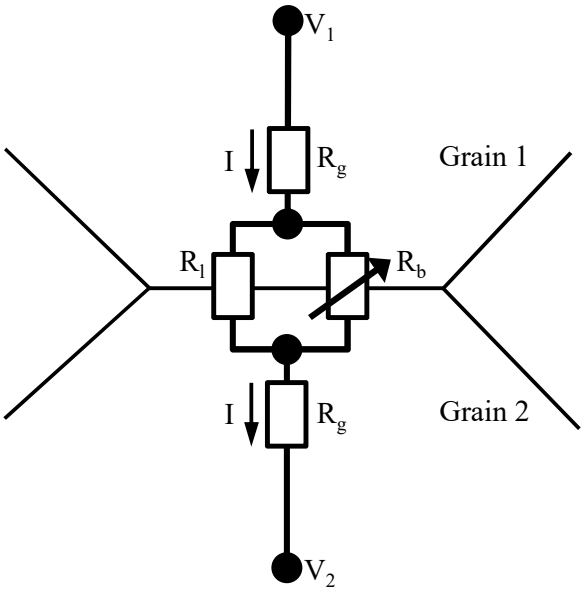

Figure 4.1.1.: Lumped electrical model using an equivalent electrical circuit to represent current flow at a grain boundary.

This approach is similar to the one used by Vojta et al. [24] and Bavelis et al [23]. It incorporates the non-linear grain boundary resistance, R_b, defined by (3.2.5), a large Ohmic resistance, R_l, accounting for leakage currents across the boundary, as well as the contribution of the grain bulk resistivity to the total current, represented by the lumped resistance R_g. Each of the grain centres is associated with a voltage node, whereas the grain boundary is represented by a current branch of the circuit. Given an electrical conductivity, λ_g, for the bulk ZnO, the ballast resistances, R_g, are estimated as $R_g = \frac{d_g}{a_B \lambda_g}$, where d_g is the grain size and a_B the grain boundary area. Similarly, the leakage resistance is assumed to be $R_l = \frac{1}{a_B \lambda_l}$, where λ_l is the specific leakage conductivity of the boundary, as shown in Table 4.1.1.

For any given voltage, V, the non-linear grain boundary resistance, $R_b(V)$, is determined by (3.2.5). In order to compute the potential barrier, the coupled equations (3.1.11), (3.2.2)

and (3.3.7) are solved using a symbolic computation package [102] (see Appendix A.1). The parameters used in the calculation are displayed in Table 4.1.1, and are, essentially, the same as those used in [71]. Nevertheless, note that the model is independent of the choice of these parameters. For a given grain boundary composition, these parameters can also be obtained from first principle calculations of the electronic structure, such as those previously reported by Sato et al. [46].

Table 4.1.1.: Grain boundary parameters used in the model. λ_l and λ_g denote the specific leakage conductivity of the grain boundary surface and the bulk conductivity of the grain ZnO, respectively.

$\epsilon_\xi(\mathrm{eV})$	$\xi_i^n(\mathrm{eV})$	$N_\nu(\mathrm{cm}^{-3})$	$N_{i0}(\mathrm{cm}^{-2})$	$E_i(\mathrm{eV})$	$\Delta E_i(\mathrm{eV})$
3.133	0.0	9×10^{17}	9×10^{12}	2.2	0.15
$\epsilon_\nu(\mathrm{eV})$	$a_B(\mu\mathrm{m}^2)$	ε_r	$\lambda_l(\mathrm{S}/m^2)$	$\lambda_g(\mathrm{S}/m)$	
3.18	100	8.81	10^{-3}	2	

Hereby, we assume a single dominant bulk state, ϵ_ν, and a Gaussian distribution of the interface states as $N_{i0}(E) \sim \exp[(E-E_i)^2/\Delta E_i^2]$. Otherwise, the grain boundary parameters are similar to those in [23, 58]. All energies are given relative to the valence band edge. The resulting solutions for the grain boundary potential and the interface charge density vs. voltage are depicted in Figure 4.1.2.

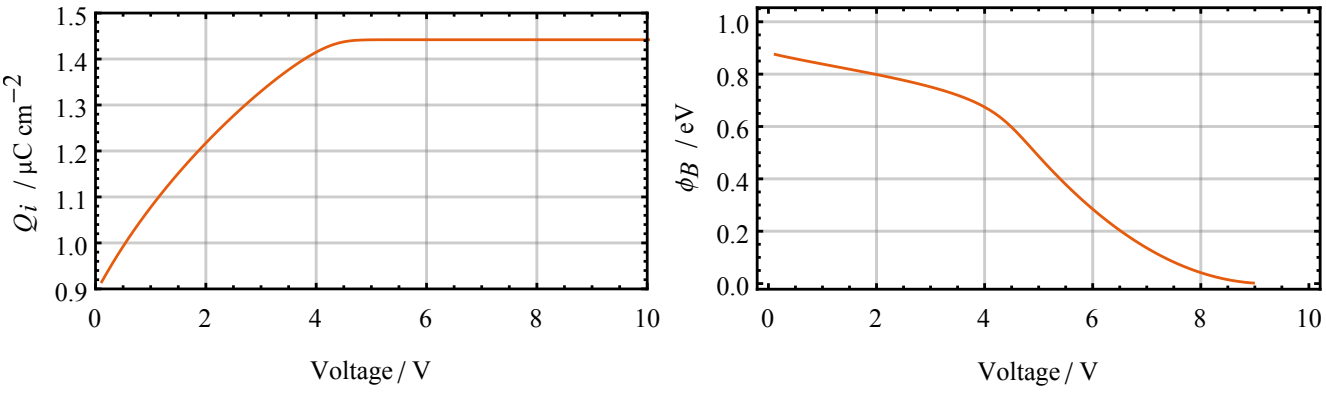

Figure 4.1.2.: Interface charge (left) and potential barrier (right) solutions for a single grain boundary.

In the stress-free case, these results are identical to those reported in [58]. As indicated in [58], the potential barrier is initially pinned at a nearly constant value at lower voltages and it decays rapidly above a certain threshold of the applied voltage.

Based on the geometry of the polycrystal, the equivalent electrical network is constructed (see Figure 4.2.1 (left)). Each grain volume is associated with a voltage node of the network, and the individual grain boundaries are associated with the elementary networks depicted in Figure 4.1.1. The grain boundary resistances are obtained by performing a self-consistent solution of the model equations (3.1.11), (3.2.2) and (3.3.7), and incorporated into a SPICE network model (see Appendices A.4 and A.5). The solution of the non-linear network equations that provide the total current through each grain boundary for an applied external voltage is realised by means of the software package LTSpice [103]. The current flowing through each grain can then be represented by dividing the sum of all 'positive' currents flowing into a grain by the total current flowing through the polycrystal, thus giving the current passing through each grain as a proportion of the whole.

4.2 Mesoscopic Network Model

For more complicated varistor structures, the equivalent electrical network is based on a Voronoi tessellation representing the polycrystalline microstructure of the varistor sample as suggested in [22]. Many open questions about these microstructural effects, such as fluctuations in the barrier height, local variation in the switching voltage and the influence of grain size distribution, are difficult to investigate experimentally. Simulation techniques have proven invaluable in this area and past research has had great success using microstructures generated from Voronoi tessellations to investigate 2D random networks [7, 22, 24, 69, 70, 85–100].

A Voronoi tessellation is produced by first generating a set of points in space. These are commonly referred to as the 'seeds' of the tessellation. Every seed defines a Voronoi cell, which is made up of all points in space closer to the cell's seed than any other. When all points in the space have been assigned to a Voronoi cell, the space will have been partitioned into as many separate cells as there are seeds, with each cell boundary being equidistant between the seeds of the two neighbouring cells.

The Voronoi tessellations used in this work were produced using a free source software package called Neper [101]. Further to the standard Voronoi tessellation, Neper contains a regularisation algorithm that removes the large number of small edges and faces commonly found in a pure Voronoi tessellation. This is achieved without changing the overall grain morphology, and helps to produce microstructures that are both more realistic and less likely to

produce computational singularities. Furthermore, the package provides a random realisation of grain orientations with a uniform distribution within the sample volume.

Such a network consists of a large number of grain boundary sub-circuits where the IV-characteristic of each grain boundary depends on the local voltage it experiences. An exemplary equivalent network for a 5-grain varistor structure is shown in Figure 4.2.1 (left). In Figure 4.2.1 (right), a second example can be seen, showing the resulting Voronoi structure for a varistor sample of dimensions 200×300 μm^2 and an average grain size of 10 μm, containing a total of 600 grains.

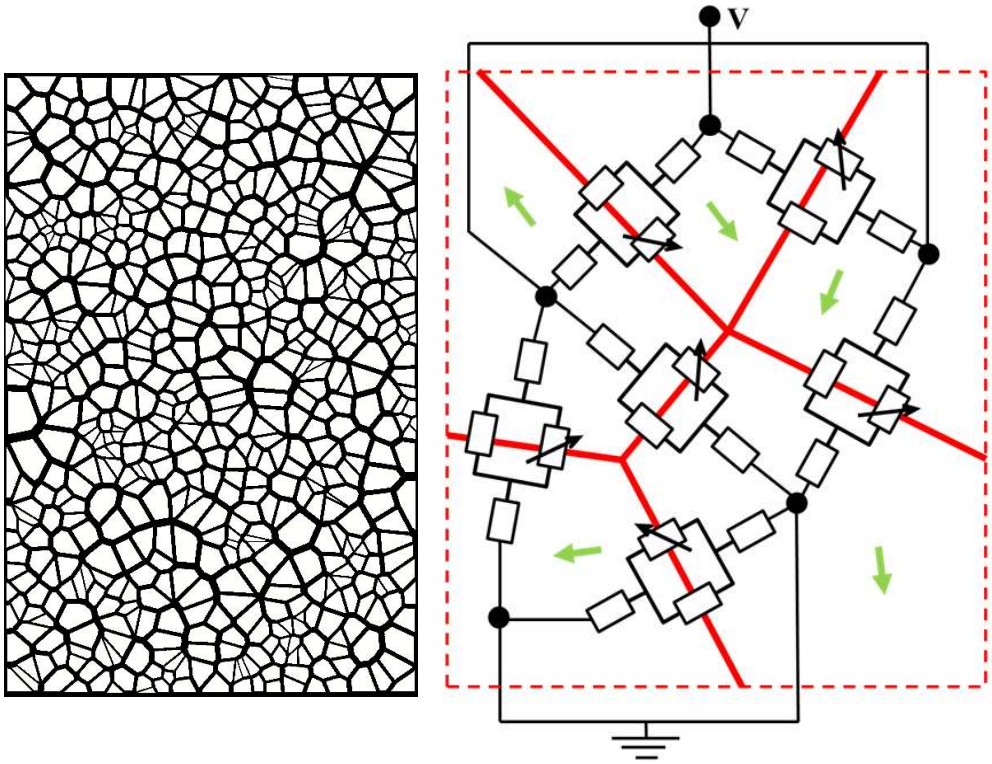

Figure 4.2.1.: Left: 2D varistor microstructure generated by Voronoi tesselation. Right: Exemplary equivalent network for a 5-grain varistor. The polycrystalline geometry obtained by Voronoi tessellation is depicted by red lines. To each of the grains, a principal axis orientation is randomly assigned (green vectors).

The individual grain boundaries are arranged in a disordered network, where the net current density across the entire polycrystal deviates from that of the local current density at any given grain boundary.

5 Mesoscopic Electrical Characteristics of Zinc Oxide Varistors

5.1 Simulation of Current Flow

The current flow patterns resulting from the solution of the circuit equations for the varistor sample in Figure 4.2.1 (left) are shown in Figure 5.1.1 for applied voltages of 6 V, 60 V and 150 V. These correspond to effective electric field strengths of 0.02 MV/m, 0.2 MV/m and 0.5 MV/m, respectively. The well-known current concentration effect [85] in the non-linear varistor regime is clearly observed. This behaviour, which can be observed qualitatively in Figure 5.1.1, is quantified by Figure 5.1.2, where the IV-characteristic for the 2D varistor structure shown in Figure 4.2.1 is plotted. It displays all the basic features described in Section 2.1.

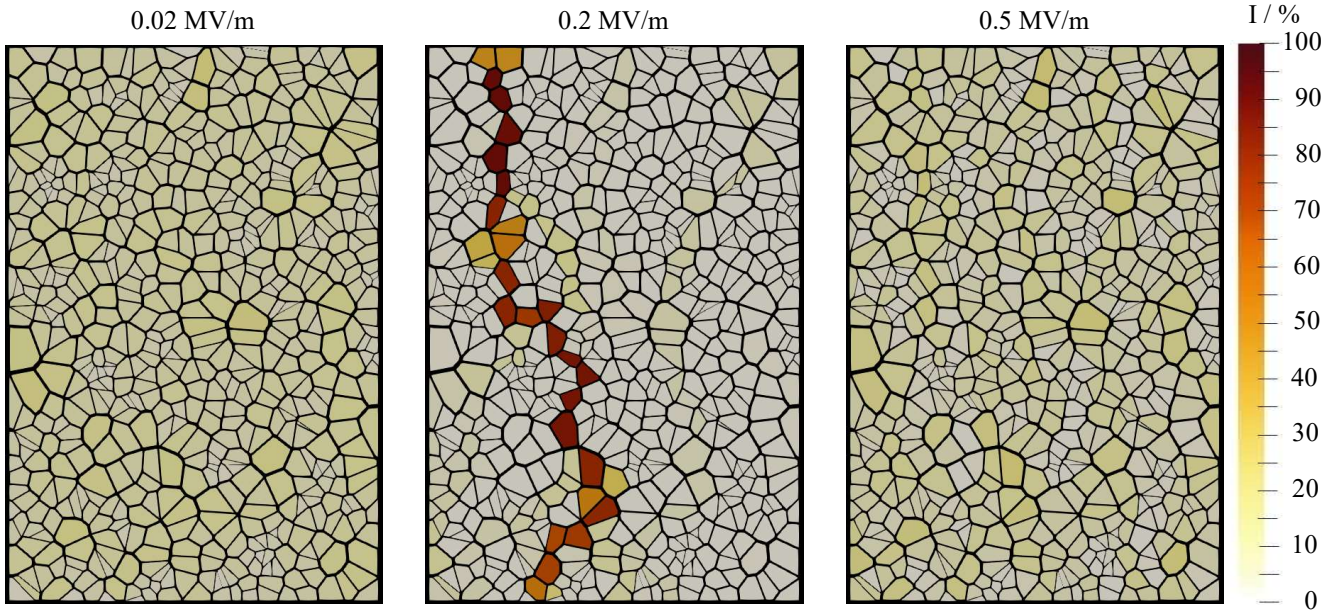

Figure 5.1.1.: Electrical current patterns for the 2D varistor sample shown in Figure 4.2.1. The current in each grain is given relative to the total current flowing through the sample, and the electrical contacts are connected to the top and bottom of the sample.

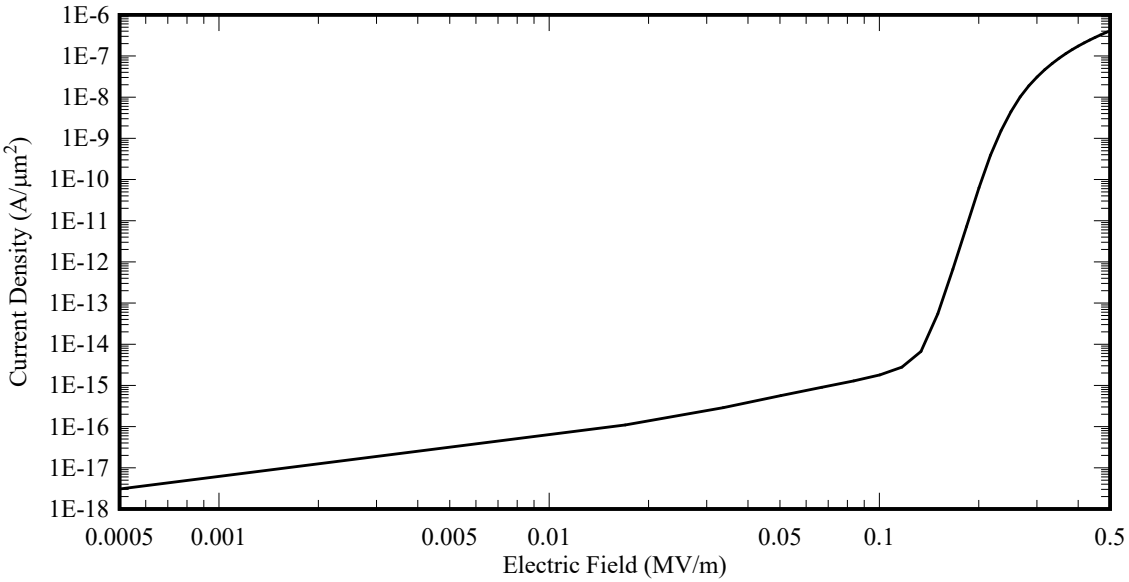

Figure 5.1.2.: IV-characteristic for the 2D varistor sample shown in Figure 4.2.1.

The current flow pattern depends on what region of the IV-characteristic the varistor is operating in. In the leakage and upturn regions, the varistor's resistance is Ohmic and there is mostly homogeneous current flow throughout the entire microstructure. In the breakdown region, the conductivity of some grain boundaries grows more rapidly than that of others due to their differing interface areas and voltage working points, for a given total applied voltage. This leads to the development of strong current filaments, such as that seen in Figure 5.1.1.

5.2 Microstructural Inhomogeneities

The presence of microscopic inhomogeneities has been addressed by several authors, pointing out that many of the grain boundaries may be either Ohmic, possess a poor non-linearity, or even be insulating [104–106]. In the past [22, 85–87], network simulations with a large proportion of grain boundaries that are modelled without varistor behaviour have been considered. These grain boundaries can be entirely insulating, have a linear, Ohmic resistance, or simply display poor varistor behaviour with a low degree of non-linearity, thus influencing the overall IV-characteristics. Such effects occur in real microstructures due to the segregation of secondary phases, such as spinel, pyrochlor, or Bi_2O_3.

So far, the grain boundary properties have been assumed to be identical for all boundaries in the model. However, due to the manufacturing process, an inhomogeneous distribution of the grain boundary properties within the material is expected.

For the investigation of the influence of inhomogeneities on the electrical characteristics, we adopt the approach used in [22, 23, 25, 85–87], where a fraction of the grain boundaries,

uniformly distributed within the sample volume, is assumed to be Ohmic. In the following, we consider the same 2D-varistor sample described in Figure 5.1.1 and introduce a number of Ohmic boundaries into the model. The specific conductivity of the grain boundary surface is chosen as $\lambda_o = 10^3$ S/m^2, and is thus much higher than its leakage conductivity (see Table 4.1.1). Current flow maps within the sample for the two cases, with and without Ohmic boundaries, are depicted in Figure 5.2.1.

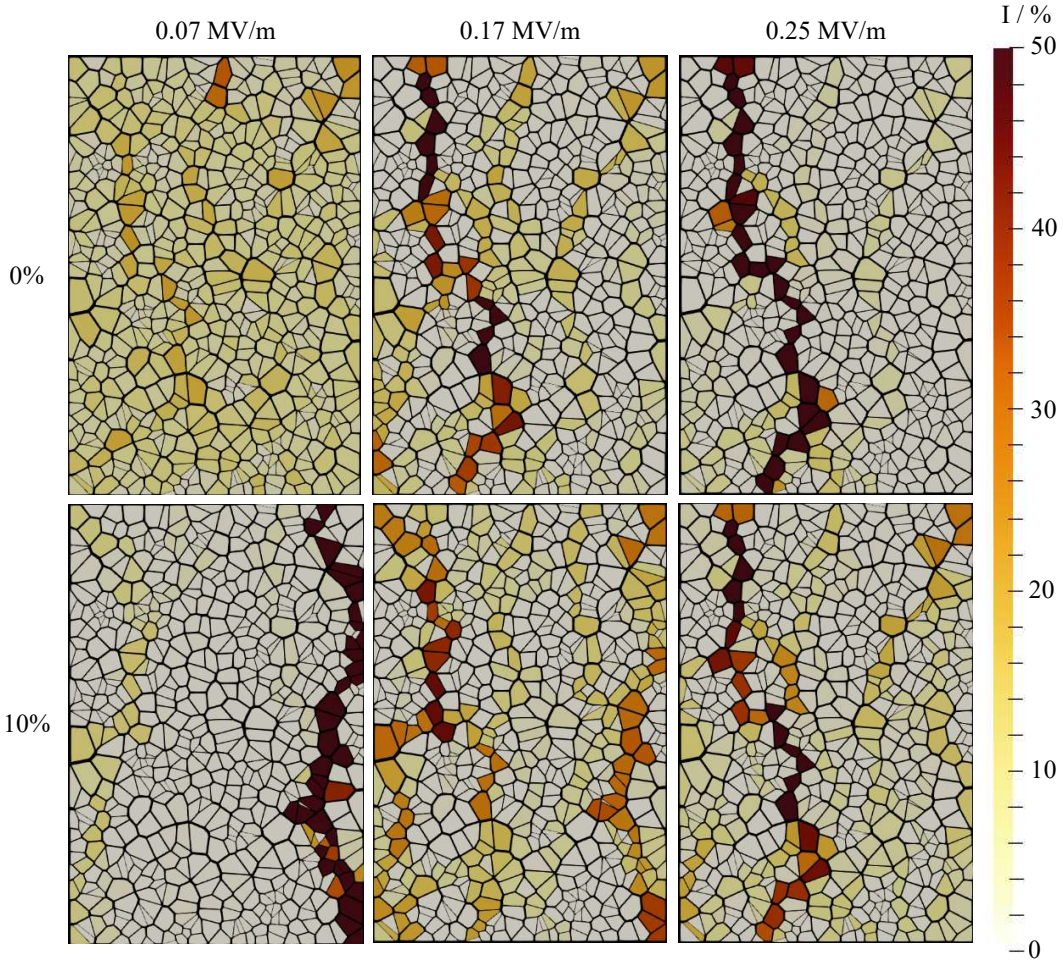

Figure 5.2.1.: Current flow maps in the presence of Ohmic boundaries. The cases of a homogeneous (top) and an inhomogeneous material (bottom), containing 10% Ohmic boundaries, are depicted.

Upon inspection of Figure 5.2.1, it can be seen that, in the case of homogeneous material, the same current pathways form and intensify with increasing voltage. This is consistent with the common understanding that these paths correspond to the shortest electrical paths between the top and bottom electrodes and that the topology of these paths does not depend on the applied voltage. However, when 10% of the boundaries are Ohmic, a switching effect occurs, and the paths jump to another location with increasing voltage. At low voltages the current

flows, preferentially, along routes containing many Ohmic boundaries. However, as the voltage increases, the conductivity of the varistor boundaries rapidly grows, ultimately, becoming larger than that of the Ohmic boundaries. The current 'jumps' to follow the path of least resistance, and new current paths emerge at a different location in the material.

This behaviour is reflected in the characteristic curves in Figure 5.2.2, where the IV-characteristics of the sample for different concentrations of Ohmic boundaries are shown. For higher concentrations of Ohmic boundaries, the curves feature several oscillations in the active varistor region. Each of the bumps corresponds to a different pathway topology, characterised by a different non-linearity coefficient. The comparatively flat regions in the curve correspond

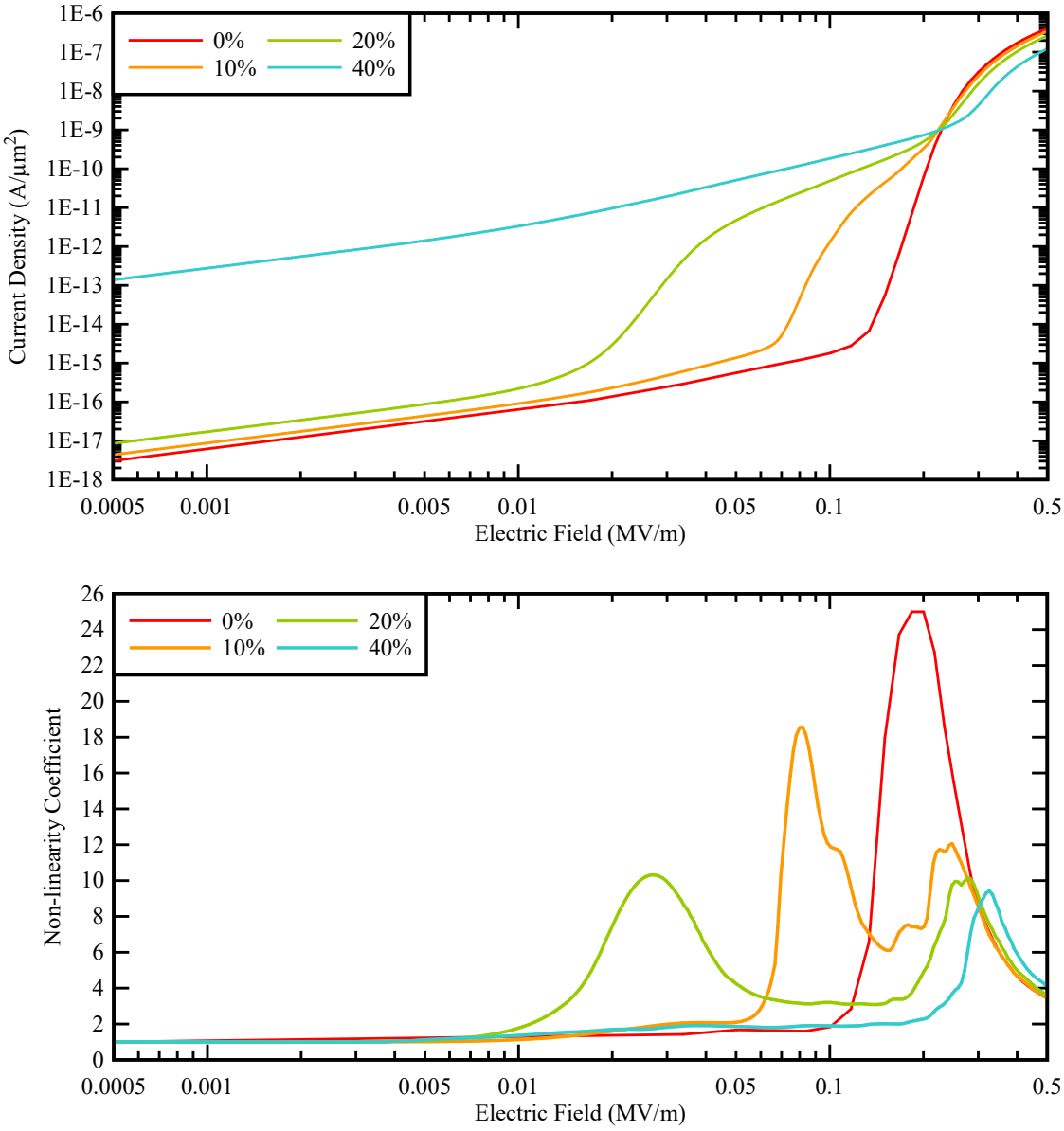

Figure 5.2.2.: IV-characteristic and non-linearity coefficients for the varistor sample in Figure 4.2.1 (right) for different concentrations of Ohmic boundaries.

to intermediate states, where two or more current paths are coexisting, before a new dominant path is settled. The latter manifests as a second breakdown of the varistor current at a higher voltage in the IV-curve. This effect was previously observed in [21,23,107], where the resulting characteristics for inhomogeneous materials were referred to as "double-knee" characteristics.

5.3 Influence of 3D Geometry

Numerical simulations for 3D-varistor structures in the absence of mechanical stress have been previously presented in [23]. Important differences between the effective 2D and 3D characteristics were observed. This was attributed to the percolative nature of current flow in the polycrystal. The amount of conductive paths available to electric currents in 3D is substantially higher than in 2D geometry. Furthermore, the collision probability for these paths to join into higher-current paths (cf. [62]) is smaller in the 3D case. 3D simulations are thus necessary for a realistic characterisation of varistor materials.

For the investigation of conductivity in the 3D case, a varistor sample with the same aspect ratio and average grain size as in the 2D model in Figure 5.1.1 is chosen. This results in a 3D polycrystalline structure consisting of 12000 grains (see Figure 5.3.1). The grain boundary properties are described by the same parameters given in Table 4.1.1.

Figure 5.3.1 shows a typical current flow map within the sample in the current breakdown region. Compared to the 2D case (cf. Figure 6.3.2), a larger number of current paths is observed. The 3D geometry provides more ways for the current to find favourable pathways to the bottom electrode. Since these paths are connected in parallel, each of them is carrying a smaller portion of the total current compared to the 2D model.

As shown in Figure 5.3.2, the 3D sample is characterised by a lower switching voltage compared to the corresponding 2D curves. Contrary to intuition, 3D current paths are electrically shorter than in 2D, or, equivalently, it is easier for the current to find highly conducting pathways in 3D than in 2D geometry. As a result, the voltage seen by the single boundaries is high, thus leading to a lower effective switching voltage.

The non-linearity coefficient of the 3D material is shown in Figure 5.3.2. Due to the reduction in the switching voltage, the effective non-linearity of the 3D sample is lower compared to the 2D case.

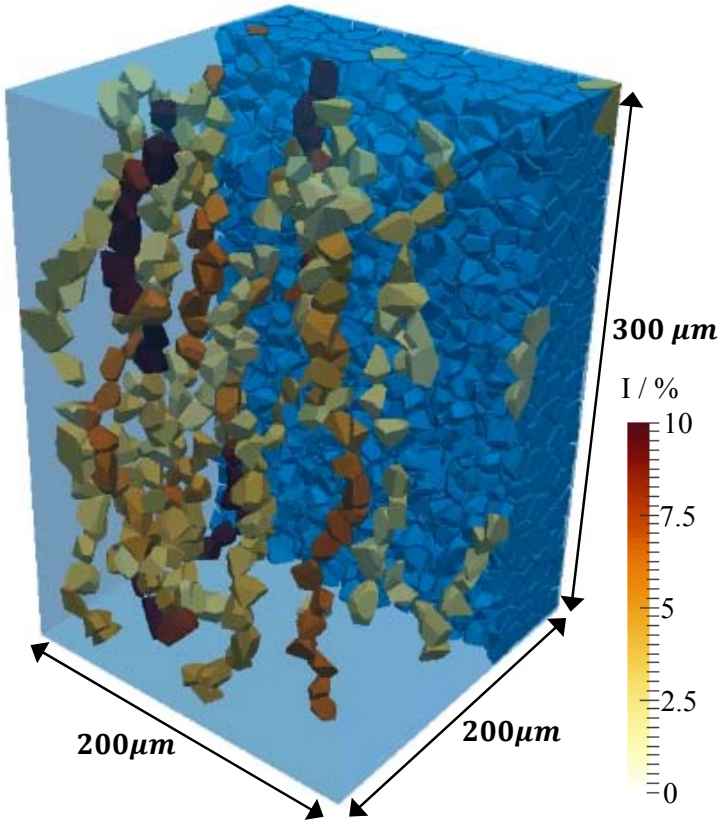

Figure 5.3.1.: Current flow map for current bearing grains in the non-linear region of the 3D varistor sample, superimposed upon a cross section of the microstructure.

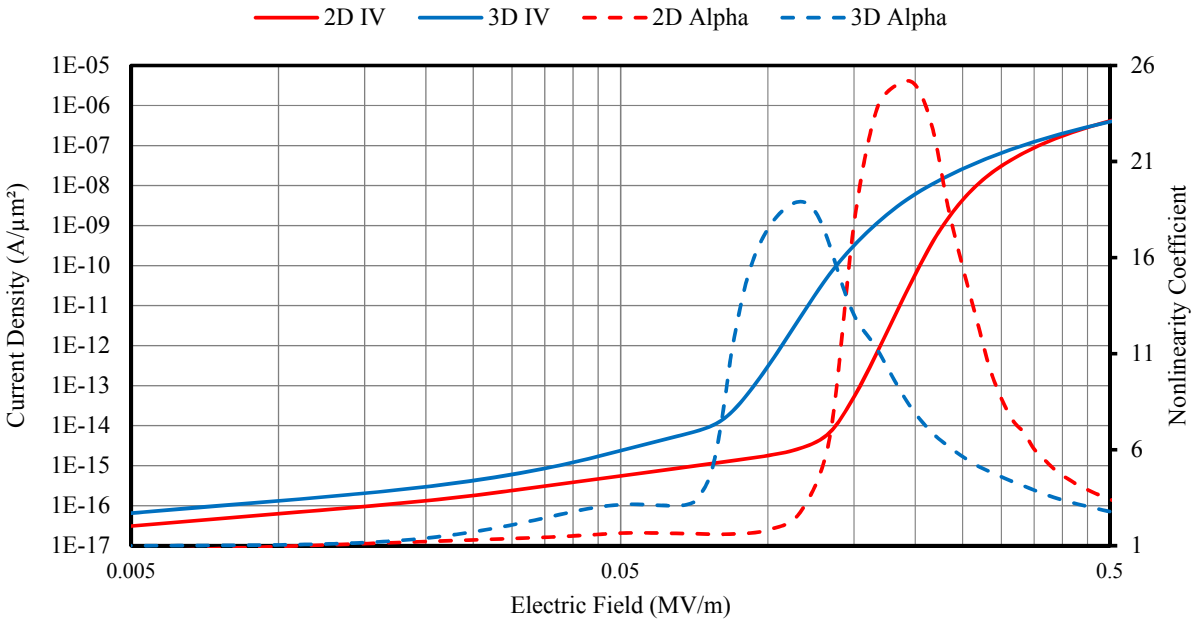

Figure 5.3.2.: IV-characteristics and non-linearity coefficients for the 3D polycrystal shown in Figure 5.3.1, compared to the 2D-characteristic from Figure 5.1.2.

6 Modelling of Mechanical Stress Sensitivity in Varistors

6.1 Single Grain Boundary Model

The piezoelectric influence of mechanical stress on charge transport through ZnO grain boundaries was introduced in Section 3.3.1. However, until now, this effect has not been accounted for in equivalent electrical network simulations.

When considering the effect of mechanical stress, we assume that the mechanical stress is uniformly distributed within a grain volume. For ZnO, this assumption is justified by the comparatively high stiffness of the crystal [107]. With this simplification, the unique mechanical condition of a grain boundary is defined solely by the two pairs $(\boldsymbol{\sigma}_1, \boldsymbol{d}_1)$ and $(\boldsymbol{\sigma}_2, \boldsymbol{d}_2)$ of the stress and piezoelectric tensors, respectively, characterizing the two grains sharing the boundary.

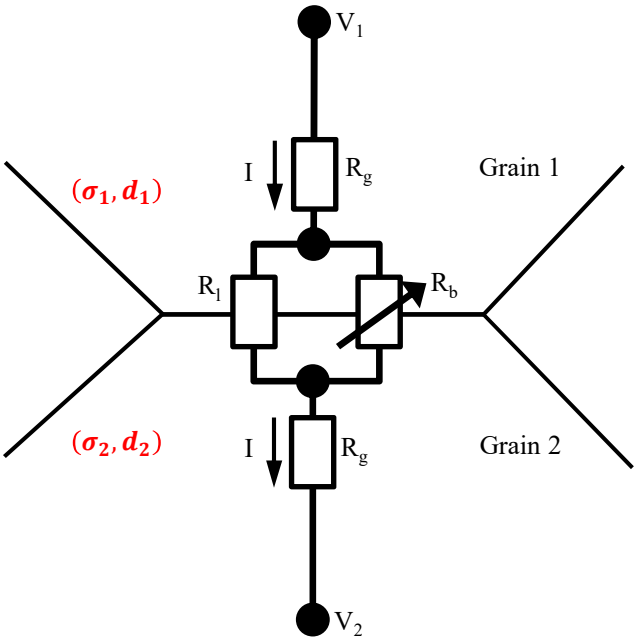

Figure 6.1.1.: Equivalent circuit representation of the bicrystal from Figure 4.1.1, characterised by the stress fields $\boldsymbol{\sigma}_1$ and $\boldsymbol{\sigma}_2$, and the piezoelectric tensors $\boldsymbol{d}_1$ and $\boldsymbol{d}_2$, in each of the two grains.

The stress-dependent solutions for the grain boundary potential and the interface charge vs. voltage are depicted in Figure 6.1.2 (cf. Figure 4.1.2). The calculations are performed exemplarily for the case when the crystallographic orientations of the two neighbouring grains are normal to the grain boundary and pointing in opposite directions in a head-to-head configuration (cf. Figure 3.3.1). A uniaxial compressive as well as tensile mechanical stress field is assumed in the direction normal to the boundary.

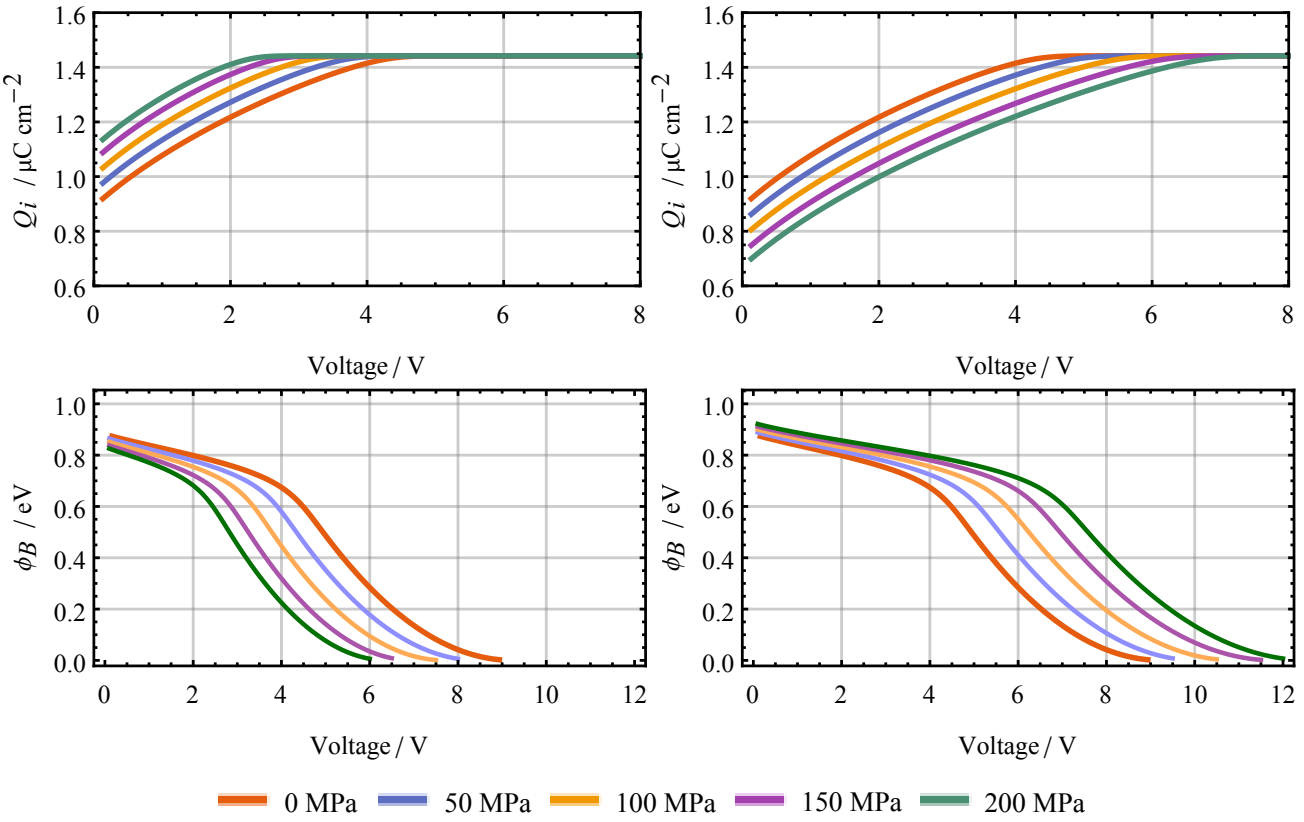

Figure 6.1.2.: Potential barrier (bottom) and interface charge (top) solutions for a single grain boundary. This is shown for compressive stress (left) and for tensile stress (right).

The curves reveal the strong effect of mechanical stress. As expected, for compressive stresses, the barrier height decreases with increasing stress, whereas, in the tensile case, the barrier increases. Nevertheless, this effect is strongly non-linear, as it depends on the voltage applied to the boundary.

The calculation of each grain boundary resistance for every possible stress condition, grain orientation and grain boundary voltage is computationally extremely demanding. For numerical efficiency, the following implementation procedure is adopted. Since the on-the-fly calculation

of the self-consistent solution to equations (3.1.11), (3.2.2) and (3.3.7) for many values of Q_P is a prohibitively complex task, the following fitting function is used to approximate Q_i as

$$Q_i(V) = \begin{cases} a + be^{-cV^p}, & V < V_B \\ a + be^{-cV_B^p}, & V \geq V_B \end{cases}, \tag{6.1.1}$$

where a, b, c, p and V_B are fitting parameters that depend on the polarisation charge, Q_P, and, by extension, also depend on the local stress state. Using the known set of parameters for a given Q_P, the corresponding Q_i can be rapidly obtained. As can been from Figure 6.1.3, the fit is very close to the direct numerical solution.

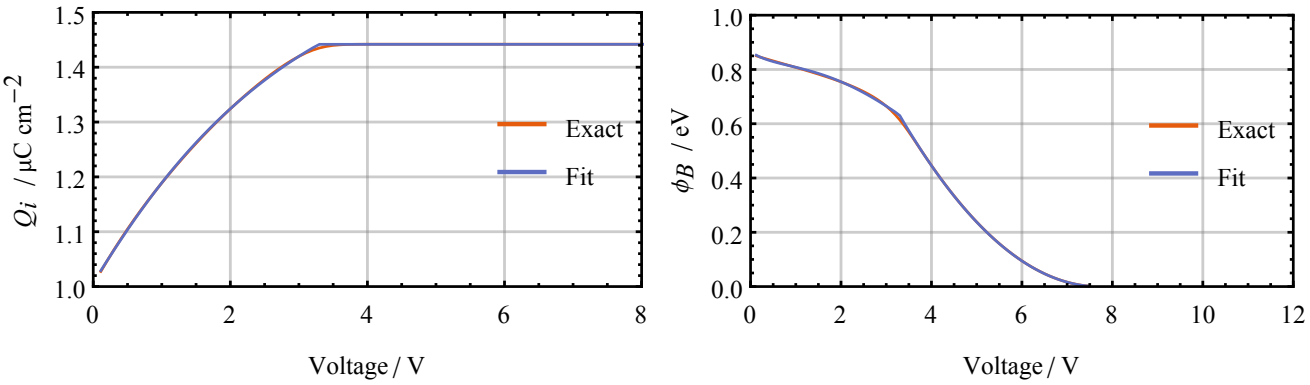

Figure 6.1.3.: Comparison between the exact and parametrised solution for Q_i (left) according to (6.1.1), and the resulting ϕ_B (right). The result is shown for a Q_P of -0.125 μCcm^{-2}, corresponding to a stress of 100 MPa when applied to a single grain boundary.

In order to be able to consider general polycrystalline configurations and arbitrary mechanical stresses, these parameters must be tabulated with respect to Q_P. First, the solution of the coupled equations (3.1.11), (3.2.2) and (3.3.7), describing the grain boundary model, is performed once at the beginning of the simulation for different values of Q_P in the range of interest. Based on this result, the parameters defining the approximation in (6.1.1) are fitted and tabulated in a look-up table for each value of Q_P. This procedure is carried out using the script, which can be found in Appendix A.1.

Thus, given an arbitrary grain boundary voltage, grain orientations and the local stress tensor solutions Q_P can be computed and Q_i can subsequently be determined on-the-fly by interpolating values from the look-up table. Given Q_i, the grain boundary potential, ϕ_B, can be calculated directly. In order to cope with more complicated polycrystalline varistor structures, composed of larger equivalent circuit models, these tables are incorporated into each individual grain boundary sub-circuit file, thus resulting in a IV-characteristic for each grain boundary that

depends on the local mechanical stress distribution. The 3D plot shown in Figure 6.1.4 gives an overview of how ϕ_B is modified by both V and Q_P.

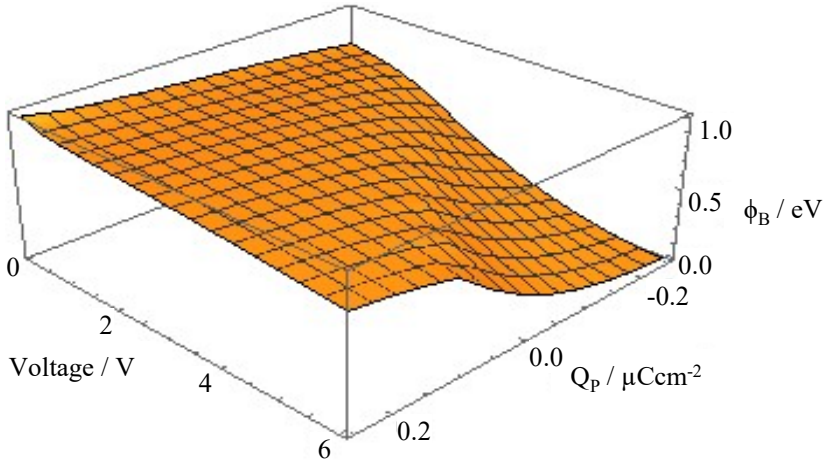

Figure 6.1.4.: 3D plot of the ϕ_B's dependency on both V and Q_P.

6.2 Solution of the Mechanical Problem

The mechanical equilibrium condition in the material reads,

$$-\mathrm{div}\,\boldsymbol{\sigma} = \boldsymbol{f}_m, \tag{6.2.1a}$$

$$\sigma_{ij} = C_{ijkl}S_{kl} - \beta_{ij}(T - T_0), \tag{6.2.1b}$$

where $\boldsymbol{f}_m$ is the applied force density, $\boldsymbol{C}$ is the stiffness tensor, $\boldsymbol{S}$ is the strain, $\boldsymbol{\beta}$ is the thermal expansion tensor and T is the temperature. The stiffness tensor for a hexagonal type ZnO crystal in the Voigt two-index notation is assumed as [107],

$$\boldsymbol{C} = \begin{bmatrix} 210 & 120 & 105 & 0 & 0 & 0 \\ 120 & 210 & 105 & 0 & 0 & 0 \\ 105 & 105 & 211 & 0 & 0 & 0 \\ 0 & 0 & 0 & 43 & 0 & 0 \\ 0 & 0 & 0 & 0 & 43 & 0 \\ 0 & 0 & 0 & 0 & 0 & 44 \end{bmatrix} \mathrm{GPa}\,. \tag{6.2.2}$$

Furthermore, the coefficient of thermal expansion in the Voigt two-index notation for a ZnO crystal with principal axis pointing in the z-direction is assumed as

$$\boldsymbol{\beta} = \begin{bmatrix} 4.31 \\ 4.31 \\ 2.49 \\ 0 \\ 0 \\ 0 \end{bmatrix} \mu\mathrm{K}^{-1}. \tag{6.2.3}$$

Given a Voronoi tessellation to describe the polycrystal geometry, a FEM mesh is generated with the open source program Gmsh [108], and the strain-stress equations (6.2.1a) and (6.2.1b) are solved numerically by FEM, using the software package Elmer [109]. In order to couple the mechanical model to the electrical model, the piezoelectric modification of the interface charge, Q_P (3.3.8), is calculated from the results of the FEM simulation. For this, the polarisation vectors P_l and P_r of the two grains sharing the boundary are determined from the local stress solution of the FEM model and the predefined piezoelectric tensors of the two respective grains. The resulting Q_P is then used to obtain the potential barrier from tabulated values, as described above. Finally, given the potential barrier $\phi_B(V)$, the non-linear and stress-dependent grain boundary resistance, $R_b(V)$, can be determined directly from the Richardson-Dushman equation (3.2.5).

6.3 Mechanical Modulation of IV-Characteristics

6.3.1 Bicrystals

In the following, we consider the effect of applied, compressive uniaxial stress on a cubic ZnO-bicrystal of size 10×10×20 μm^3. Using this structure, a compressive stress in the range 50-200 MPa is externally applied. Three different grain configurations are considered. In case (a), the two grains are both oriented in the z-direction as in a head-to-head configuration (cf. Figure 3.3.1a). In case (b), the c-axis of one of the grains is rotated by 90°. In case (c), both grains are again oriented in the z-direction, but pointing as in a head-to-tail configuration (cf. Figure 3.3.1c).

The results for the IV-characteristics are shown in Figure 6.3.1. As expected, in the head-to-tail case, the IV-curves are not affected by the applied stress (Figure 6.3.1c). The piezoelectric coupling is completely absent. In the other two cases, a sizeable loss of non-linearity is observed.

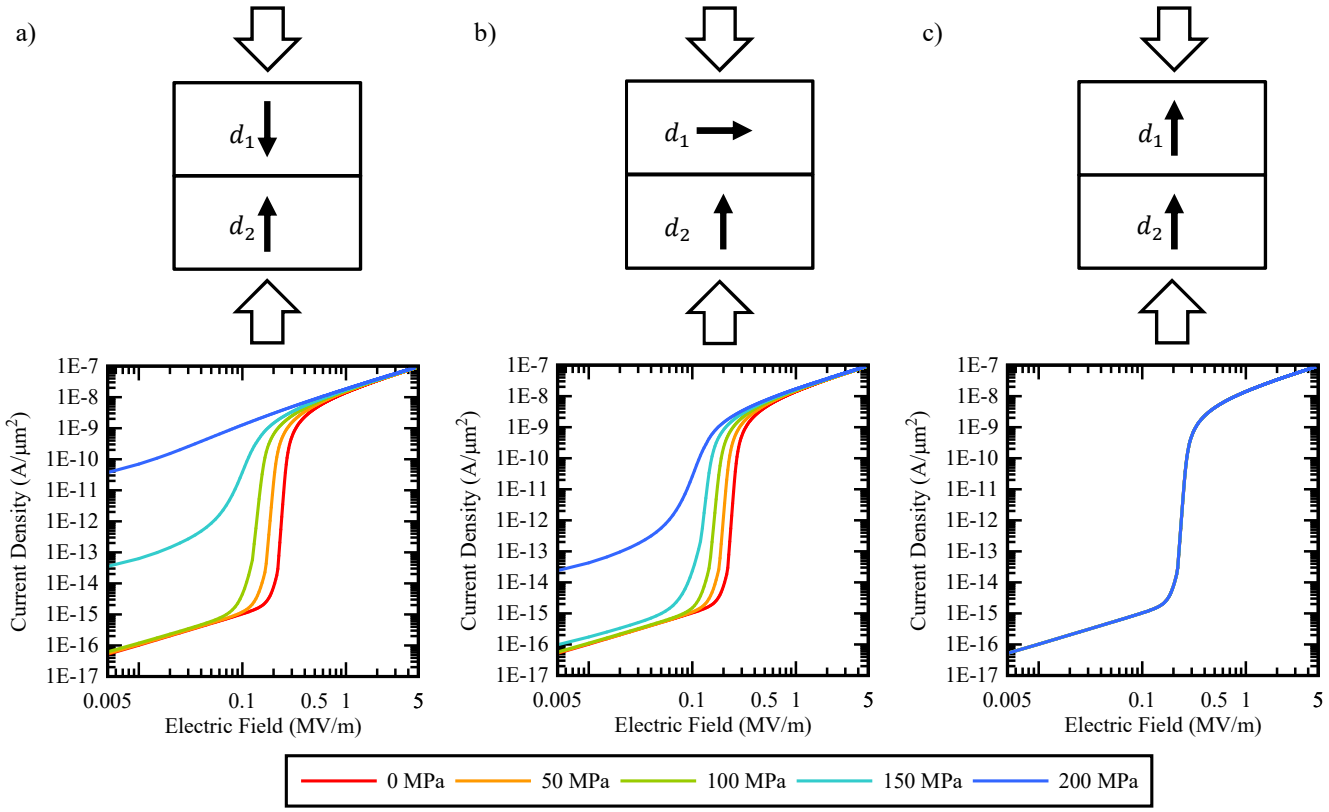

Figure 6.3.1.: IV-plots showing the stress sensitivity of the bicrystal for the following orientations: (a) head-to-head, (b) grain orientations forming a 90° angle and (c) head-to-tail.

Furthermore, the varistor switching voltage is shifted to lower values. This effect is more obvious in the head-to-head case corresponding to the stronger jump of the polarisation field at the grain boundary. For an applied stress of 200 MPa, the varistor property is completely lost and the bicrystal features an essentially linear behaviour, corresponding to the Ohmic conductivity of the bulk ZnO crystal.

6.3.2 Polycrystals

For the polycrystalline case, we first consider a 2D polycrystal of size 200×300 μm^2 with an average grain size of 10 μm. The computed stress distribution in this sample, for an applied uniaxial stress of 200 MPa in the vertical direction is depicted in Figure 6.3.2 (left). Furthermore, the current flow pattern resulting from the numerical solution of the circuit equations for an applied external voltage of 5 V is shown in Figure 6.3.2 (right). The current concentration effect, described in Section 5.1, remains. However, the topology and intensity of the current concentration effect is different.

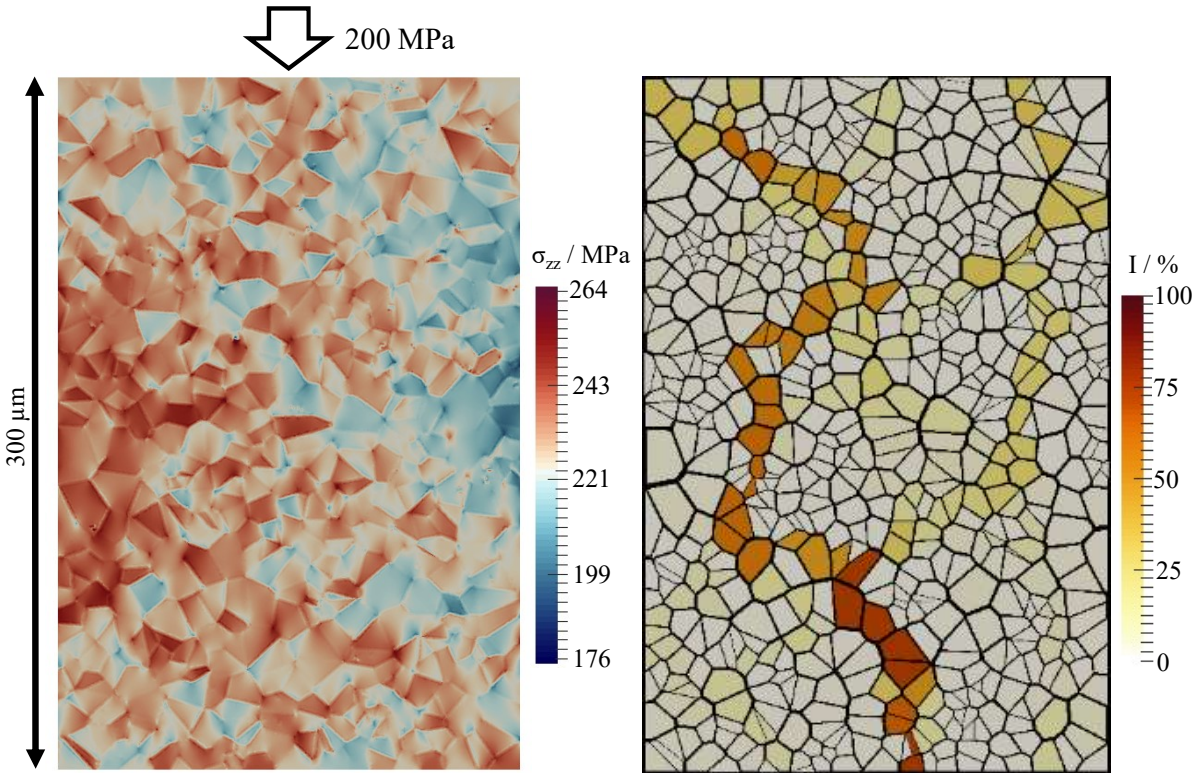

Figure 6.3.2.: Mechanical stress distribution and current flow map for the non-linear region of a 2D polycrystal of size 200×300 μm and average grain size of 10 μm when a uniaxial compressive stress of 200 MPa is applied (left). Current pattern in the sample for an applied voltage of 5 V. The current in each grain is given relative to the total current flowing through the sample.

In Figure 6.3.3 (top), additional current flow patterns are shown for different applied voltages and stresses in order to illustrate the effect of applied stress. The current concentration effect is observed for all considered cases. However, the switching voltage, for which this effect starts to become visible, depends on the applied stress. Larger applied stresses result in a reduction in the switching voltage. Furthermore, the length and position of the dominant current path are different for different applied stresses. For larger applied stresses, multiple secondary paths, characterised by a lower current density, appear. In these cases, the current distribution within the material tends to be more homogeneous, since the conductivity of individual grain boundaries becomes less non-linear with increasing stress.

A quantitative description of the effect of applied stress is provided by the effective IV-curves of the sample, shown in Figure 6.3.3 (bottom). The general behaviour of these curves is similar to that of the head-to-head bicrystalline case (cf. Figure 6.3.1), in that a compressive stress results in a reduction in the switching voltage exhibited by the polycrystal, as shown by the progressive shift of the curves to the left along the voltage-axis. However, the stress sensitivity

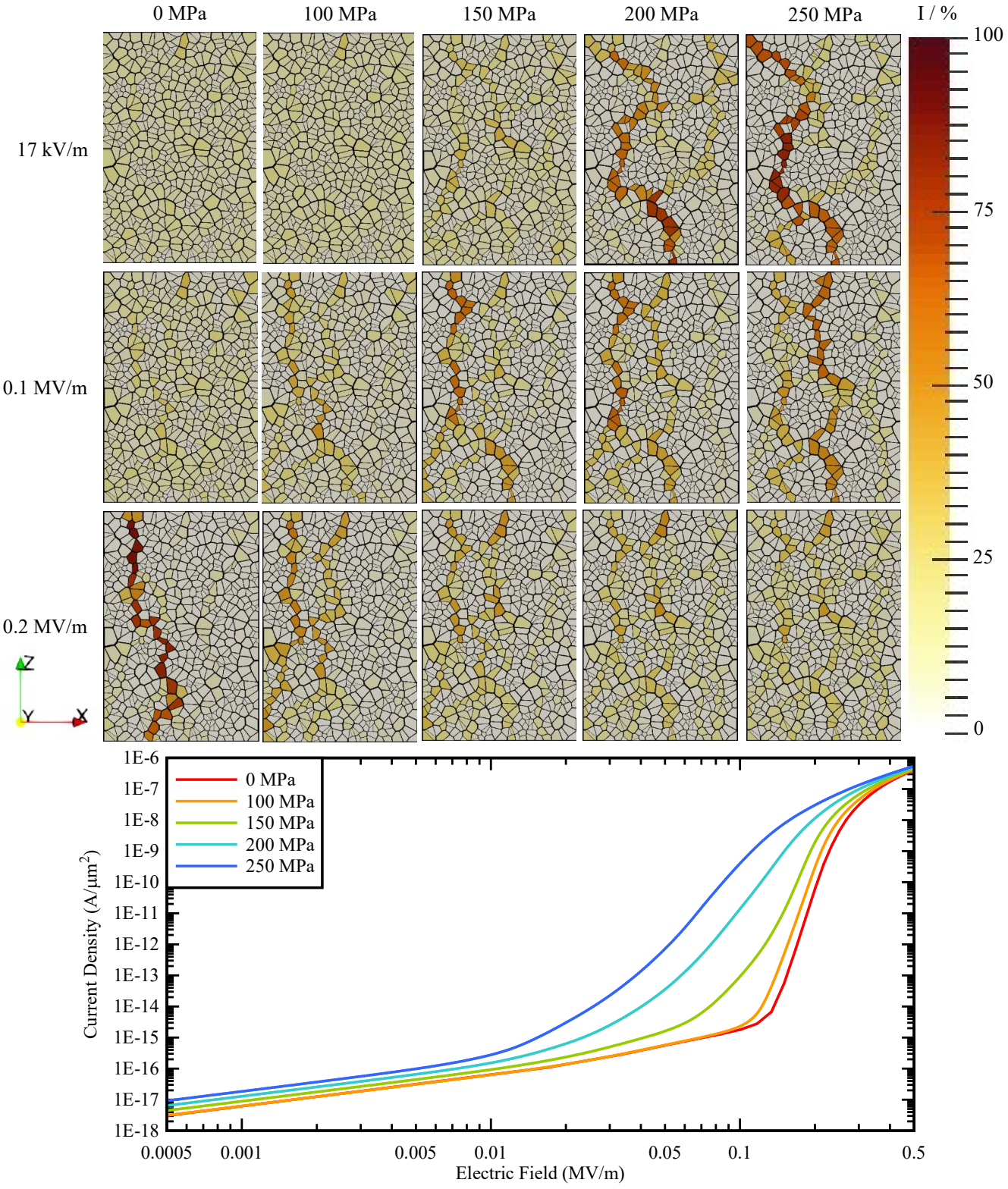

Figure 6.3.3.: Top: Current concentration for varying applied electric field strengths and uniaxial compressive stresses in a 2D polycrystal of size 200×300 μm^2 and average grain size of 10 μm. The current in each grain is given relative to the total current flowing through the sample. Bottom: The corresponding IV-characteristic.

in the polycrystalline case is lower than in the case of an ideal bicrystal. This is because there is no perfect head-to-head alignment of the grains in the polycrystal. Furthermore, the stress sensitivity of the material is only due to those grain pairs with (nearly) head-to-head orientations. The current carrying paths tend to form along these boundaries. Since the grain orientations are not perfectly aligned, the varistor property is not completely lost, even for a large applied stress. This is different to the bicrystalline case with head-to-head orientations, where a purely Ohmic conductivity is obtained for a large applied stress.

Figure 6.3.4 (left) shows the resulting gauge factor for this particular microstructure. The gauge factor is maximised when the varistor is operated close to its switching voltage. However, the switching voltage also depends on the applied stress. Thus, for a small applied stress, the gauge factor is higher at higher voltages, and vice-versa. For this particular structure, a maximum gauge factor of about 1800 is obtained for an applied stress of 100 MPa at around 60 V. This figure is more than a factor of two higher than the measured values reported in [16]. This discrepancy arises from the idealised varistor model considered in the simulations, which is 2D and does not account for microstructural inhomogeneities. The stress-induced reduction in the switching voltage is accompanied by a deterioration in the polycrystal's non-linearity. This is demonstrated in Figure 6.3.4 (right), where the non-linearity coefficient α can be clearly seen to decrease with increasing stress.

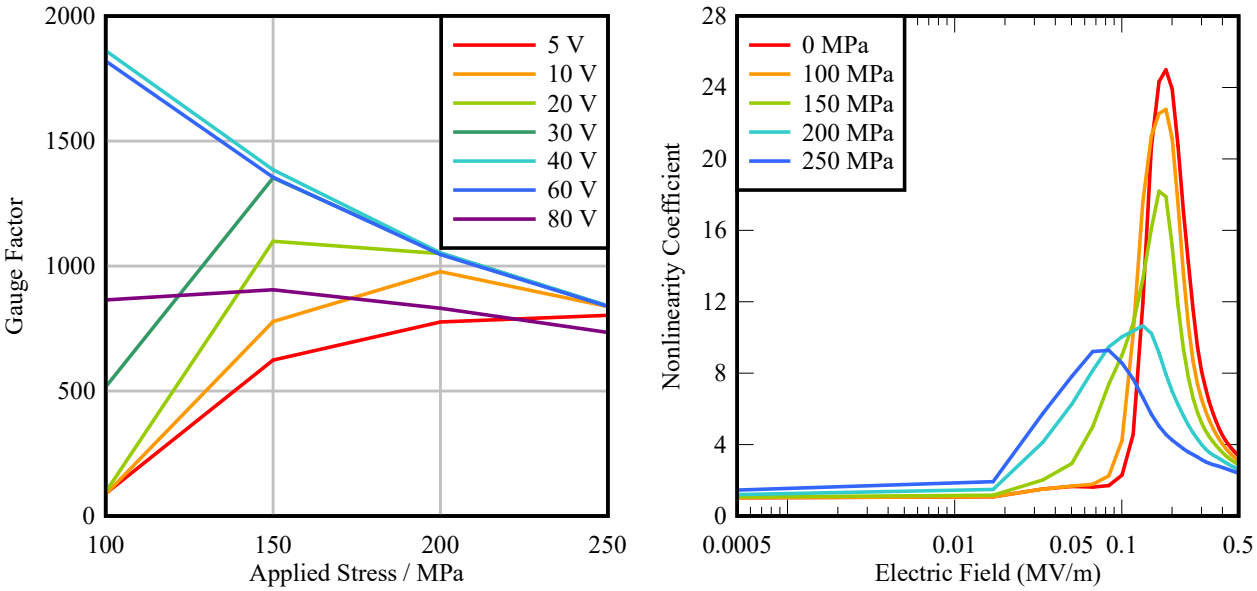

Figure 6.3.4.: Gauge factor (left) and non-linearity coefficients (right) for different applied voltages for the 2D IV-characteristics shown in Figure 6.3.3.

In Section 5.2, simulation results illustrating the effect of microstructural inhomogeneity on varistor IV-characteristics were shown. Figure 6.3.5 shows IV-characteristics for the same structure under the influence of applied stress. Applying mechanical stress to the material does

not essentially affect the "double-knee" mechanism. As in the case of homogeneous material, the overall non-linearity of the stressed material is lower, and the switching voltage shifts to lower values, compared to the unstressed one.

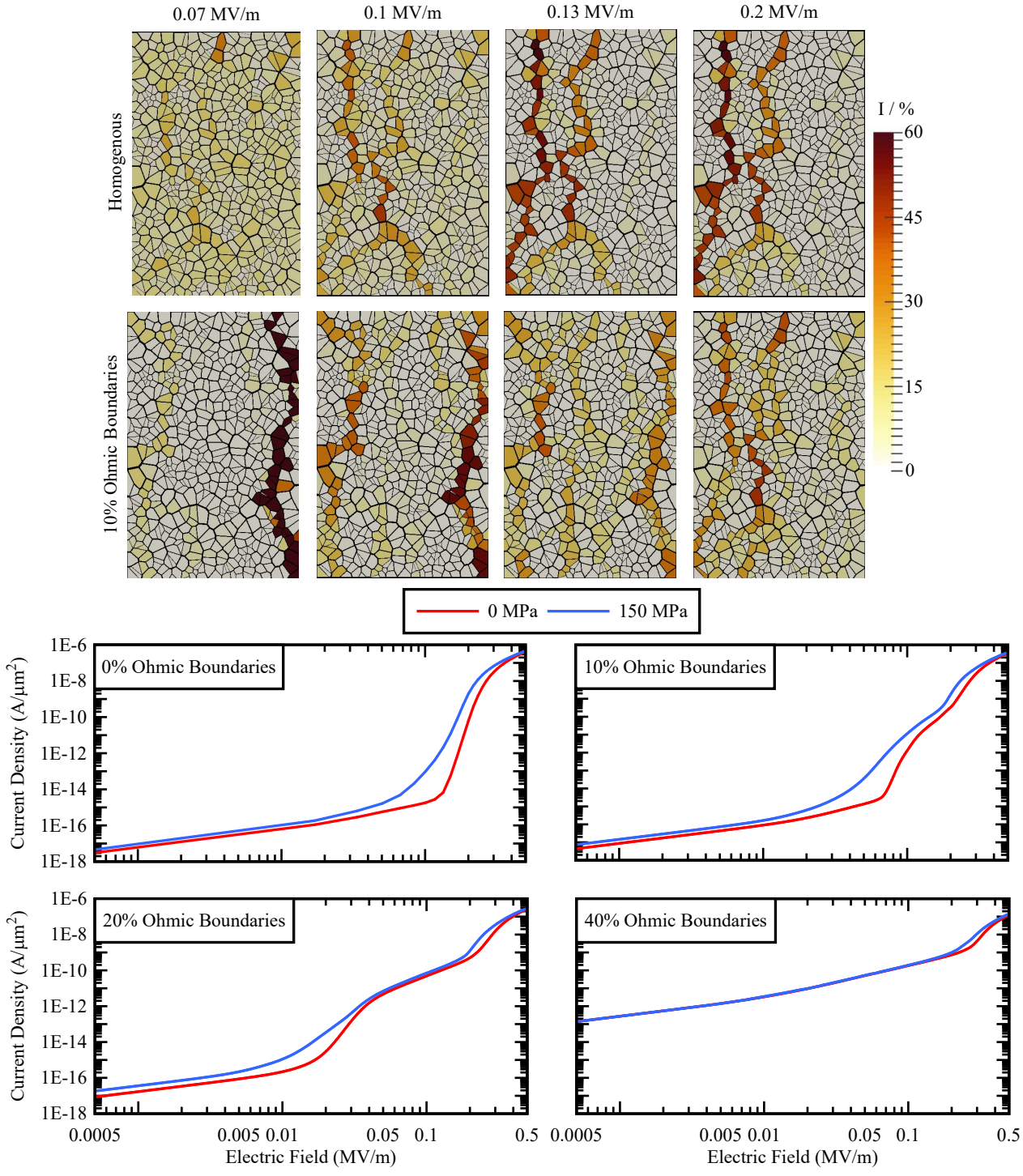

Figure 6.3.5.: Top: Current flow maps showing jumping pathways due to the presence of Ohmic boundaries. The homogeneous and inhomogeneous (10% Ohmic boundaries) cases are considered. Bottom: Influence of applied stress on the IV-characteristic of varistor samples with different concentrations of Ohmic boundaries.

6.3.3 Influence of Sample Size

One important consideration is the effect of sample size on the computed effective characteristic. In order for these characteristics to be macroscopically representative, a sample size greater than a representative volume element (RVE) must be chosen [110]. The RVE is identified by comparing simulations of different sample sizes, while keeping the average grain size and grain boundary properties unchanged. For the 2D polycrystal described in Figure 6.3.2, we consider three different samples of sizes 100×150 μm^2, 200×300 μm^2, and 400×600 μm^2. These correspond to totals of 150, 600 and 2400 grains, respectively, with an average grain size of 10 μm in all three samples. As shown in Figure 6.3.6, the results for the stress-dependent IV-characteristics converge quickly with increasing sample size. The results for the 600 grain sample are identical to those of the 2400 grain sample. In particular, the results obtained in Section 6.3.2 are macroscopically representative, since the larger sample used in the simulations is well above the RVE limit.

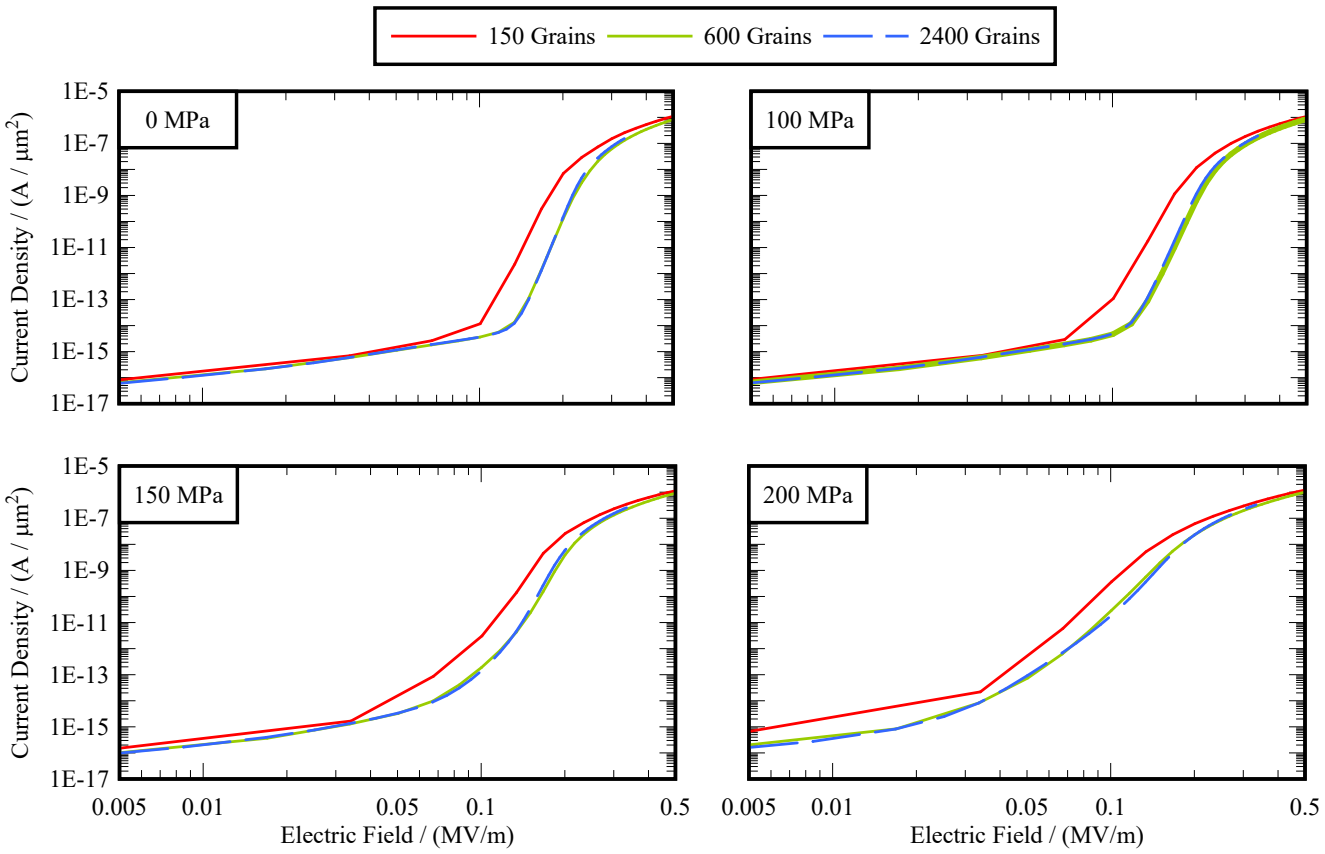

Figure 6.3.6.: Stress-dependent IV-characteristics for different sizes of the varistor sample. In all cases, the average grain size is 10 μm.

6.3.4 3D Varistor Modelling

For the investigation of the stress-dependent conductivity in the 3D case, a 3D varistor sample of dimensions 100×100×150 μm^3, with an average grain size of 10 μm is chosen. The grain boundary properties remain as defined in Table 4.1.1. The mechanical stress distribution is obtained by fully 3D FEM simulations for a random realization of the uniform distribution of grain orientations within the polycrystal. Figure 6.3.7 shows the resulting Von Mises stress distribution for an applied stress of 200 MPa.

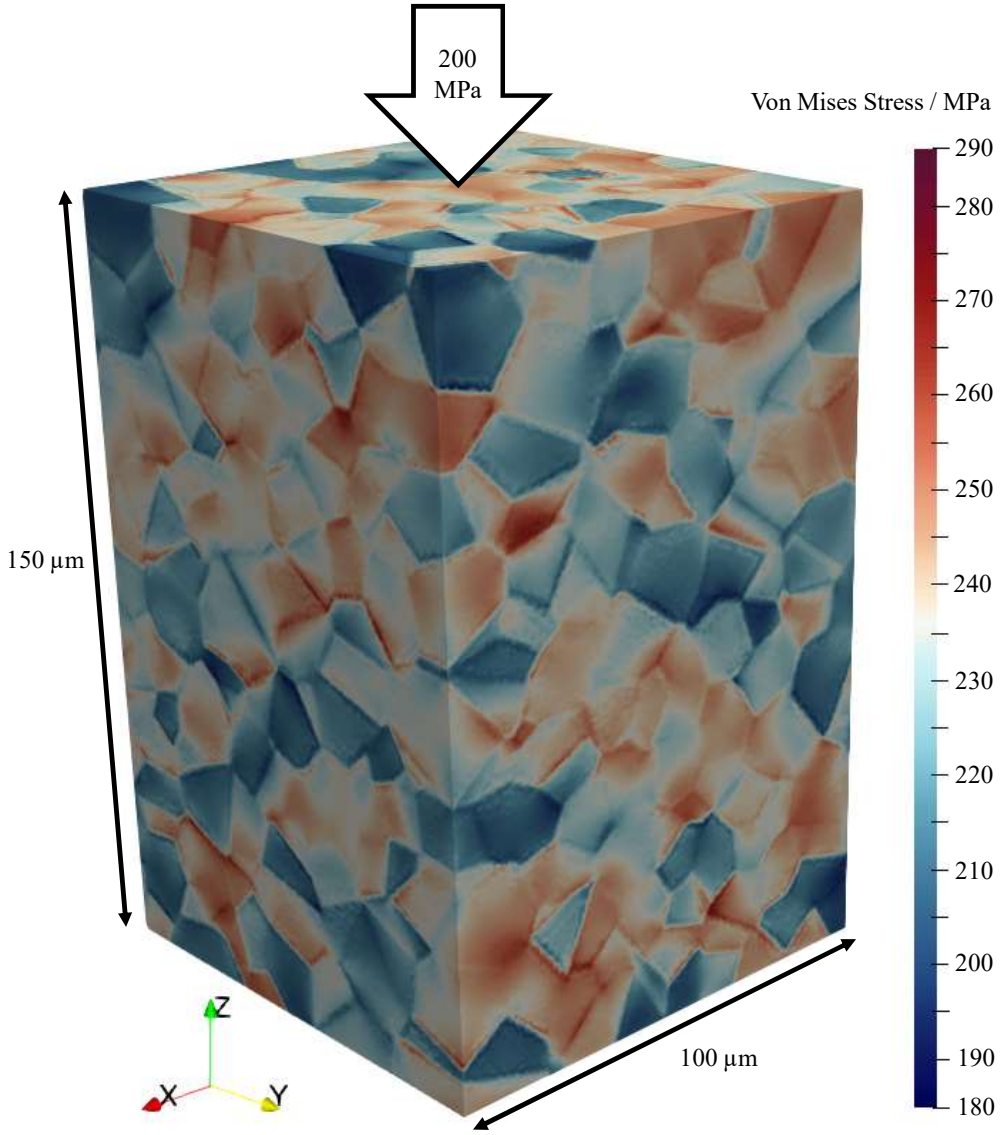

Figure 6.3.7.: Stress distribution in a 3D polycrystal of size 100×100×150 μm^3. with an average grain size of 10 μm, when a uniaxial compressive stress of 200 MPa is applied.

In Figure 6.3.8 (top), the stress-dependent IV-characteristics of the 3D sample are shown. Compared to the 2D case, the 3D sample is characterised by a lower V_c for all applied stresses.

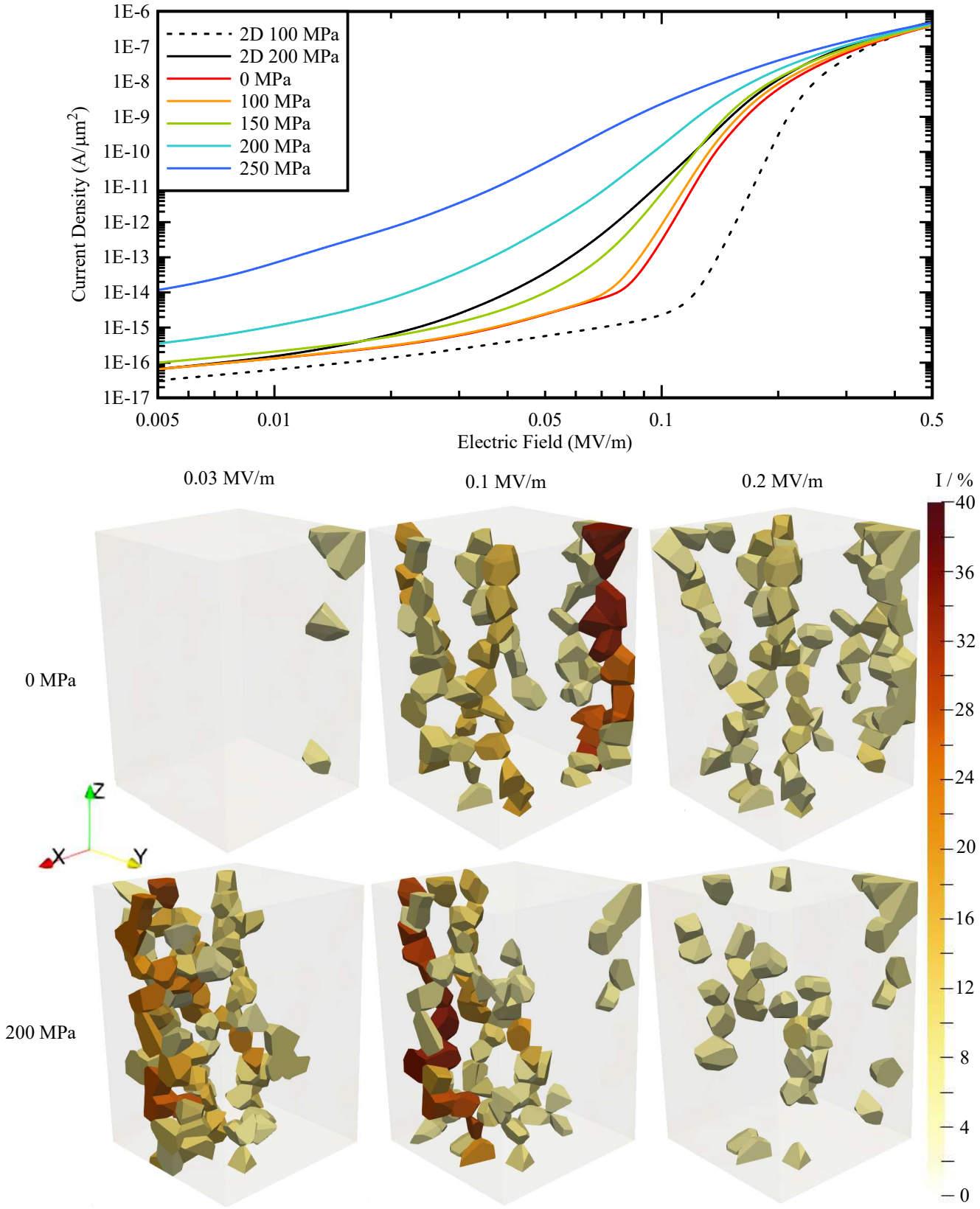

Figure 6.3.8.: Top: IV-characteristics for a 3D polycrystal of dimensions 100×100×150 μm^3, with an average grain size of 10 μm, compared to the 2D IV-characteristic from Figure 6.3.3. Bottom: Current flow paths for the characteristic shown above. Only grains carrying 5% or more of the total current are shown.

The corresponding current flow patterns are shown in Figure 6.3.8 (bottom), where the electrical contacts are applied to the top and bottom of each sample. At an effective electric field strength of 0.03 MV/m, the sample without applied stress presents a largely homogenous distribution of current throughout the polycrystal. There is no significant current concentration, since the varistor is still operating in the leakage regime. On the other hand, at the same effective electric field strength of 0.03 MV/m, the sample under an applied uniaxial compressive strength of 200 MPa has already entered the breakdown regime. This is clear to see from the concentrated current pathways that have formed within the microstructure.

As the applied voltage grows, the stress-free sample eventually progresses into the breakdown region, as can be seen from the concentrated pathways in the current flow map shown for an effective electric field strength of 0.1 MV/m. However, the sample under compression is, comparatively, closer to the upturn region. This can be seen in the current patterns for effective electric field of 0.2 MV/m, where the current distribution in the sample under applied stress is already almost homogenous. However, in the stress-free sample, some current concentration paths can still be seen.

The stress sensitivity of the 3D material is shown in Figure 6.3.9, depicting the non-linearity coefficient and gauge factor of the sample. Similarly to Figure 5.3.2, due to the reduction in the switching voltage, the effective non-linearity of the 3D sample is lower compared to the 2D case. Furthermore, the loss of non-linearity in 3D geometry leads to a decrease in the effective gauge

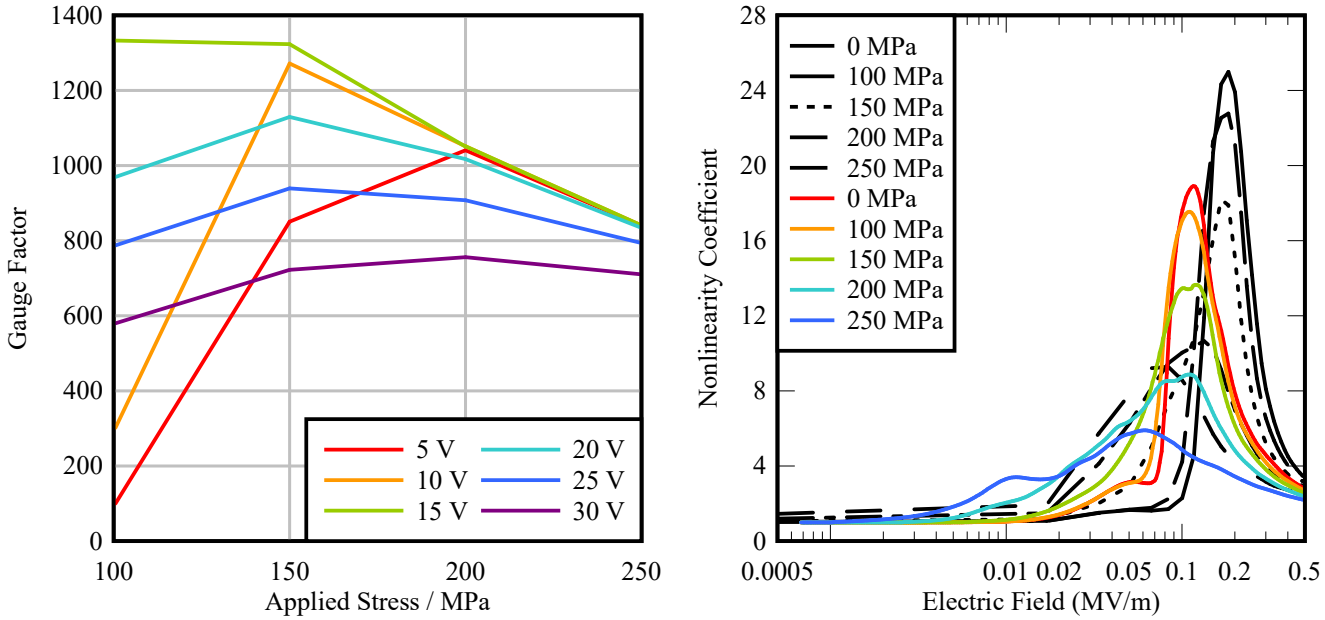

Figure 6.3.9.: Left: Gauge factors vs. applied stress in the 3D case. Right: Non-linearity coefficients for the 2D (black) and 3D (colour) IV-characteristics shown in Figure 6.3.8.

factor. The peak gauge factor obtained for this sample is now around 1300. This figure is much lower than the 2D result in Figure 6.3.4 and closer to the experimental value reported in [16]. This demonstrates the necessity of 3D simulations for accurate varistor characterisation.

Finally, it should be noted that the IV-curves computed for the 3D varistor sample are in good qualitative agreement with measurement data (cf. Figure 3 in [19]). A more detailed comparison between simulation results and measurements, however, remains beyond the scope of this work. This is primarily due to the lack of detailed knowledge on the grain boundary properties for the materials used in these experiments, where commercial varistors of unspecified dopant composition and fabrication procedure were employed.

6.4 Single Crystal-Polycrystal Structures

Keil et al. recently studied the influence of high temperature treatment during epitaxial growth on the stress sensitivity of doped ZnO-based single crystal-polycrystal-single crystal (SC-PC-SC) structures [21]. In this section, simulations are performed using SC-PC-SC geometries and the coupled model described above. These structures were created such that the crystallographic orientations of the single crystals were aligned head-to-head, as illustrated in Figure 3.3.1. The geometries considered represent a freshly bonded SC-PC-SC structure, with a smooth interface and a fine microstructure, and also an SC-PC-SC structure after heat treatment. The latter microstructure is significantly coarser, with uneven edges where the outer grains have been absorbed by the single crystal. These microstructures are illustrated in Figures 6.4.1 and 6.4.1,

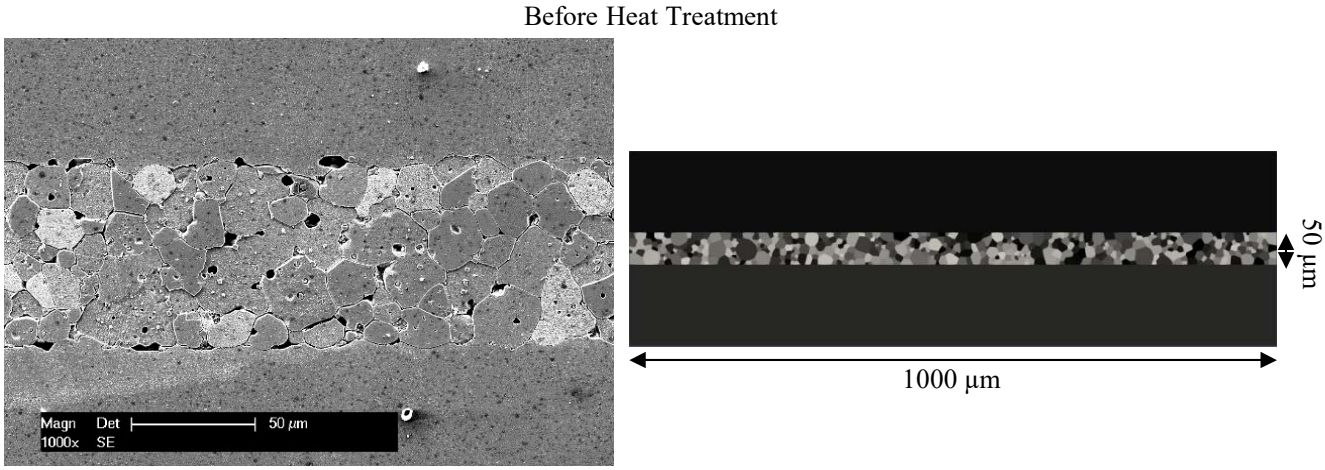

Figure 6.4.1.: Scanning electron microscope image of an SC-PC-SC interface in cross-section (left) and the corresponding SC-PC-SC sample based on Voronoi tessellation (right) before heat treatment. Experimental images provided by Keil, Rödel et al.

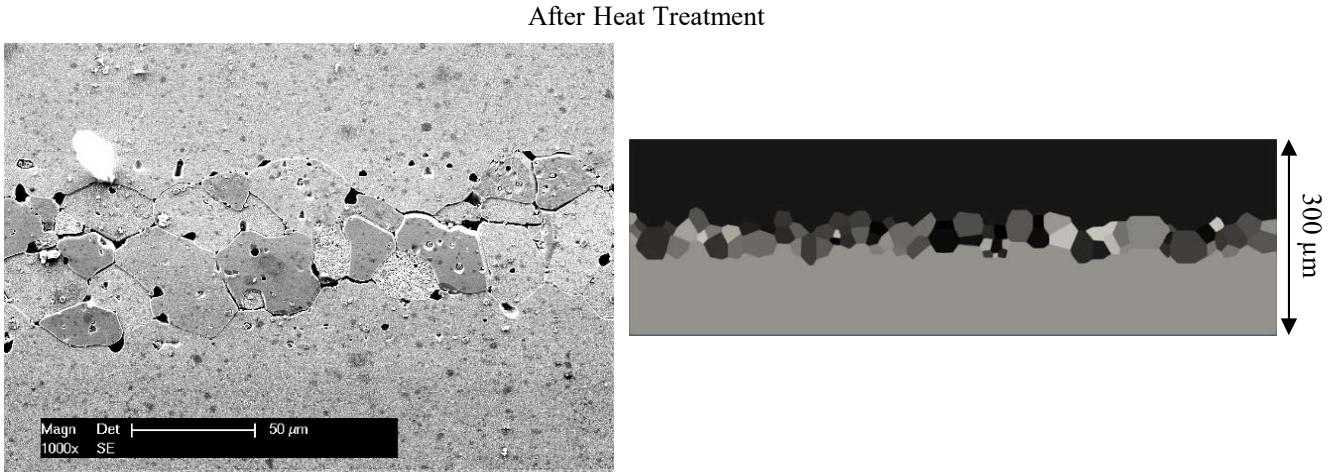

Figure 6.4.2.: Scanning electron microscope image of an SC-PC-SC interface in cross-section (left) and the corresponding SC-PC-SC sample based on Voronoi tessellation (right) after heat treatment. Experimental images provided by Keil, Rödel et al.

alongside experimental images of equivalent structures. In the figures, it can be seen that the Voronoi tessellation-based samples are geometrically similar to the experimental measurements.

In Figure 6.4.3, IV-characteristics are shown for both structures. For the untreated sample, the same current concentration effect in the breakdown region as that seen in Figure 6.3.2 is observed. As the voltage is increased, different paths form depending on where the current experiences the least resistance. However, the coarser microstructure seen in the heat-treated sample has larger grains, resulting in a few paths that must cross only one grain boundary. This

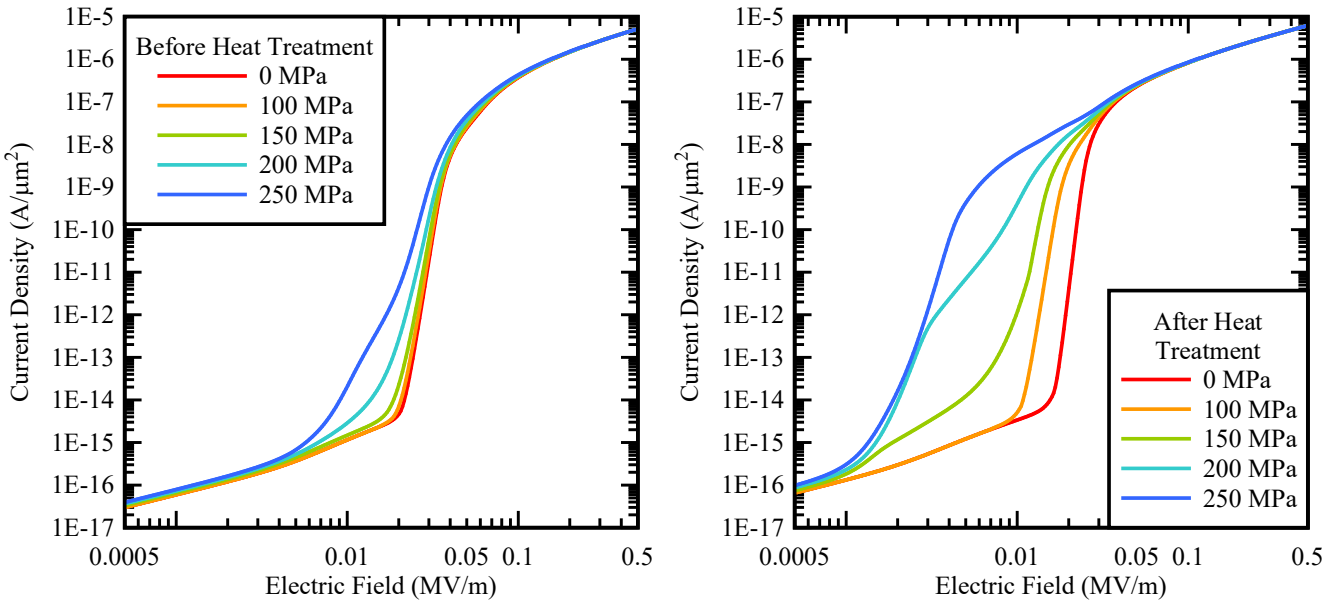

Figure 6.4.3.: IV-characteristics for a SC-PC-SC structure both before (left) and after heat treatment (right) with an average grain size of 10 μm and 25 μm, respectively.

results in a greatly enhanced stress sensitivity, as can be seen from the more pronounced shift in the switching voltage.

The experimental results of Keil et al. also show a strong stress sensitivity after heat treatment of the sample. Furthermore, in both the experiment and the simulation results a "double-knee" is observed in the IV-characteristic, signifying a changing coefficient of non-linearity as the path taken by the current moves with increasing voltage. The non-linearity coefficients corresponding to Figure 6.4.3 are plotted in Figure 6.4.4.

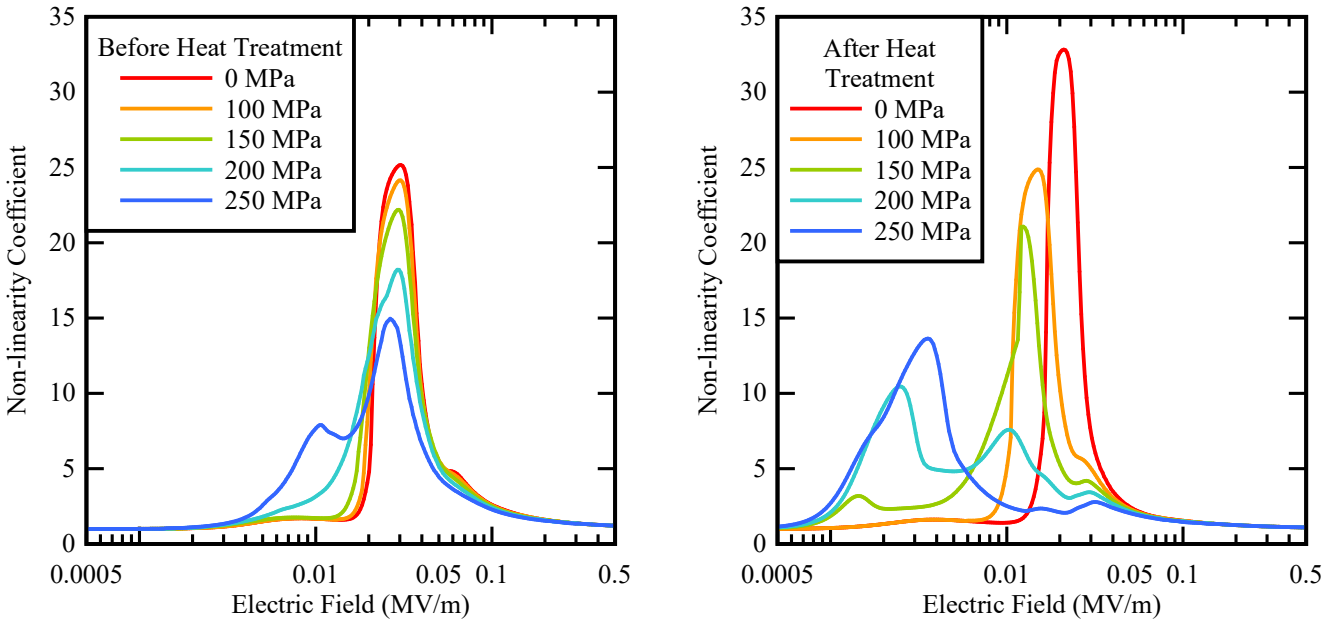

Figure 6.4.4.: Non-linearity coefficients for a SC-PC-SC structure both before (left) and after heat treatment (right) with an average grain size of 10 μm and 25 μm, respectively.

The changing paths taken by the current are visualised in Figure 6.4.5, for the two peaks exhibited by the sample after heat treatment under a uniaxial compressive stress of 200 MPa.

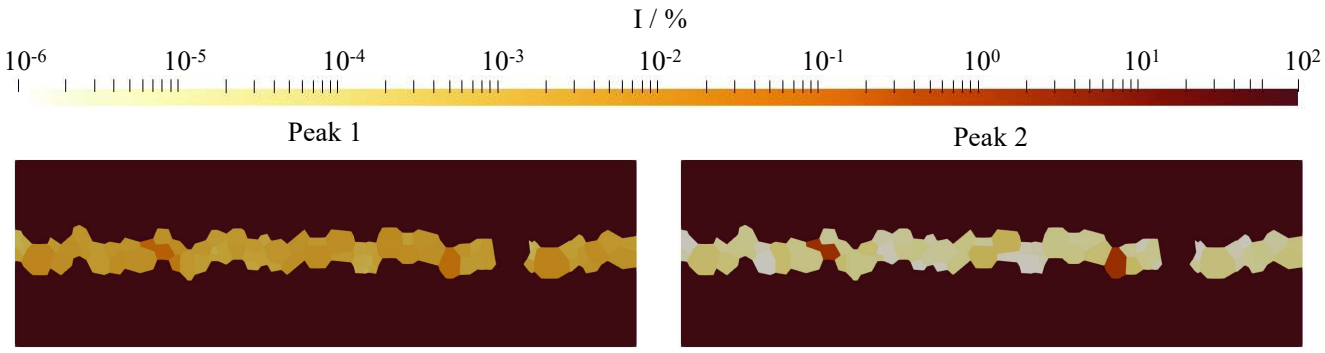

Figure 6.4.5.: Current flow patterns corresponding to the two peaks in the non-linearity coefficient of the sample after heat treatment, for a compressive stress of 200 MPa.

This effect occurs because, depending on the orientation of the grains in the polycrystalline layer and the surface area of their grain boundaries, different pathways become electrically active at different applied voltages. However, a quantitative comparison between experiment and simulation is not possible at this time, due to the lack of detailed knowledge on the grain boundary properties for realistic materials mentioned in Section 6.3.4.

6.5 Thick Film Zinc Oxide

In order to demonstrate the capabilities of the simulation model, we consider a thick film ZnO varistor configuration. The manufacturing and implementation of such varistors for low-voltage insulation applications has been discussed, e.g. in [111, 112]. The purpose of the following is to investigate the influence of bending stress on the electrical varistor characteristic. The model geometry considered is depicted in Figure 6.5.1 (top). It consists of a polycrystalline strip with

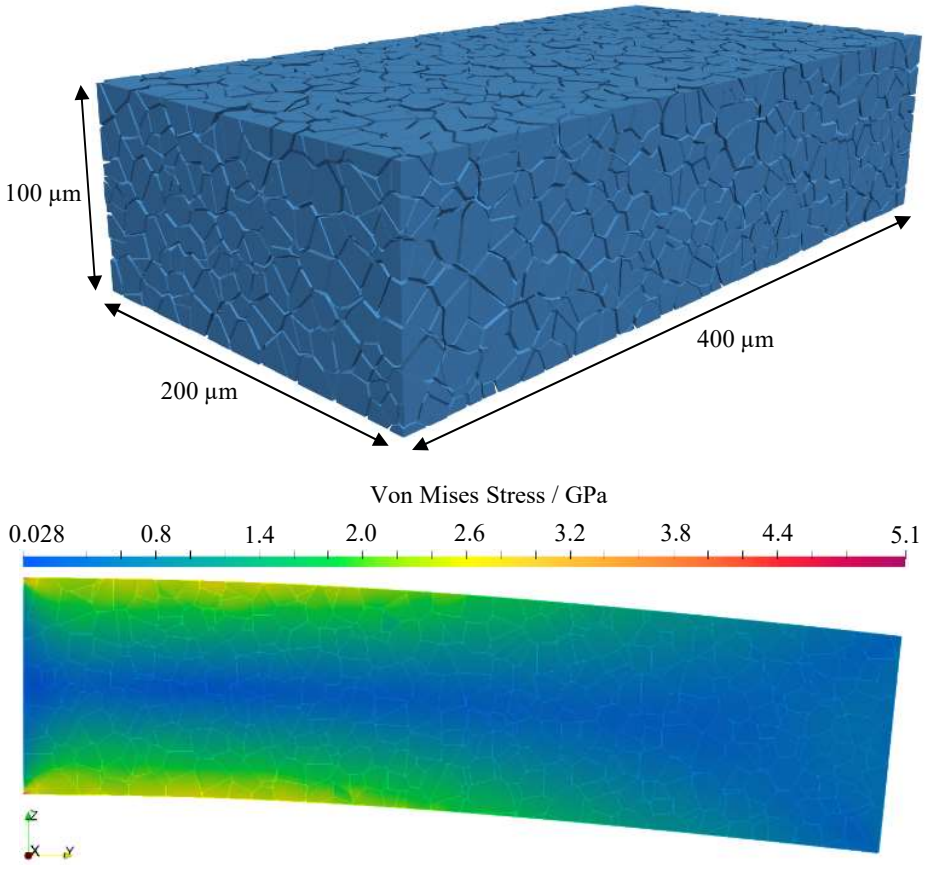

Figure 6.5.1.: Top: Thick film varistor of dimensions 200×400×100 μm^3 and with an average grain size of ≈10 μm. Bottom: Stress distribution after application of 250 MPa of shear force to the right end of the film. Shown is the deformation and the Von Mises stress distribution.

dimensions given in the figure and with grain boundary properties as in Table 4.1.1. The strip is fixed at one end and a downward shear force is applied at the other. The resulting stress distribution is shown in Figure 6.5.1 (bottom).

Figure 6.5.2 (top) illustrates the effect of mechanical stress on the current distribution within the film varistor. When no force is applied, the current paths are spread more or less evenly within the sample. However, when bending is applied, the current paths are localized in the area of highest stress concentration. This results in a current concentration that has a predictable location, namely, close to the base of the strip. The corresponding stress-dependent electrical characteristics of the varistor are shown in Figure 6.5.2 (bottom). As expected, the effect of

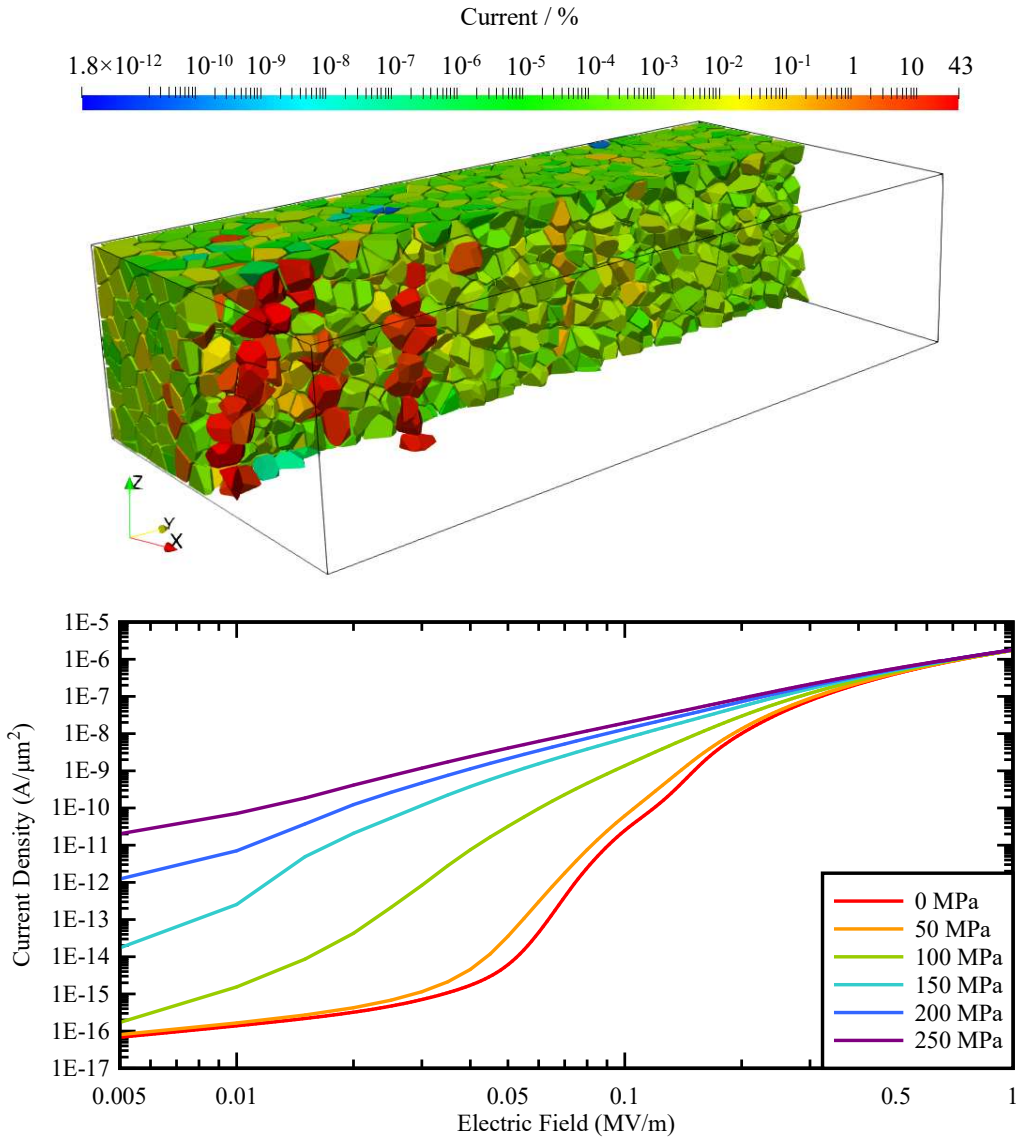

Figure 6.5.2.: Top: Cross section of the thick film varistor showing the current localization for an applied shear stress of 50 MPa and a voltage of 6.5 V. Bottom: The corresponding IV-characteristic.

such bending stress is essentially the same as in the uniaxial case. It results in a lower switching voltage and in a loss of varistor non-linearity with increasing applied stress. This behaviour is irrespective of the presence of compressive as well as tensile stress within the varistor, since both of these stress types may enhance grain boundary conductivity, depending on the crystalline orientation of the individual grains.

6.6 Modelling of 4-Point Measurements

In order to experimentally measure the local electrical properties across a single grain boundary, a characterisation method capable of establishing electrical contact on the micrometer scale is necessary. This can be achieved using a microprobe equipped with four contact needles and the 4-point sensing method [113]. This method is designed to prevent contact between the sample and the electrode from influencing electrical measurements. This works by first applying a current across two electrodes, and then with a second pair measuring the voltage drop across the sample (see Figure 6.6.1). The resistance of the voltmeter is very high, and its current can thus be neglected, resulting in a measurement that is very close to the voltage across the sample alone.

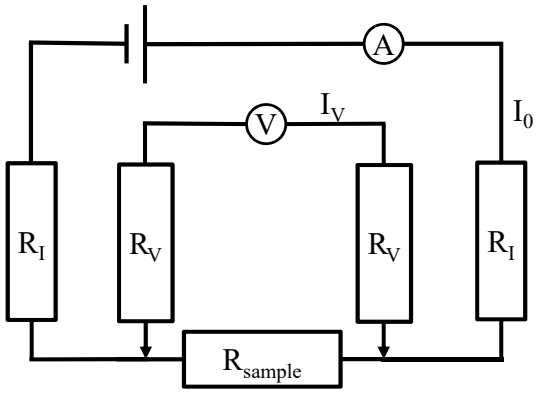

Figure 6.6.1.: Equivalent circuit diagram for the 4-point sensing method. R_I is the resistance of the contacts attached to the current source, R_V is the resistance of contacts attached to the voltmeter. R_{sample} is the resistance of the sample, I_V is the current through the voltmeter and I_0 is the current from the source. [113]

Since the voltage across a grain boundary in the equivalent network model can be calculated directly, this is an easy test case to reproduce and can be compared to data from bicrystal simulations, in order to assess whether the results are truly representative of a single grain boundary. Furthermore, the resulting current flow visualisations can provide additional insight into the behaviour of current flow within varistor microstructures.

Figure 6.6.2 shows the sample geometry used to reproduce the 4-point sensing method. Two grains near the middle of the top surface of the varistor are chosen as contact points for the electrodes and assigned orientations that are close to head-to-head, relative to their mutual grain boundary. A uniaxial compressive stress is then applied to the sample in the x-direction.

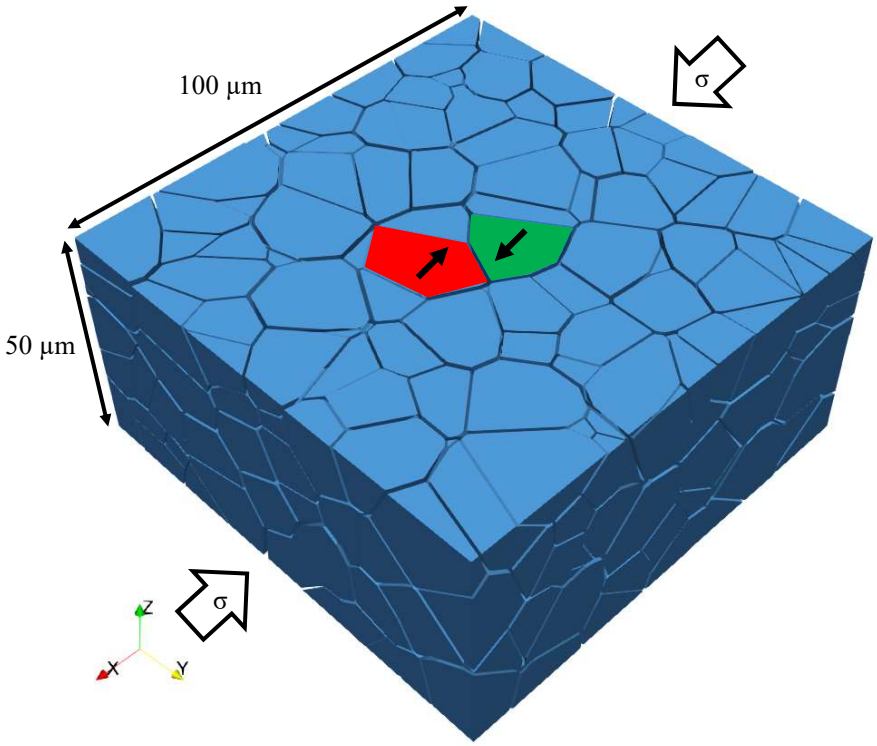

Figure 6.6.2.: 500 grain varistor block of dimensions 100×100×50 μm and with an average grain size of ≈10 μm. The grain surfaces chosen for contacting the electrodes are coloured in red and green, and marked with arrows indicating the orientations of their c-axes.

The resulting current flow patterns are shown in Figure 6.6.3 for cases with and without an applied stress, and at voltages in the leakage, breakdown and upturn regions. The corresponding IV-characteristics are plotted in Figure 6.6.4.

Each region of the characteristic shows a distinct current flow pattern. In the leakage region, current flows primarily through the two contacted grains, but also through neighbouring grains, with a reduced current concentration the further the grain is from the electrodes. In the breakdown region, the conductivity of the grain boundary between the two electrodes increases dramatically and current flows almost exclusively through this boundary. Finally, as the applied voltage increases past the breakdown and into the upturn region, the local working points of grain boundaries further from the electrode pair also begin to enter the breakdown region associated with their individual IV-characteristic. The conductivity of these boundaries increases

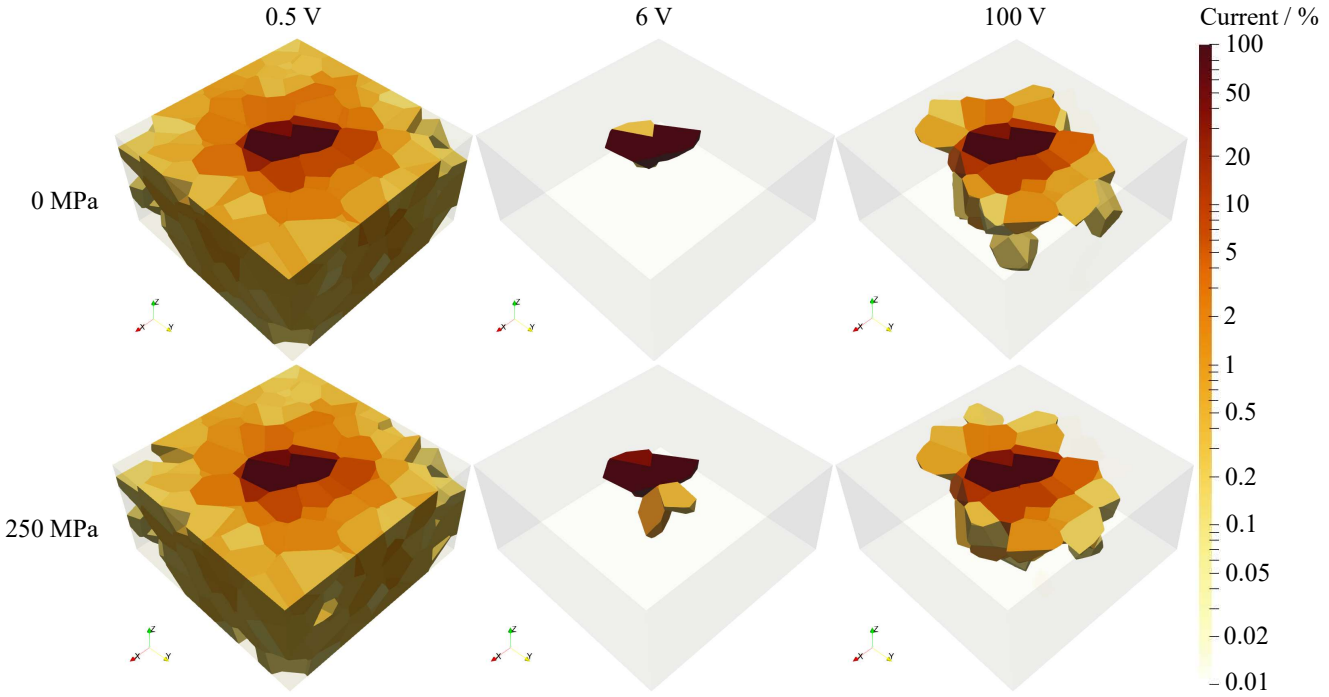

Figure 6.6.3.: Current concentration for varying applied voltages, with and without applied stress, in the varistor structure shown in Figure 6.6.2. The current in each grain is given relative to the total current flowing through the sample. Only grains carrying ≥0.1% of the total current are shown.

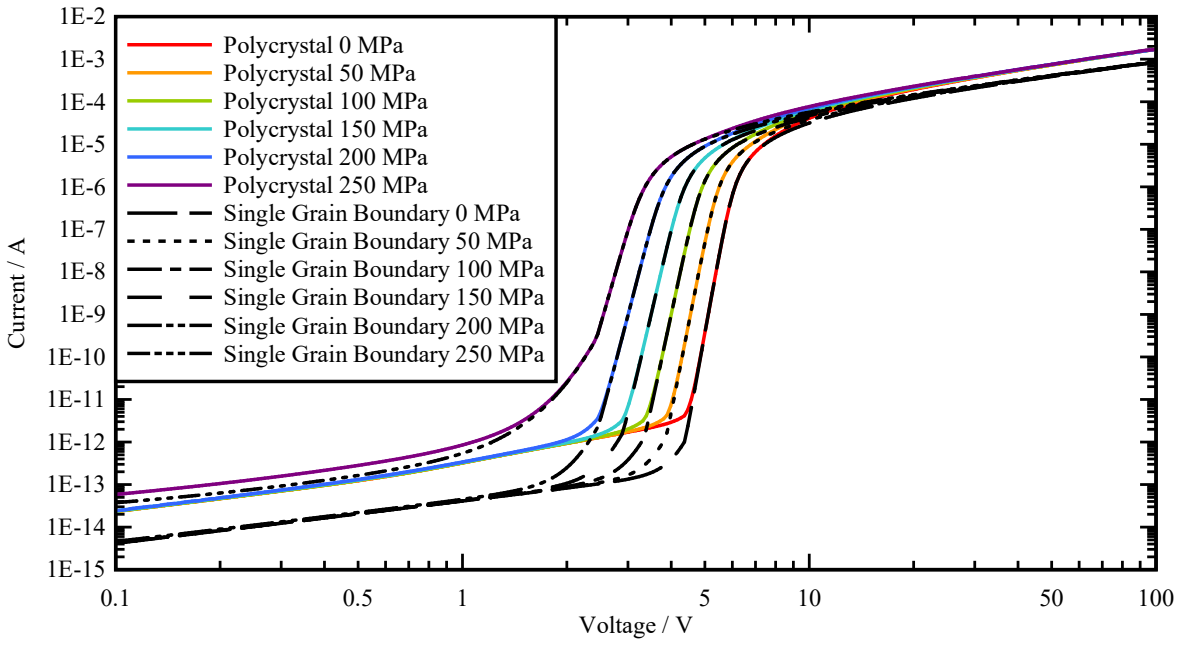

Figure 6.6.4.: IV-characteristics for the full varistor structure shown in Figure 6.6.2 and for the single grain boundary between the pair of highlighted grains.

and thus the number of current-bearing grains also increases, forming a roughly hemispherical section of current-bearing grains, which grows as grain boundaries further and further from the electrode pair enter breakdown.

The effect of applied stress is much the same as that shown in Section 6.3, in that the switching voltage decreases, as shown in Figure 6.6.4. Naturally, this also impacts the current flow pattern, as each of the changes described above occurs at a lower applied voltage. For example, the current concentration seen at 6 V with an applied stress of 250 MPa is reduced compared to that seen at 6 V with no applied stress, because, at this point, the stressed sample is already beginning to push into the upturn region of its characteristic and its maximum current concentration occurs around 5 V.

When current is only allowed to flow through the grain boundary connecting the two grains with contact to the electrodes, the true IV-characteristic for this grain boundary is obtained. This is represented by the black IV-characteristic curves in Figure 6.6.4. Comparing this set of results to the coloured curves, which represent the measurement obtained from a 4-point sensing experiment, highlights some notable differences. Firstly, since the current in the polycrystalline case is free to seek more conductive grain boundaries, the current in the leakage and upturn regions of the curves is higher. Furthermore, due to the more distributed current flow, the impact of applied stress on the non-linearity of the characteristic is greater in the polycrystalline case, as can be seen from the softer gradient as the IV-characteristic enters the breakdown region. Nevertheless, the switching voltage does not significantly change between the two data sets. These differences between a true single boundary measurement, and a measurement carried out using the 4-point sensing method, should be taken into consideration when performing such measurements.

7 Thermal Stress

7.1 Effect of Residual Thermal Stress

The crystallographic anisotropy in the thermal expansion of ZnO grains commonly results in internal mechanical stress in ZnO varistors. This build up of residual internal stress arises between grains when polycrystalline samples are cooled from their fabrication temperature, thus causing the individual grains to shrink. Just as for an applied stress, this induces a net electric dipole moment that modifies the Schottky barriers at the grain boundaries, and thus the IV-characteristic. Due to the piezoelectric nature of ZnO, this stress can have a detrimental impact on the non-linearity of a varistor.

Verghese et al. were able to measure the residual strain in polycrystalline ZnO samples using Raman piezospectroscopy [18]. The permissible energies for phonons and electrons in a crystal lattice can be modified by mechanical strain, which results in a shift in the characteristic fluorescent spectral peaks of the material or in its Raman scattering. This allows for an experimental quantification of the mechanical stress state in piezoelectric materials. Based on these results, Verghese calculated the average residual stress and assumed a Gaussian distribution of stress throughout the material.

Based on this stress distribution, Verghese created a stochastic model for the barrier height distribution, based on equations (3.1.11) and (3.3.7), although this earlier model did not include the self-consistent solution with (3.2.2), as described in Section 4.1. This model also assumes a Gaussian distribution of barrier heights within the polycrystal, and this was verified by a Monte Carlo simulation of the barrier height, which showed a good agreement with the assumed distribution. The resulting effective medium calculations [114] revealed both a decrease in the non-linearity coefficient and an increase in the leakage current of the sample.

In the following, we present a comparison to the work of Verghese et al. by calculating the residual thermal stress distribution numerically using FEM. This voids the need for an assumed stress distribution, and instead allows us to calculate the potential barrier at each grain boundary directly, using the method described in Section 6.1.

7.2 The Bicrystalline Case

In the following, we consider the case of the residual stress that arises when cooling a bicrystal from a stress-free state at 1500 K to 300 K. The boundary conditions are left open to displacement, and the grain's c-axes are oriented at 90° to one another, as shown in Figure 7.2.1.

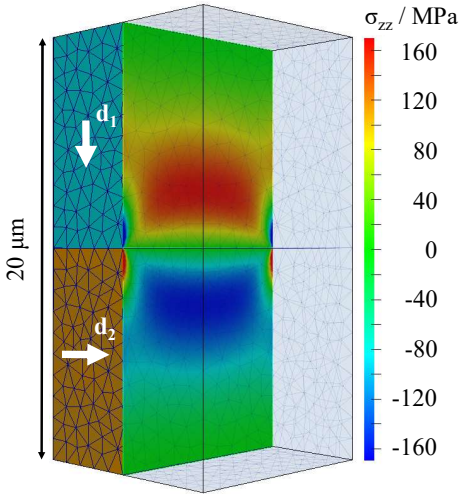

Figure 7.2.1.: Distribution of residual stress after thermal treatment. Also shown are the c-axis orientations and the style of FEM mesh used in the calculations.

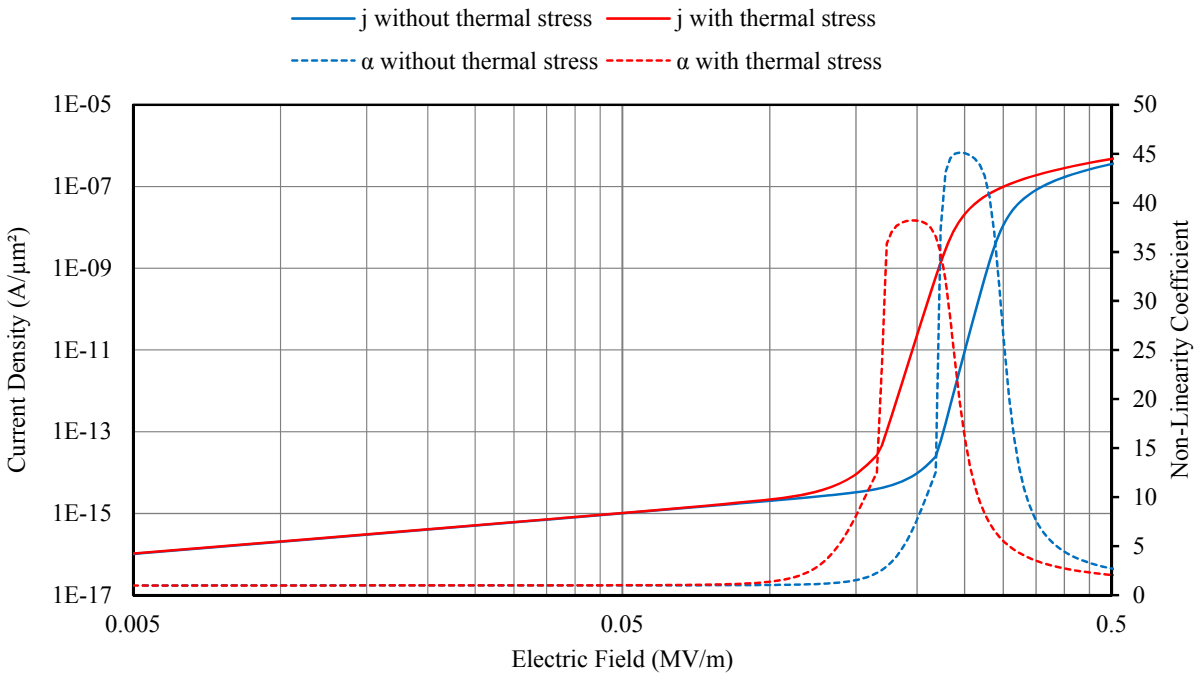

Figure 7.2.2.: IV-characteristics and non-linearity coefficient of the bicrystal.

Figure 7.2.2 depicts the non-linearity coefficients of the bicrystal for the cases with and without residual stress, respectively. Again, the presence of mechanical stress leads to the loss of varistor non-linearity and to a shift of the switching voltage to lower values. This effect is comparable to that of a 90° orientation bicrystal when an external stress is of 100 MPa is applied (cf. Figure 3.1.1). This is reflected in the jump in stress from one grain to the other, as shown in Figure 7.2.1. Thus, in this case, the piezoelectric effect is not only due to the different grain orientations, but also to a jump in the mechanical stress across the boundary of the order of 100 MPa.

7.3 The Polycrystalline Case

In Figure 7.3.1, the computed stress distribution within a varistor sample of dimensions 200×300 μm, and with an average grain size of 10 μm (consisting in a total of 600 grains), is shown. The material was cooled from 1200 K down to 300 K, while the boundary conditions of the simulation were left open to displacement. The resulting stress within the polycrystal is much higher than in the case of the bicrystal, since the internal grains cannot freely contract. Furthermore, due to the significant anisotropy of both thermal expansion and elastic modulus, which arises from the shape of the ZnO unit cell, the mechanical stress in each grain is different.

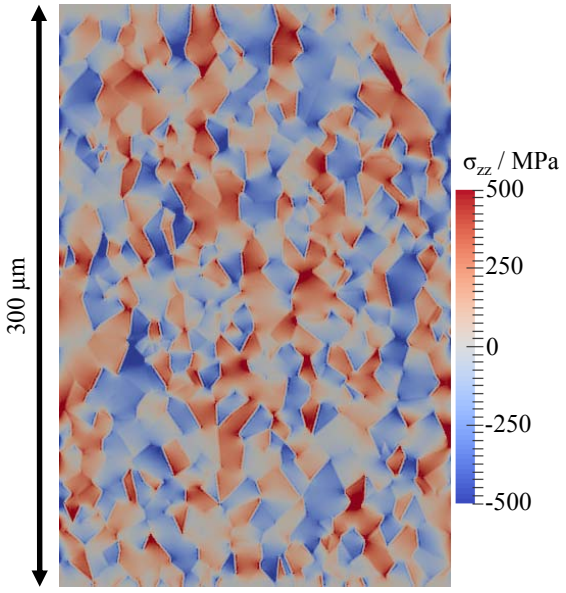

Figure 7.3.1.: Mechanical stress distribution (σ_{zz}) for a 2D polycrystal of size 200×300 μm^2 and average grain size of 10 μm, after cooling from 1500 K to 300 K.

An assessment of the distribution of Von Mises stresses throughout the polycrystal is given in Figure 7.3.2. As seen in the histogram representation, the resulting mean and standard

deviation of the Von Mises stress in the individual grains are very similar to those measured by Verghese et al. using Raman spectroscopy, featuring a distribution peak near 250 MPa [18].

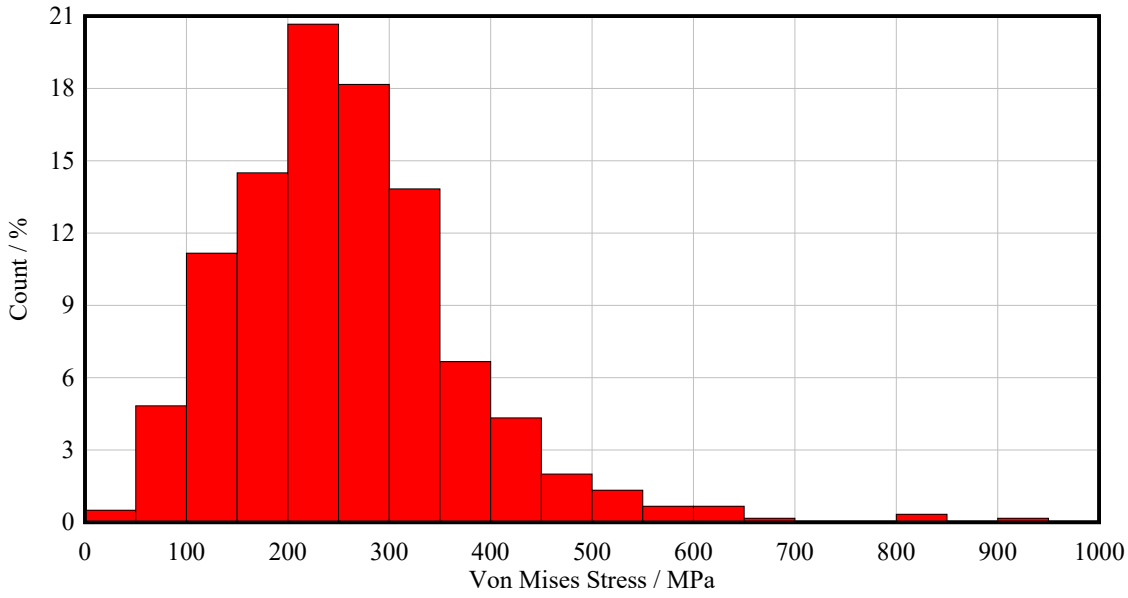

Figure 7.3.2.: Thermal stress distribution in the polycrystal shown in Figure 7.3.1 after cooling from 1200 K to 300 K. Mean stress = 258 MPa. Standard deviation = 115 MPa.

The current flow pattern within the sample resulting from the numerical solution of the circuit equations for an applied external voltage of 15 V is shown in Figure 7.3.3.

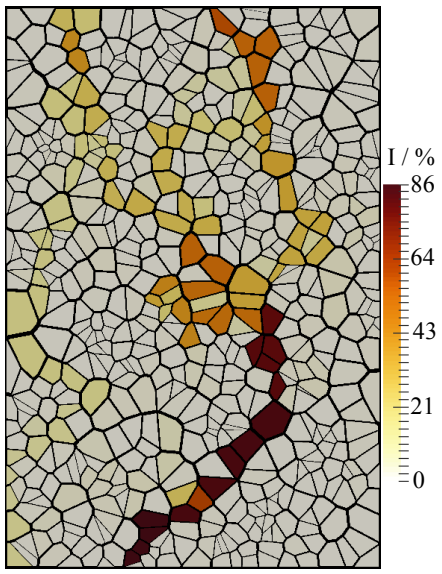

Figure 7.3.3.: Electrical current pattern for the samples shown in Figure 7.3.1 in the sample for an applied voltage of 15 V (effective electric field strength of 0.05 MV/m). The current in each grain is given relative to the total current through the sample.

The current flow patterns resulting from the solution of the circuit equations for the larger polycrystalline structure introduced in Figure 7.3.1 are shown in Figure 7.3.4. The results are compared for different applied voltages and for the cases with and without residual thermal stress. In both cases, the well known current concentration effect in the non-linear varistor regime [22] is observed. In addition, the simulations show the loss of non-linearity induced by the presence of residual stress. This is indicated by the more uniform current distribution consisting of several low density paths in the later case.

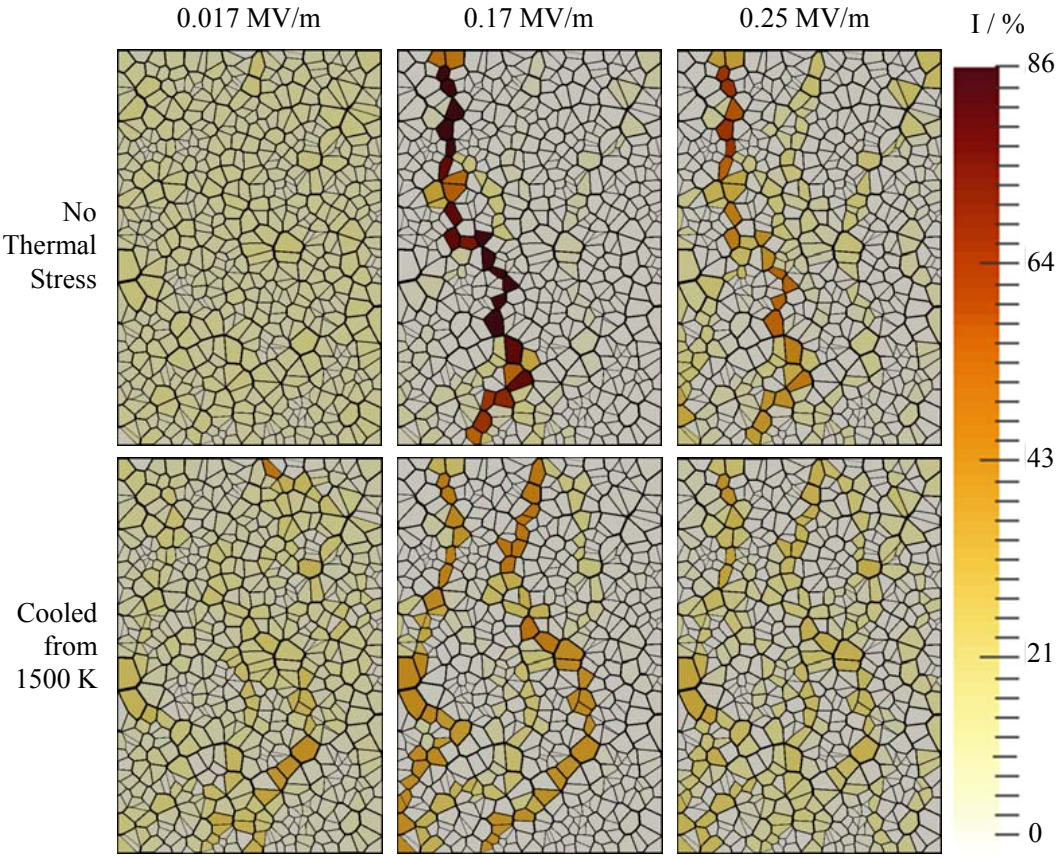

Figure 7.3.4.: Electrical current patterns obtained for the polycrystalline structure considered in Figure 7.3.1 with and without the effect of thermal stress. The current in each grain is given relative to the total current flowing through the sample.

A more quantitative analysis of the effect of thermal stress is provided by the effective IV-curves of the sample as shown in Figure 7.3.5. The behaviour of these curves is similar to that of the head-to-head bicrystalline case. An increasing residual stress results in a reduction in the switching voltage and in the decrease of the effective non-linearity coefficient of the sample. Although grain boundaries with compressive configurations close to tail-to-tail and tensile configurations close to head-to-head will exist within the polycrystalline sample, almost no current flows through these low-conductivity boundaries. The current paths concentrate

along those grain boundaries exhibiting orientations close to head-to-head and tail-to-tail, under compressive and tensile stress respectively. This is because these grain boundaries experience an increased electrical conductivity due to the presence of residual thermal stresses. The mechanical modulation of electrical conductivity in polycrystalline materials is thus determined by the reciprocal grain orientations within the material that are responsible for the piezoelectric coupling of grain boundary conductivity.

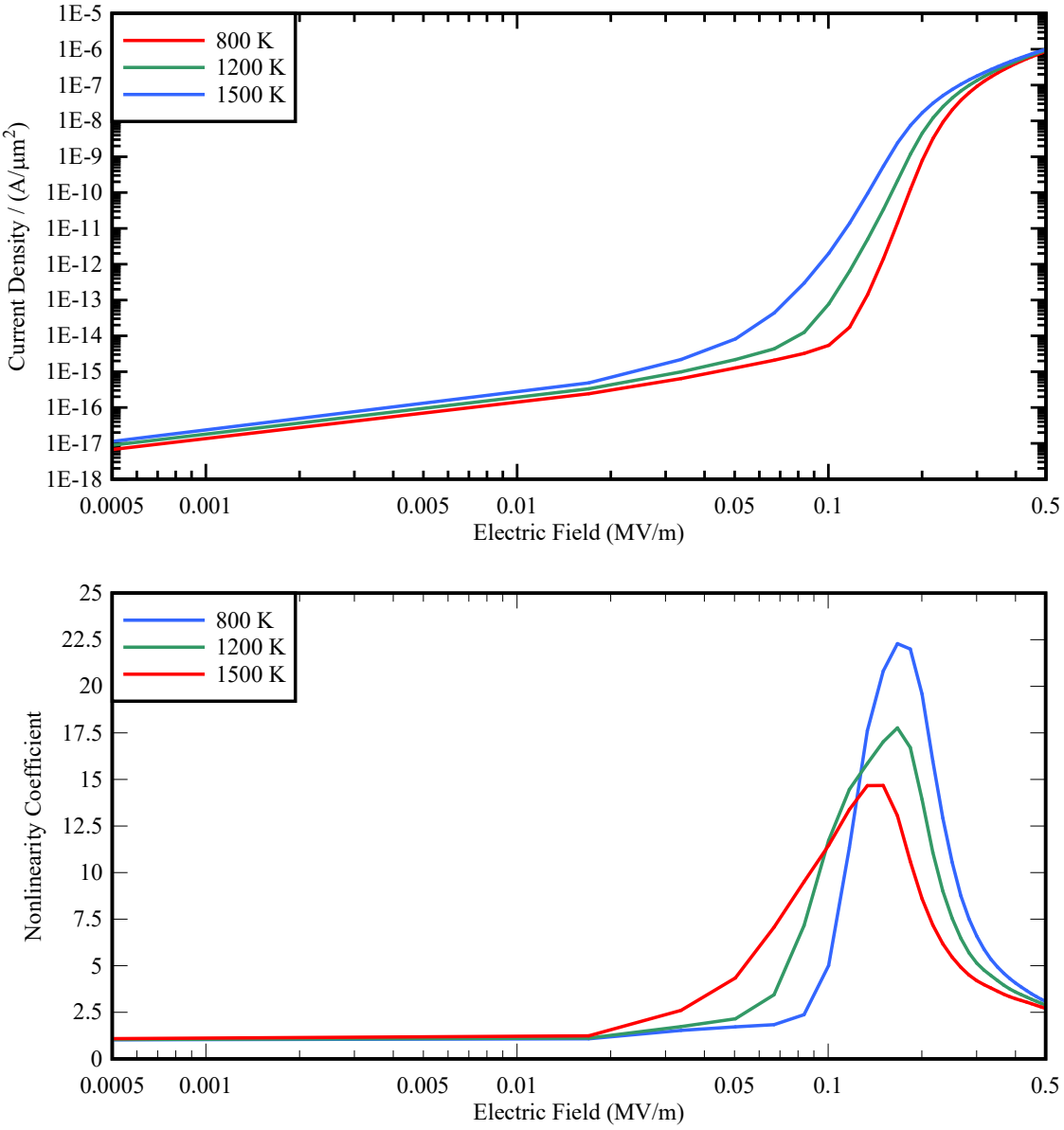

Figure 7.3.5.: Electrical characteristics (top) and non-linearity coefficient (bottom) for the 2D polycrystal shown in Figure 7.3.1.

Expanding the same system to 3D shows much the same relationship as for an applied stress, as shown in Figure 7.3.6. The switching voltage falls with increasing stress levels, resulting in a lower effective non-linearity. This effect is exacerbated in three dimensions, due to the larger number of possible pathways available for current flow.

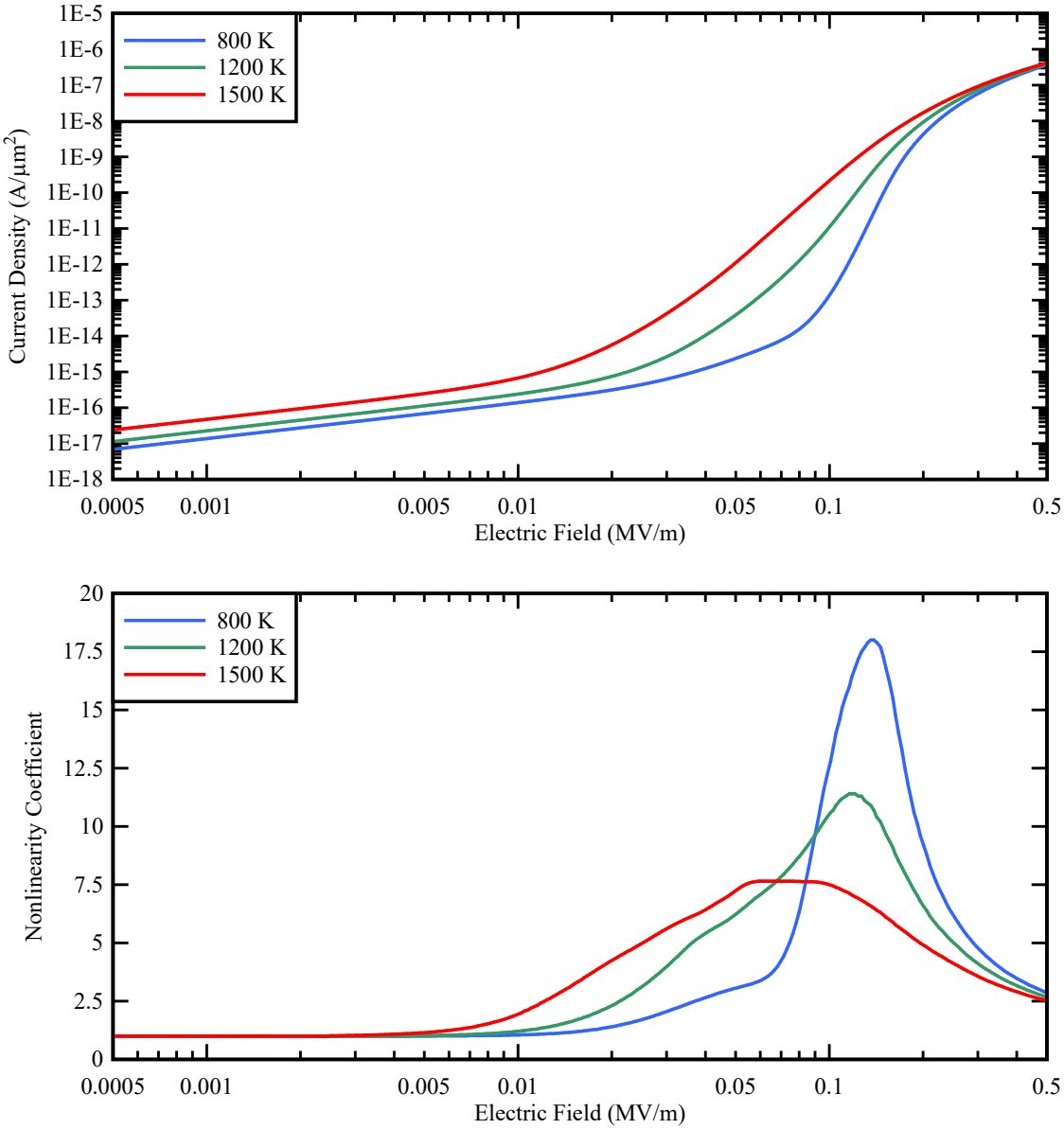

Figure 7.3.6.: Electrical characteristics (top) and non-linearity coefficient (bottom) resulting from residual thermal stress after cooling from different temperatures for a 3D polycrystal of size 200×200×300 μm^3 and with an average grain size of 10 μm.

8 The Inverse Piezoelectric Effect

8.1 Modelling the Inverse Piezoelectric Effect

When a voltage is applied to a varistor, the electric field inside the material induces a mechanical response in the form of a strain via the inverse piezoelectric effect. This, in turn, generates additional piezoelectric strain charges at the grain boundary, thus modifying the polarisation. The effect of these additional charges on the IV-characteristic will be examined in this section.

In order to account for the inverse piezoelectric effect, an additional term must be added to the relationship between stress and strain, as performed by Xu et al. [115]. In one dimension, this relationship takes the form

$$\sigma = CS - eE\,, \tag{8.1.1}$$

where σ is the stress, C is the Young's modulus, S is the strain, e is the piezoelectric strain constant and E is the electric field. In comparison to the model so far, the term eE is new and accounts for the strain inducing effect of the electric field. From this, the polarisation,

$$P = eS = e\left(\frac{\sigma + eE}{C}\right) = e\frac{\sigma}{C} + \frac{e^2E}{C}\,, \tag{8.1.2}$$

can be calculated [17]. In the classical model proposed by Verghese [18], only the direct contribution $d\sigma = \frac{e}{C}\sigma$ is accounted for, while the inverse part $\frac{e^2E}{C}$ is neglected. Here, the electric field dependent term is added to Q_P (c.f. Equation 3.3.7), resulting in

$$Q_P' = Q_P + \frac{e^2(E_l - E_r)}{C}\,, \tag{8.1.3}$$

where E_l and E_r are the electric fields from the left and right hand sides of the grain boundary, respectively. Close to the grain boundary, the electric field is given by [58]

$$E(x) = \begin{cases} \frac{q\tilde{N}_\nu}{\varepsilon_r\varepsilon_0}\left(x - \frac{\tilde{Q}_i}{2q\tilde{N}_\nu} + \frac{\varepsilon_r\varepsilon_0 V}{\tilde{Q}_i}\right) & -x_l \le x \le 0 \\ \frac{q\tilde{N}_\nu}{\varepsilon_r\varepsilon_0}\left(x + \frac{\tilde{Q}_i}{2q\tilde{N}_\nu} + \frac{\varepsilon_r\varepsilon_0 V}{\tilde{Q}_i}\right) & 0 \le x \le x_r \end{cases}\,, \tag{8.1.4}$$

where q is the positive unit charge, $\tilde{N}$ is the space charges in the depletion layer, ε_r is the relative permittivity of the material, $\tilde{Q}_i = Q_i + Q_P'$, and the x-axis is perpendicular to the grain

boundary with its origin at the grain boundary. Furthermore, $q\tilde{N}_v = qN_v + \rho_P$, where the term ρ_P defines an additional space charge in the depletion layer, which has been induced by the inverse piezoelectric effect.

Since the derivation of (8.1.4) assumes a linear field in the depletion layer, ρ_p and $\tilde{N}_v$ are constant in that region. This means that $\nabla \cdot E = \frac{q\tilde{N}_v}{\varepsilon_r \varepsilon_0}$, and so

$$\rho_P = -\frac{e^2 q\tilde{N}_v}{C\varepsilon_r\varepsilon_0}, \tag{8.1.5}$$

which in combination with $q\tilde{N}_v = qN_v + \rho_P$ produces the relationship

$$\tilde{N}_v = (1-f)N_v, \quad f = \frac{e^2}{\varepsilon_r\varepsilon_0 C + e^2}, \tag{8.1.6}$$

where f is a dimensionless factor composed of the piezoelectric strain constant, the dielectric constant and the Young's modulus. Thus, the term $-fN_v$ accounts for the space charge arising from the electric field. Combining (8.1.4) and the following solutions for x_l and x_r,

$$\begin{aligned} x_l &= -\frac{\tilde{Q}_i}{2q\tilde{N}_0} + \frac{\varepsilon_r\varepsilon_0 V}{\tilde{Q}_i} \\ x_r &= -\frac{\tilde{Q}_i}{2q\tilde{N}_0} - \frac{\varepsilon_r\varepsilon_0 V}{\tilde{Q}_i} \end{aligned}. \tag{8.1.7}$$

gives the electric field at the grain boundary,

$$\begin{aligned} E_l &= \frac{q\tilde{N}_v}{\varepsilon_r\varepsilon_0}\left(-\frac{\tilde{Q}_i}{2q\tilde{N}_v} + \frac{\varepsilon_r\varepsilon_0 V}{\tilde{Q}_i}\right) \\ E_r &= \frac{q\tilde{N}_v}{\varepsilon_r\varepsilon_0}\left(\frac{\tilde{Q}_i}{2q\tilde{N}_v} + \frac{\varepsilon_r\varepsilon_0 V}{\tilde{Q}_i}\right) \end{aligned}, \tag{8.1.8}$$

which is then inserted into (8.1.3). Together with $\tilde{Q}_i = Q_i + Q'_P$, this results in an expression for $\tilde{Q}_i$ in terms of f,

$$\tilde{Q}_i = (1-f)(Q_i + Q_P). \tag{8.1.9}$$

This reveals the nature of f as a scaling factor that acts upon the total interface charge at the grain boundary. The stronger the inverse piezeoelectric field, the larger f grows, and the more the interface charge is reduced. When this effect is included in the expression for the potential barrier at the grain boundary (3.1.11), it is modified as follows,

$$\phi_B = -\frac{qN_v}{2\varepsilon_r\varepsilon_0}(1-f)\left(-\frac{Q_i+Q_P}{2qN_v} + \frac{\varepsilon_r\varepsilon_0 V}{(1-f)(Q_i+Q_P)}\right)^2. \tag{8.1.10}$$

When $f = 0$, this simplifies to the classical equation presented by Verghese [18].

This factor can be accounted for in the variable resistance, R_b, in the lumped conductivity model for a each grain boundary. For a one-dimensional bicrystal, all components of f are scalar. Assuming a bicrystal of head-to-head orientation and that, as in the work of Zhou et al. [17], only the zzz-component of the piezoelectric strain tensor and the zzzz-component of the Young's modulus contribute to f, this results in a value of 0.096, which equates to a 9.6% reduction of the interface charge. The IV-characteristic of such a bicrystal is shown below in Figure 8.1.1.

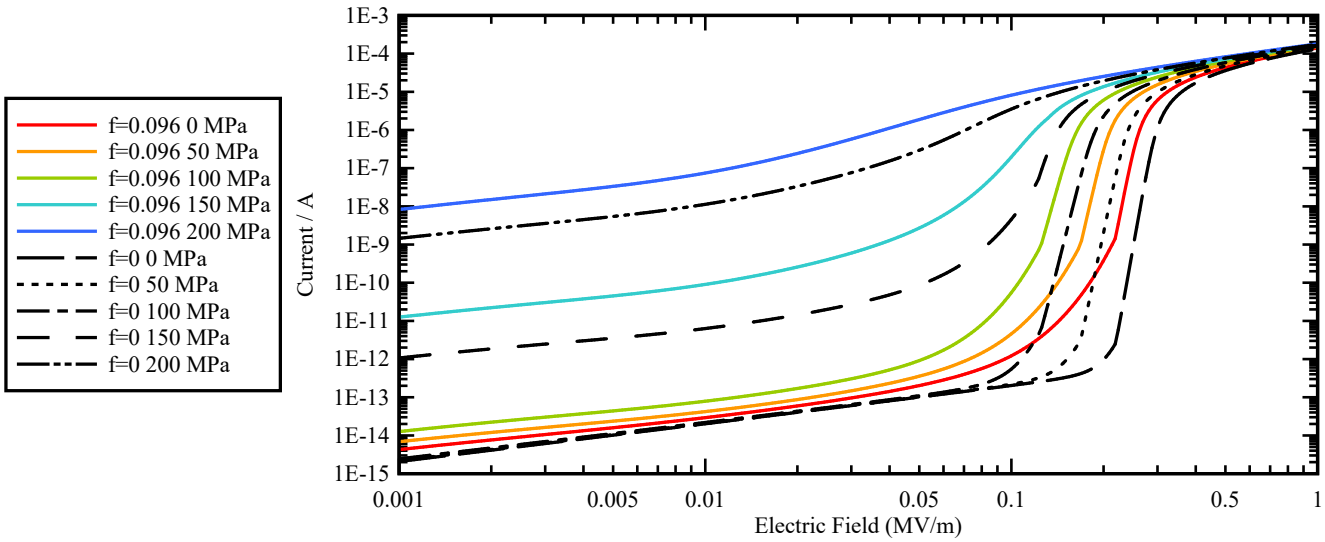

Figure 8.1.1.: IV-characteristics for a 1D head-to-head bicrystal with and without the inverse piezoelectric effect.

The influence of the reduced interface charge on the one dimensional problem is clear. The switching voltage and non-linearity both fall noticeably, similarly to the effect of a polarisation induced by mechanical stress. This is to be expected, as, in the head-to-head case, the piezoelectric effect also acts to reduce the interface charge and thus the barrier height.

8.2 The Influence of the Inverse Piezoelectric Effect in 3D

Blatter's model for charge transport across a grain boundary, as described in Sections 3.1 and 3.2, is a 1D model, and the derivation of the factor f in Section 8.1 is an expansion upon this model. As shown in (8.1.6), f depends on both C and e, which, in 1D, are scalar values. However, in 3D, these material properties are described by tensors that change their value depending on the crystal orientation of each grain. These tensors are given as matrices in Voigt notation in (3.3.4) and (6.2.2).

This section aims to use the above model to gain insight into the influence of the inverse piezoelectric effect in 3D. To that end, the 1D model for charge carrier transport across grain boundaries, as employed in Chapters 5-7, is retained, with the addition of the inverse piezoelectric scaling factor, f, as given in (8.1.6) and (8.1.10). In doing so, we assume that, for the case of charge transport across any one boundary in the electrical network, C and e can be reduced to a single scalar value that acts along the grain boundary normal, thus allowing for the calculation of f.

For 3D polycrystalline varistor material, the matrices representing the tensors of C and e are transformed to match the coordinate system of each individual grain by multiplying them with the appropriate transformation matrices [116]. For brevity, the transformation matrices are given in Appendix A.6. The components of the transformed matrix that act along the grain boundary normal are then extracted, to give a scalar value for f in the direction of the grain boundary. Thus, all values in (8.1.10) are scalars and the potential barrer can be calculated including the inverse piezoelectric effect.

In Figure 8.2.1, a head-to-head bicrystal is considered. In 3D, the zxx and zyy components of the piezoelectric strain tensor also contribute to the value of e in the z-direction, thereby reducing its final value and resulting in a smaller f. This reveals the relatively minor overall impact of the inverse piezoelectric effect in 3D simulations - in this case the interface charge is reduced by only 0.4%.

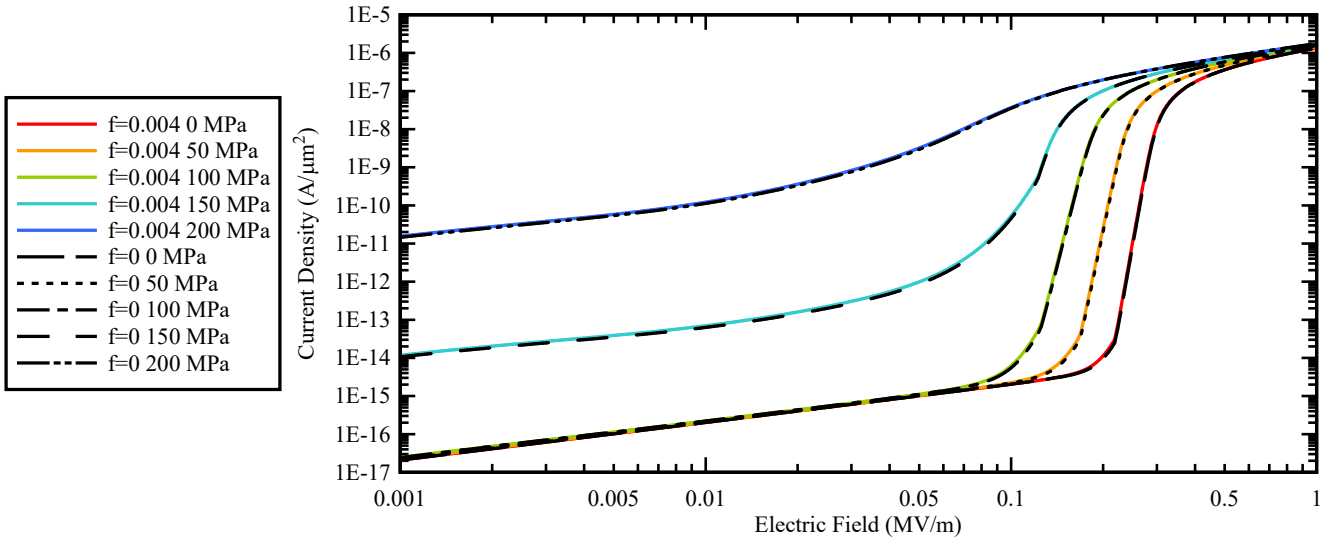

Figure 8.2.1.: IV-characteristics for a 3D head-to-head bicrystal of dimensions 10×10×20 μm^3, with and without the inverse piezoelectric effect.

Figure 8.2.2 shows the result of applying the inverse piezoelectric effect to a polycrystalline case. The value of f is independent of the applied stress, but specific to the relative orientations of the grains in the varistor. For the microstructure used here, the average value of f is 0.007, corresponding to a reduction in interface charge of 0.7%. This is larger than the value obtained for a 3D bicrystal, due to the variety of orientations between grain pairs that is inherent to the polycrystalline structure. The Young's modulus of the ZnO unit cell is maximal in the z-direction and a lower Young's modulus leads to a slightly larger value for f. Nevertheless, the difference is minor and thus the overall value of f remains relatively small.

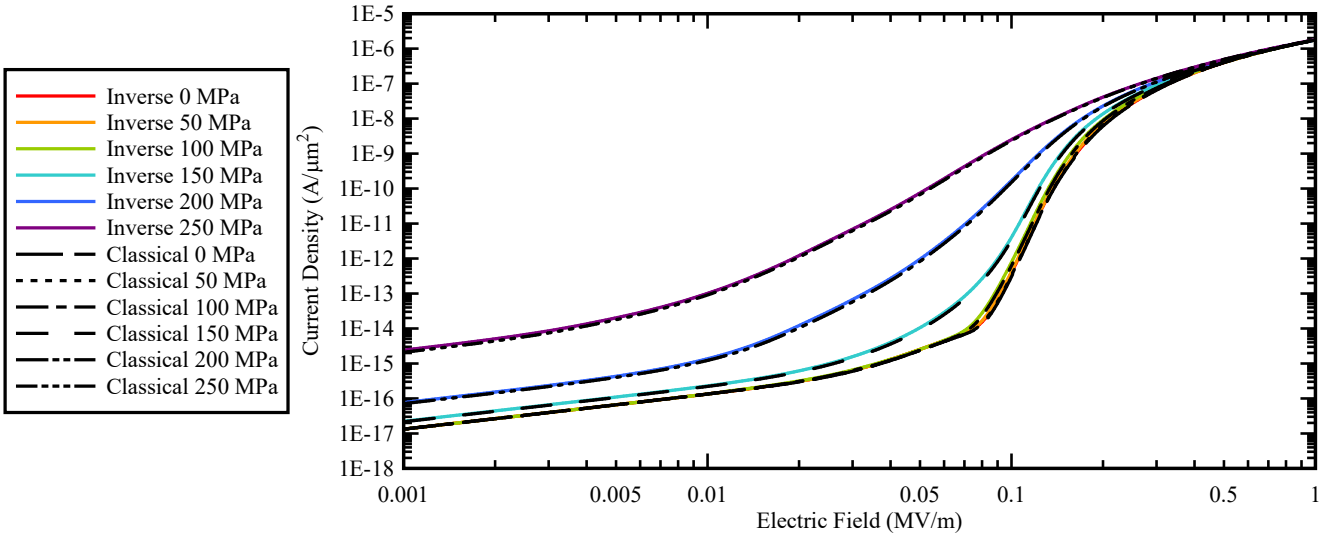

Figure 8.2.2.: IV-characteristics for a varistor of dimensions $100\times100\times150\ \mu m^3$, with and without the inverse piezoelectric effect.

9 Conclusion and Outlook

9.1 Conclusion

A model for calculating the stress-dependent electrical characteristics of ZnO varistors is developed. The model is based on an equivalent electrical network description of the varistor microstructure. The piezoelectric effect at the grain boundaries is taken into account by incorporating a self-consistent solution for the grain boundary potential and the piezoelectrically induced grain boundary charge. This modelling approach is applied for polycrystalline varistor structures consisting of a large number of grains with arbitrary crystallographic orientations and for arbitrary stress distributions, in 2D as well as in 3D geometry.

The simulations reveal the strong stress sensitivity of the varistor characteristics and provide insight into the current flow behaviour within the material, in the presence of mechanical stress. On the macroscopic scale, the effect of mechanical stress shifts the IV-characteristic to a lower switching voltage. Furthermore, the effective non-linearity of the material is reduced. These results, as well as the computed gauge factors for a typical varistor sample, are consistent with recent experimental findings for industrial ZnO varistors. The investigation of microstructurally inhomogeneous varistors and the simulation of a bent thick film varistor under shear stress demonstrate the capability of the model to cope with complicated material configurations. The model was also applied to demonstrate the differences between measurements made using the 4-point sensing method, and the true IV-characteristic of a single grain boundary. In addition to this, the model was applied to the case of residual stresses arising within microstructures due to the thermal expansion anisotropy of the crystal. Polycrystalline structures with different residual thermal stresses resulting from sintering at different temperatures were analysed. Furthermore, the model was adapted to account for the inverse piezoelectric effect. It was able to demonstrate that this effect's influence on the overall IV-characteristic was vanishingly small in the case of 3D polycrystalline varistor samples.

Overall, this new model offers a qualitative representation of the observed phenomenon and is highly flexible in terms of the geometries and mechanical stress states to which it can be applied.

9.2 Outlook

Future work could make use of, or extend upon, the framework that was established in this thesis in a number of areas.

A quantitative verification of the model's capabilities would require values for the parameters shown in Table 4.1.1 for a specific ZnO varistor composition, and stress-dependent electrical measurement data using varistor material of the same kind. Such measurements could be obtained experimentally using off-axis electron holography [117]. Alternatively, the values could be derived from the density of states, which could be determined numerically, using density functional theory [46].

An extensive statistical analysis of the effect of the stochastic properties of polycrystalline microstructures on the IV-characteristics produced by this model would also serve to further cement its validity. Variations in the geometry of the varistor microstructure, as well as the distributions of grain sizes, grain orientations, and microstructural inhomogeneities, all play a role in determining the effective IV-characteristic of the varistor as whole. While an analysis involving large numbers of simulations for comparable varistor samples goes beyond the scope of this work, a future investigation using a large dataset would serve well to underline the model's utility.

Finally, this model has concerned itself with the electromechanical coupling of mechanical stress and grain boundary barrier height in ZnO varistors via the piezotronic effect. However, any current flowing through such a varistor is accompanied by an increase in the temperature of the material, which in turn has an impact on the conductivity of the varistor. In the breakdown region, when current concentration occurs, this effect is particularly noticeable, due to the high current densities that occur locally along the path of current flow. Future work could consider this effect (perhaps by using a lumped thermal circuit model [118]) and, via back-coupling, model the effect of thermal runaway, described in Section 2.3.

A Appendices

A.1 Code for the Self-Consistent Solution of the Potential Barrier

The following script was written in Wolfram Mathematica 11.2. It performs the self-consistent solution of of the coupled equations (3.1.11)-(3.2.2) and produces the coefficients for the fitting function shown in (6.1.1), for tabulated values of Q_P. Note that this script requires the `RootSearch.m` package [119].

```
ClearAll;
Import["C:\\FilePath\\RootSearch.m"]
q0 = 1.60217662*10^-19; (* Elementary Unit Charge / C *)
kT = (1.3806488*10^(-23)*296)/q0; (* k*T at 296 K / eV *)
Ei = 2.2; (* peak of the Gaussian density of states w.r.t. valence band / eV *)
dE = 0.15; (* variance of the Gaussian density of states / eV *)
Ni = 9*10^12; (* density of interface states / 1/cm^2 *)
Ef = 3.2 - 0.067; (* Fermi energy w.r.t. valence band / eV *)
Xn = 0; (* Fermi level of the neutral interface *)
Nd = 9.0*10^17;  (* density of deep trap states / 1/cm^3 *)
eps0 = 8.854187817*10^-14; (* permittivity of vacuum / F/cm *)
eps1 = 8.81; (* relative permittivity of the material *)
NdFac = 2*q0*Nd*eps0*eps1;
Qp = -1.25*10^-7; (* piezoelectric polarisation charge at the grain boundary *)

(* Fermi Energy *)
Xi[V_?NumericQ] := Ef - kT*Log[2/(1 + Exp[-V/kT])]

(* Interface Charge *)
Qi[V_?NumericQ, phi_?NumericQ] := Ni q0 NIntegrate[E^(-((x-(Ei+phi))^2/dE^2))/
(Sqrt[ \[Pi]] dE (E^((x-Xi(V))/kT)+1)),{x,Xn,(Ei+phi)+8*dE},MaxRecursion->50,
PrecisionGoal->12]
```

```
(* Potential Barrier *)
Phi[V_?NumericQ, qi_?NumericQ, qp_?NumericQ] := ((qi + qp)^2 - NdFac*V)^2/
(4*NdFac*(qi + qp)^2)

(* Voltage Range to Solve For *)
Vmin = 0.1;
Vmax = 10;
Vdel = 0.1;
Vnum = (Vmax - Vmin)/Vdel + 1;
Vval = Table[V, {V, Vmin, Vmax, Vdel}];

(* Definition of Qi Fitting Function *)
fitQi[x_, a_, b_, c_, d_, f_] := Piecewise[{{a + b  Exp[-c x^f], x < d},
{a + b Exp[-c d^f], x >= d}}]

Params[Qp_] := Module[{sol, Psol1, Psol2, Qsol1, Qsol2, VCsol1, VCsol2},

(* Self-Consistent solution for V>0 *)
sol = Table[RootSearch[phi == Phi[V, Qi[V, phi], Qp], {phi, 0, 2}], {V, Vmin,
Vmax, Vdel}];

(* Potential Barrier Solutions *)
Psol1 = Table[sol[[i, 1]][[1, 2]], {i, 1, Vnum}];
Psol2 = Table[sol[[i, 2]][[1, 2]], {i, 1, Vnum}];

(* Interface Charge Solutions *)
Qsol1 = Table[Qi[Vval[[i]], Psol1[[i]]], {i, 1, Vnum}];
Qsol2 = Table[Qi[Vval[[i]], Psol2[[i]]], {i, 1, Vnum}];

(* Breakdown Voltage Solutions *)
VCsol1 = Table[Qsol1[[i]]*Qsol1[[i]]/NdFac, {i, 1, Vnum}];
VCsol2 = Table[Qsol2[[i]]*Qsol2[[i]]/NdFac, {i, 1, Vnum}];
```

```
(* Generation of Qi-Fit *)
FindFit[Table[{Vval[[i]], Qsol1[[i]]}, {i, 1, Vnum}], fitQi[x, a, b, c, d, f],
{a, b, c, d, f}, x, Method -> LevenbergMarquardt, MaxIterations -> 10000]

(* Qp Range to Tabulate the Qi-Fit For *)
Qpmin = -0.00000015;
Qpmax = 0.00000015;
Qpdel = 0.00000005;
Qpnum = (Qpmax - Qpmin)/Qpdel + 1;
Qpval = Table[Qp, {Qp, Qpmin, Qpmax, Qpdel}];

(* Tabulation of Fitting Parameters *)
aa = {};
bb = {};
cc = {};
dd = {};
ff = {};
For[i = 1, i <= Qpnum, i++,
 {
  par = Params[Qpval[[i]]];
  AppendTo[aa, par[[1]][[2]]];
  AppendTo[bb, par[[2]][[2]]];
  AppendTo[cc, par[[3]][[2]]];
  AppendTo[dd, par[[4]][[2]]];
  AppendTo[ff, par[[5]][[2]]]
  }
 ]

(* Parameter Output *)
aa
bb
cc
dd
ee
ff
```

A.2 Code for the Calculation of the Polarisation Normal to Each Grain Boundary

The following script was written in Python 2.7. It takes as input the local stress state in each grain (as output by the Elmer FEM program [109]), the orientation of each grain and the orientation of each grain boundary normal. It then calculates the piezoelectric polarisation charge at each grain boundary, for each grain, according to (3.3.1).

```
import sys, getopt, re, argparse, random, linecache
import numpy as np
from pprint import pprint
from collections import OrderedDict

print "\n###################################"
print "# Polarisation Vector Extractor #"
print "###################################\n"

# The script takes one argument: -b <number of grains>
def main(argv):
 inputfile = ''
 outputfile =''
 try:
  opts, args = getopt.getopt(argv,"hb:",["bodies="])
 except getopt.GetopError:
  print 'polarisation.py -b <bodynumber>'
  sys.exit(2)
 for opt, arg in opts:
  if opt == '-h':
   print 'polarisation.py -b <bodynumber>'
   sys.exit()
  elif opt in ("-b", "--bodies"):
   bodynumber = arg
 print 'Number of Bodies:', bodynumber
if __name__ == "__main__":
 main(sys.argv[1:])
output = open('polarisation.txt', 'w')
body = 1
```

```
bodynumber = float(sys.argv[2])

# Loop through the set of files with the local stress for each grain.
while body <= bodynumber:
 with open('body%d.dat' % body) as f:
  for line in f:
   numbers_float = map(float, line.split())
   stressxx = (0.0001*numbers_float[0])
   stressyy = (0.0001*numbers_float[1])
   stresszz = (0.0001*numbers_float[2])
   stressxy = (0.0001*numbers_float[3])
   stressxz = (0.0001*numbers_float[4])
   stressyz = (0.0001*numbers_float[5])
   StressVector = np.matrix([[stressxx], [stressyy], [stresszz], [stressyz],
[stressxz], [stressxy]])
# Define the piezoelectric stress tensor.
   d31 = -5.43*(10**(-12))
   d33 = 11.67*(10**-(12))
   d15 = -11.34*(10**(-12))
   dMatrix = np.matrix([[0, 0, 0, 0, d15, 0], [0, 0, 0, d15, 0, 0], [d31, d31,
d33, 0, 0, 0]])
# Get the grain orientation.
 with open('python_rot.txt', 'r') as orientations:
  line_orientations = orientations.readlines()
  orientations.seek(0)
  for line in orientations:
   if line == '%s\n' % body:
    orients_str = line.split()
    if int(orients_str[0]) == int(body):
     orientation_line = line_orientations.index('%s\n' % body)
     tensor_line = (orientation_line + 1)
     if tensor_line == int(orientation_line + 1):
      tensor_entry = linecache.getline('python_rot.txt', (tensor_line + 1))
      tensor_str = tensor_entry.split()
      rxx = float(tensor_str[0])
```

```
      rxy = float(tensor_str[1])
      rxz = float(tensor_str[2])
      tensor_line += 1
      if tensor_line == (orientation_line + 2):
       tensor_entry = linecache.getline('python_rot.txt', (tensor_line + 1))
       tensor_str = tensor_entry.split()
       ryx = float(tensor_str[0])
       ryy = float(tensor_str[1])
       ryz = float(tensor_str[2])
       tensor_line += 1
       if tensor_line == (orientation_line + 3):
        tensor_entry = linecache.getline('python_rot.txt', (tensor_line + 1))
        tensor_str = tensor_entry.split()
        rzx = float(tensor_str[0])
        rzy = float(tensor_str[1])
        rzz = float(tensor_str[2])
        RM = np.matrix([[rxx, rxy, rxz], [ryx, ryy, ryz], [rzx, rzy, rzz]])
        dR = np.dot(RM,dMatrix)
        PVector = np.dot(dR,StressVector)
# Get the grain boundary orientation.
 with open('grains.dat', 'r') as grains:
  line_number = grains.readlines()
  grains.seek(0)
  for line in grains:
# Skip empty lines.
   if line != "\n":
    lines = re.sub('[:]','', line)
    numbers_str = lines.split()
    if numbers_str[0] == 'Grain':
     numbers_str[1] = float(numbers_str[1])
# If the grain is correct, get the grain boundary normal.
     if numbers_str[1] == body:
      number_of_boundaries = float(numbers_str[2])
      grain_line = line_number.index('Grain %s: %s\n' % (body, numbers_str[2]))
      boundary_line = (grain_line + 2)
```

```
# Repeat for all grain boundaries for this grain.
      while boundary_line < (grain_line + number_of_boundaries + 1):
       boundary = linecache.getline('grains.dat', boundary_line)
       boundary_cleaned = re.sub('[:]','', boundary)
       boundary_str = boundary_cleaned.split()
       normal_x = float(boundary_str[3])
       normal_y = float(boundary_str[4])
       normal_z = float(boundary_str[5])
       NVector = np.matrix([normal_x, normal_y, normal_z])
# Get the polarisation normal to the grain boundary.
       Polarisation = np.dot(NVector,PVector)
# Write the grain, grain boundary and polarisation to the output file.
       print >>output,"Grain",int(numbers_str[1]),"Boundary",boundary_str[1],
Polarisation
       boundary_line += 1
# When the last grain boundary is reached, move to the next grain and repeat.
      else:
       if boundary_line == (grain_line + number_of_boundaries + 1):
        boundary = linecache.getline('grains.dat', boundary_line)
        boundary_cleaned = re.sub('[:]','', boundary)
        boundary_str = boundary_cleaned.split()
        normal_x = float(boundary_str[3])
        normal_y = float(boundary_str[4])
        normal_z = float(boundary_str[5])
        NVector = np.matrix([normal_x, normal_y, normal_z])
        Polarisation = np.dot(NVector,PVector)
        print >>output,"Grain",int(numbers_str[1]),"Boundary",boundary_str[1],
Polarisation
        body += 1
        if body <= bodynumber:
         with open('body%d.dat' % body) as f:
          for line in f:
           numbers_float = map(float, line.split())
           stressxx = (0.0001*numbers_float[0])
           stressyy = (0.0001*numbers_float[1])
```

```
            stresszz = (0.0001*numbers_float[2])
            stressxy = (0.0001*numbers_float[3])
            stressxz = (0.0001*numbers_float[4])
            stressyz = (0.0001*numbers_float[5])
            StressVector = np.matrix([[stressxx], [stressyy], [stresszz],
[stressyz], [stressxz], [stressxy]])
            d31 = -5.43*(10**(-12))
            d33 = 11.67*(10**-(12))
            d15 = -11.34*(10**(-12))
            dMatrix = np.matrix([[0, 0, 0, 0, d15, 0], [0, 0, 0, d15, 0, 0],
[d31, d31, d33, 0, 0, 0]])
          with open('python_rot.txt', 'r') as orientations:
           line_orientations = orientations.readlines()
           orientations.seek(0)
           for line in orientations:
            if line == '%s\n' % body:
             orients_str = line.split()
             if int(orients_str[0]) == int(body):
              orientation_line = line_orientations.index('%s\n' % body)
              tensor_line = (orientation_line + 1)
              if tensor_line == int(orientation_line + 1):
               tensor_entry = linecache.getline('python_rot.txt', (tensor_line
+ 1))
               tensor_str = tensor_entry.split()
               rxx = float(tensor_str[0])
               rxy = float(tensor_str[1])
               rxz = float(tensor_str[2])
               tensor_line += 1
               if tensor_line == (orientation_line + 2):
                tensor_entry = linecache.getline('python_rot.txt', (tensor_line
+ 1))
                tensor_str = tensor_entry.split()
                ryx = float(tensor_str[0])
                ryy = float(tensor_str[1])
                ryz = float(tensor_str[2])
```

```
                tensor_line += 1
                if tensor_line == (orientation_line + 3):
                 tensor_entry = linecache.getline('python_rot.txt', (tensor_line
+ 1))
                 tensor_str = tensor_entry.split()
                 rzx = float(tensor_str[0])
                 rzy = float(tensor_str[1])
                 rzz = float(tensor_str[2])
                 RM = np.matrix([[rxx, rxy, rxz], [ryx, ryy, ryz], [rzx, rzy,
rzz]])
                 dR = np.dot(RM,dMatrix)
                 PVector = np.dot(dR,StressVector)
else:
 print("Done!")
```

A.3 Code for the Calculation of the Polarisation Jump Across Each Grain Boundary

The following script was written in Python 2.7. It takes as input the piezoelectric polarisation charge at each grain boundary, for each grain, (as output by the script in Appendix A.2) and produces the jump in polarisation across each grain boundary, according to (3.3.8).

```
import sys, getopt, re, itertools, csv, pprint, os
import numpy as np

print "\n################################"
print "# Polarisation Jump Calculator #"
print "################################\n"

# The script takes one argument: -b <number of grain boundaries>
def main(argv):
 inputfile = ''
 outputfile =''
 try:
  opts, args = getopt.getopt(argv,"hb:",["boundaries="])
 except getopt.GetopError:
  print 'jump.py -b <boundarynumber>'
```

```
  sys.exit(2)
 for opt, arg in opts:
  if opt == '-h':
   print 'jump.py -b <boundarynumber>'
   sys.exit()
  elif opt in ("-b", "--boundaries"):
   boundarynumber = arg
 print 'Number of Boundaries:', boundarynumber
if __name__ == "__main__":
 main(sys.argv[1:])
boundarynumber = float(sys.argv[2])

# Cleans up the output from the polarisation script.
input2 = open('polarisation2.txt', 'w')
with open('polarisation.txt') as polarisation:
 for line in polarisation:
  line_cleaned = re.sub('[\[\]]','', line)
  content = " ".join(line_cleaned.split())
  line_split = content.split()
  print >>input2,line_split[3],line_split[4]
input2.close()

# Sorts the polarisation values by grain boundary.
input3 = open('polarisation3.txt', 'w')
with open("polarisation2.txt","r") as polarisation2:
 data = polarisation2.readlines()
 data_sorted = sorted(data, key=lambda l: float(l.split(" ")[0]))
 print >>input3,"\n".join(data_sorted)
input3.close()

# Removes gaps from polarisation3.
input4 = open('polarisation4.txt', 'w')
with open('polarisation3.txt', 'r') as polarisation3:
 for line in polarisation3:
  if not line.isspace():
```

```
   input4.write(line)
input4.close()

# Calculates the jump in polarisation across the grain boundary.
output = open('jumps.txt', 'w')
boundary = 1
with open('polarisation4.txt', 'r') as polarisation4:
 prevLine = ""
 Pprev = ""
 prevBoundary = ""
 for line in polarisation4:
  numbers_str = line.split()
  boundaryNow = int(numbers_str[0])
  P = float(numbers_str[1])
  if boundaryNow == prevBoundary:
   jump = P + Pprev
   print >>output,boundaryNow,jump
   prevLine = line
   Pprev = P
   prevBoundary = boundaryNow
   boundary += 1
  else:
   prevLine = line
   Pprev = P
   prevBoundary = boundaryNow
output.close()
print "Done!"
```

A.4 Code for the Writing of LTspice Sub-Circuit Files for Each Grain Boundary

The following script was written in Python 2.7. It takes as input the jump in polarisation across each grain boundary (as output by the script in Appendix A.3) and produces an LTspice sub-circuit file for each grain boundary.

```
import sys, getopt, re, itertools, csv, pprint, os, math
import numpy as np
```

```
print "\n################################"
print "# Spice Sub Circuit Generator #"
print "################################\n"

# The script takes one argument: -b <number of grain boundaries>
def main(argv):
 inputfile = ''
 outputfile =''
 try:
  opts, args = getopt.getopt(argv,"hb:",["boundaries="])
 except getopt.GetopError:
  print 'bounds.py -b <boundarynumber>'
  sys.exit(2)
 for opt, arg in opts:
  if opt == '-h':
   print 'bounds.py -b <boundarynumber>'
   sys.exit()
  elif opt in ("-b", "--boundaries"):
   boundarynumber = arg
 print 'Number of Boundaries:', boundarynumber
if __name__ == "__main__":
 main(sys.argv[1:])
boundarynumber = float(sys.argv[2])
line_number = 1
input = open('jumps.txt', 'r')

# Writes one grain boundary sub-circuit file for every line in the input file.
for line in input:
 jumps_str = line.split()
 jump = jumps_str[0]
 polarisation = float(jumps_str[1])
 with open('BOUND%d.lib' % line_number, 'w') as BOUND:
  print >>BOUND,'.SUBCKT BOUND%(line_number)d 1 2\n.param Rich={30}\n.param
E_f={0.067}\n.param Qp={%(polarisation)s}\n.param N_t={0.9e13}\n.param
N_d={0.9e18}\n.param q={1.6e-19}\n.param epsilon={8.81*8.85e-14}\n.param
```

```
Ndfac={2*epsilon*N_d*q}\n.param T={296}\n.param kB={8.617e-5}\n.param
R_G={1/(2*pow(Area,0.5))}\n.func a(Qp0)=table{Qp0,-2.42e-7,1.54057e-6,-1.88e-7,
1.56889e-6,-1.25e-7,1.63095e-6,-0.63e-7,1.65212e-6,0,1.71531e-6,0.63e-7,
1.76403e-6,1.25e-7,1.82157e-6,1.88e-7,1.86703e-6,2.42e-7,1.91574e-6,2.51e-7,
1.92473e-6,3.13e-7,1.99006e-6,3.76e-7,2.04345e-6,5.01e-7,2.17885e-6}\n.func
b(Qp0)=table{Qp0,-2.42e-7,-4.26063e-7,-1.88e-7,-5.02508e-7,-1.25e-7,
-6.23019e-7,-0.63e-7,-6.99271e-7,0,-8.21114e-7,0.63e-7,-9.27738e-7,1.25e-7,
-1.04277e-6,1.88e-7,-1.14611e-6,2.42e-7,-1.24484e-6,2.51e-7,-1.26219e-6,
3.13e-7,-1.38523e-6,3.76e-7,-1.49666e-6,5.01e-7,-1.74768e-6}\n.func
c(Qp0)=table{Qp0,-2.42e-7,0.534161,-1.88e-7,0.438088,-1.25e-7,0.343845,
-0.63e-7,0.299191,0,0.251506,0.63e-7,0.219898,1.25e-7,0.194121,1.88e-7,
0.175022,2.42e-7,0.160363,2.51e-7,0.158068,3.13e-7,0.143607,3.76e-7,0.132204,
5.01e-7,0.112636}\n.func d(Qp0)=table{Qp0,-2.42e-7,2.43578,-1.88e-7,2.82866,
-1.25e-7,3.29075,-0.63e-7,3.83146,0,4.37507,0.63e-7,4.97234,1.25e-7,5.59233,
1.88e-7,6.26742,2.42e-7,6.86756,2.51e-7,6.96953,3.13e-7,7.68981,3.76e-7,
8.46809,5.01e-7,10.0956}\n.func f(Qp0)=table{Qp0,-2.42e-7,1.1313,-1.88e-7,
1.10012,-1.25e-7,1.04352,-0.63e-7,1.03488,0,0.999042,0.63e-7,0.978774,1.25e-7,
0.957982,1.88e-7,0.944811,2.42e-7,0.931639,2.51e-7,0.929336,3.13e-7,0.913895,
3.76e-7,0.903442,5.01e-7,0.880483}\n.func
Qi(V)=min((a(Qp)+(b(Qp)*exp(-c(Qp)*pow(d(Qp),f(Qp))))),
(a(Qp)+(b(Qp)*exp(-c(Qp)*pow(V,f(Qp))))))\n.func
Phi(V)={pow(pow(Qi(V)+Qp,2)-Ndfac*V,2)/(4*NdFac*pow(Qi(V)+Qp,2))}\n.func
Jdc(V)={Rich*pow(T,2)*exp(-(E_f+Phi(V))/(kB*T))*(1-exp(-V/(kB*T)))}\nR1 1 3
R=R_G/2\nR2 3 4 R=V(3,4)/(Area*10000*Jdc(V(3,4)))\nR3 3 4 R=1000/Area\nR4 4 2
R=R_G/2\n.ENDS' % {"line_number": line_number, "polarisation": polarisation}
  line_number += 1
input.close()
print "Done!"
```

A.5 LTspice Input

A.5.1 Example Grain Boundary Sub-Circuit

The following is an example of an LTspice sub-circuit (as output by the script in Appendix A.4) for a grain boundary in this framework.

```
.SUBCKT BOUNDX 1 2 *Here, X is the grain boundary number.
.param Rich={30} *Richardson constant
.param E_f={0.067} *Fermi energy
.param Qp={0} *Here, the script inserts the calculated value for Qp.
.param N_t={0.9e13} *Density of interface states
.param N_d={0.9e18} *Density of deep trap states
.param q={1.6e-19} *Elementary unit charge
.param epsilon={8.81*8.85e-14} *Permittivity
.param Ndfac={2*epsilon*N_d*q}
.param T={296} *Temperature
.param kB={8.617e-5} *Boltzmann constant
.param R_G={1/(2*pow(Area,0.5))} *Grain bulk resistance
*Tabulation of Qi parameters for Qp
.func a(Qp0)=table{Qp0,-2.42e-7,1.54057e-6,-1.88e-7,1.56889e-6,-1.25e-7,
1.63095e-6,-0.63e-7,1.65212e-6,0,1.71531e-6,0.63e-7,1.76403e-6,1.25e-7,
1.82157e-6,1.88e-7,1.86703e-6,2.42e-7,1.91574e-6,2.51e-7,1.92473e-6,3.13e-7,
1.99006e-6,3.76e-7,2.04345e-6,5.01e-7,2.17885e-6}
.func b(Qp0)=table{Qp0,-2.42e-7,-4.26063e-7,-1.88e-7,-5.02508e-7,-1.25e-7,
-6.23019e-7,-0.63e-7,-6.99271e-7,0,-8.21114e-7,0.63e-7,-9.27738e-7,1.25e-7,
-1.04277e-6,1.88e-7,-1.14611e-6,2.42e-7,-1.24484e-6,2.51e-7,-1.26219e-6,
3.13e-7,-1.38523e-6,3.76e-7,-1.49666e-6,5.01e-7,-1.74768e-6}
.func c(Qp0)=table{Qp0,-2.42e-7,0.534161,-1.88e-7,0.438088,-1.25e-7,0.343845,
-0.63e-7,0.299191,0,0.251506,0.63e-7,0.219898,1.25e-7,0.194121,1.88e-7,
0.175022,2.42e-7,0.160363,2.51e-7,0.158068,3.13e-7,0.143607,3.76e-7,0.132204,
5.01e-7,0.112636}
.func d(Qp0)=table{Qp0,-2.42e-7,2.43578,-1.88e-7,2.82866,-1.25e-7,3.29075,
-0.63e-7,3.83146,0,4.37507,0.63e-7,4.97234,1.25e-7,5.59233,1.88e-7,6.26742,
2.42e-7,6.86756,2.51e-7,6.96953,3.13e-7,7.68981,3.76e-7,8.46809,5.01e-7,
10.0956}
.func f(Qp0)=table{Qp0,-2.42e-7,1.1313,-1.88e-7,1.10012,-1.25e-7,1.04352,
-0.63e-7,1.03488,0,0.999042,0.63e-7,0.978774,1.25e-7,0.957982,1.88e-7,0.944811,
2.42e-7,0.931639,2.51e-7,0.929336,3.13e-7,0.913895,3.76e-7,0.903442,5.01e-7,
0.880483}
 *Solution of Qi
.func Qi(V)=min((a(Qp)+(b(Qp)*exp(-c(Qp)*pow(d(Qp),f(Qp))))),
```

```
(a(Qp)+(b(Qp)*exp(-c(Qp)*pow(V,f(Qp))))))
*Solution of Phi
.func Phi(V)={pow(pow(Qi(V)+Qp,2)-Ndfac*V,2)/(4*NdFac*pow(Qi(V)+Qp,2))}
*Solution of the Richardson-Dushman equation
.func Jdc(V)={Rich*pow(T,2)*exp(-(E_f+Phi(V))/(kB*T))*(1-exp(-V/(kB*T)))}
*Grain Boundary Equivalent Electrical Circuit
R1 1 3 R=R_G/2 *Grain Resistance
R2 3 4 R=V(3,4)/(Area*10000*Jdc(V(3,4))) *Non-Linear Resistance
R3 3 4 R=1000/Area *Leakage Resistance
R4 4 2 R=R_G/2 *Grain Resistance
.ENDS
```

A.5.2 Netlist Excerpt for the Equivalent Electrical Network of a Varistor

The following is an excerpt from an LTspice netlist for a polycrystalline varistor in this framework. It requires the set of sub-circuit files produced by the script in Appendix A.4.

```
Varistor

v1 potential 0 dc 100 *Voltage range to simulate for.
X1 1 164 BOUND1 Area=1.149453408015e-12 *Netlist connections describing the
X2 1 224 BOUND2 Area=1.754505076673e-12 *equivalent electrical network.
X3 1 311 BOUND3 Area=1.436298962316e-11
*.
*. The netlist is very long and is skipped here for brevity.
*.
X1743 563 0 BOUND0 Area=3.826753000000e-12
X1744 potential 565 BOUND0 Area=9.075624000000e-12
X1745 potential 573 BOUND0 Area=8.915800000000e-14

.options plotwinsize=0
.options numdgt=7
.options gmin=1e-60
.options itl1 1000
.options itl2 1000
```

```
.dc dec v1 0.1 100 *This option steps the voltage logarithmically, which allows
for a finer resolution of the IV-curve at low voltages.
*.dc v1 0 100 0.5 *This option steps the voltage linearly, which is necessary
for the tool that produces the current flow maps.
.inc BOUND0.lib *List of sub-circuit files to include.
.inc BOUND1.lib
.inc BOUND2.lib
*.
*. The list of sub-circuits is very long and is skipped here for brevity.
*.
.inc BOUND1743.lib
.inc BOUND1744.lib
.inc BOUND1745.lib
.end
```

A.5.3 Sub-Circuit for the External Electrical Contacts

The electrical contacts at the top and bottom of the sample are defined by the sub-circuit `BOUND0`, which appears below.

```
.SUBCKT BOUND0 1 2
.param R_G={1/(2*pow(Area,0.5))}
R1 1 2 R=R_G/2 *Grain Resistance
.ENDS
```

A.5.4 Sub-Circuit for an Ohmic Grain Boundary

The Ohmic grain boundaries described in Section 5.2 are defined by the sub-circuit `BOUNDOHMIC`, which appears below.

```
.SUBCKT BOUNDOHMIC 1 2
.param R_G={1/(2*pow(Area,0.5))}
R1 1 3 R=R_G/2 *Grain Resistance
R2 3 4 R=1/(Area*1000) *Ohmic Resistance
R3 4 2 R=R_G/2 *Grain Resistance
.ENDS
```

A.6 Transformation Matrices

The matrix R represents the relationship between two coordinate systems, where R_R is obtained by multiplying the matrices for the three basic rotations around each of the Cartesian coordinate axes [116]. This appears as follows,

$$\begin{aligned} R_R &= R_z(\psi)R_y(\theta)R_x(\phi) \\ &= \begin{bmatrix} \cos\psi & -\sin\psi & 0 \\ \sin\psi & \cos\psi & 0 \\ 0 & 0 & 1 \end{bmatrix} \begin{bmatrix} \cos\theta & 0 & -\sin\theta \\ 0 & 1 & 0 \\ \sin\theta & 0 & \cos\theta \end{bmatrix} \begin{bmatrix} 1 & 0 & 0 \\ 0 & \cos\phi & -\sin\phi \\ 0 & \sin\phi & \cos\phi \end{bmatrix} \\ &= \begin{bmatrix} \cos\psi\cos\theta & \cos\psi\sin\theta\sin\phi - \sin\psi\cos\phi & \cos\psi\sin\theta\cos\phi + \sin\psi\sin\phi \\ \sin\psi\cos\theta & \sin\psi\sin\theta\sin\phi + \cos\psi\cos\phi & \sin\alpha\sin\theta\cos\phi - \cos\alpha\sin\phi \\ -\sin\theta & \cos\theta\sin\phi & \cos\theta\cos\phi \end{bmatrix} \\ &= \begin{bmatrix} l_1 & m_l & n_1 \\ l_2 & m_2 & n_2 \\ l_3 & m_3 & n_3 \end{bmatrix}, \end{aligned} \tag{A.6.1}$$

where ϕ is the Euler angle rotating about the x-axis, θ is the Euler angle rotating about the y-axis, and ψ is the Euler angle rotating about the z-axis.

In order to apply a coordinate transformation to fourth rank tensors, the transformation matrix, α_T, is required [116], where

$$\alpha_T = \begin{bmatrix} l_1^2 & m_1^2 & n_1^2 & 2m_1n_1 & 2n_1l_1 & 2l_1m_1 \\ l_2^2 & m_2^2 & n_2^2 & 2m_2n_2 & 2n_2l_2 & 2l_2m_2 \\ l_3^2 & m_3^2 & n_3^2 & 2m_3n_3 & 2n_3l_3 & 2l_3m_3 \\ l_2l_3 & m_2m_3 & n_2n_3 & m_2n_3 + m_3n_2 & n_2l_3 + n_3l_2 & m_2l_3 + m_3l_2 \\ l_3l_1 & m_3m_1 & n_3n_1 & m_3n_1 + m_1n_3 & n_3l_1 + n_1l_3 & m_3l_1 + m_1l_3 \\ l_1l_2 & m_1m_2 & n_1n_2 & m_1n_2 + m_2n_1 & n_1l_2 + n_2l_1 & m_1l_2 + m_2l_1 \end{bmatrix}. \tag{A.6.2}$$

When a fourth rank tensor is expressed as a matrix in Voigt notation, it is transformed by

$$C_T = \alpha_T C \alpha_T^{-1}, \tag{A.6.3}$$

where C_T is the transformed matrix, α_T is the transformation matrix, C is the matrix to be transformed and α_T^{-1} is the inverse of the transformation matrix.

Bibliography

[1] X. W. Sun, and H. S. Kwok, *Optical Properties of Epitaxially Grown Zinc Oxide Films on Sapphire by Pulsed Laser Deposition*, J. Appl. Phys., 86, 408, 1999.

[2] Z. G. Ju, C. X. Shan, D. Y. Jiang, J. Y. Zhang, B. Yao, D. X. Zhao, D. Z. Shen, and X. W. Fan, *Mg_xZn_{1-x}-based Photodetectors Covering the Whole Solar-Blind Spectrum Range*, Appl. Phys. Lett., 93, 173505, 2008.

[3] K. Ellmer, A. Klein and B. Rech, *Transparent Conductive Zinc Oxide*, Springer, 2008.

[4] T. K. Gupta, *Application of Zinc Oxide Varistors*, J. Am. Ceram. Soc., 73, 1817-1840, 1990.

[5] G. Ringler, P. Kirby, C. C. Erven, M. V. Lat and T. A. Malkiewicz, *The Energy Absorption Capability and Time-to-Failure of Varistors Used in Station Class Metal-Oxide Surge Arrestors*, IEEE Trans. Power Delivery, 12, 203-212, 1997.

[6] L. K. J. Vanadamme and J. C. Brugman, *Conduction Mechanisms in ZnO Varistors*, J. Appl. Phys., 51, 4240, 1980.

[7] A. Vojta and D. R. Clarke, *Microstructural Origin of Current Localization and Puncture Failure in Varistor Ceramics*, J. Appl. Phys, 81, 985, 1997.

[8] ABB Switzerland Ltd., *Overvoltage Protection, Metal Oxide Surge Arresters in Medium Voltage Systems - Application Guidelines*, 5th Edition, 2011.

[9] J. Zhou, Y. Gu, P. Fei, W. Mai, Y. Gao, R. Yang, G. Bao and Z.-L. Wang, *Flexible Piezotronic Strain Sensor*, Nano Lett. 8, 3035-3040, 2008.

[10] P. Keil, M. Trapp, N. Novak, T. Frömling, H.-J. Kleebe and J. Rödel, *Piezotronic Tuning of Potential Barriers in ZnO Bicrystals*, Adv Mater, 1705573, 2018.

[11] J. He, *Metal Oxide Varistors - From Microstructure to Macro-Characteristics*, John Wiley & Sons, 2019.

[12] Y. Purusothaman, N. Alluri, C. Arunkumar, V. Vivekananthanand, S. J. Kim, *Regulation of Charge Carrier Dynamics in ZnO Microarchitecture-Based UV/Visible Photodetector via Photonic-Strain Induced Effects*, Small, 01, 1703044, 2018.

[13] W. Han, Y. Zhou, Y. Zhang, C. Y. Chen, L. Lin, X. Wang, S. Wang and Z. L. Wang, *Strain-Gated Piezotronic Transistors Based on Vertical Zinc Oxide Nanowires*, ACS Nano, 6, 3760-3766, 2012.

[14] W. Zhang, R. Zhu, V. Nguyen and R. Yang, *Highly Sensitive and Flexible Strain Sensors Based on Vertical Zinc Oxide Nanowire Arrays*, Sensors and Actuators, A: Physical, 205, 164-169, 2014.

[15] R. Baraki, N. Novak, T. Frömling, T. Granzow and J. Rödel, *Bulk ZnO as Piezotronic Pressure Sensor*, Applied Physics Letters, 105, 111604, 2014.

[16] P. Keil, R. Baraki, N. Novak, J. Rödel and T. Frömling, *Gauge Factors for Piezotronic Stress Sensor in Polycrystalline ZnO*, J. Phys. D: Appl. Phys., 50, 175106, 2017.

[17] Z.-Q. Zhou, K. Taylor, E. Gjonaj, T. Frömling and B.-X. Xu, *Finite Element Simulations on Piezoelectric Modulation of ZnO Grain Boundary Barrier Height*, J. Appl. Phys, 126, 205101, 2019.

[18] P. M. Verghese and D. R. Clarke, *Piezoelectric Contributions to the Electrical Behaviour of ZnO Varistors*, J. Appl. Phys., 87, 4430, 2000.

[19] R. Baraki, N. Novak, M. Hofstätter, P. Supancic, J. Rödel and T. Frömling, *Varistor Piezotronics: Mechanically Tuned Conductivity in Varistors*, J. Appl. Phys., 118, 85703, 2015.

[20] N. Raidl, P. Supancic, R. Danzer and M. Hofstätter, *Piezotronically Modified Double Schottky Barriers in ZnO Varistors*, Adv Mater, 27, 2031-2035, 2015.

[21] P. Keil, M. Gehringer, T. Frömling, N. Novak and J. Rödel, *ZnO-Based Single Crystal-Polycrystal Structures for Piezotronic Applications*, J. Am. Ceram. Soc., 102, 2640-2647, 2019.

[22] M. Bartkowiak and G. D. Mahan, *Nonlinear Currents in Voronoi Networks*, Phys. Rev. B, 51, 10825-10832, 1995.

[23] K. Bavelis, E. Gjonaj and T. Weiland, *Modeling of Electrical Transport in Zinc Oxide Varistors*, Adv. Radio Sci., 12, 29-34, 2014.

[24] A. Vojta, Q. Wen and D. R. Clarke, *Influence of Microstructural Disorder on the Current Transport Behavior of Varistor Ceramics*, Comp. Mater. Sci., 6, 51-62, 1996.

[25] D. R. Clarke, *Varistor Ceramics* J. Am. Ceram. Soc. 82, 485-502, 1999.

[26] D. J. Scott, P. V. Coveney, J. A. Kilner, J. C. H. Rossiny and N. Mc N. Alford, *Prediction of the Functional Properties of Ceramic Materials from Composition using Artificial Neural Networks*, J. Eur. Cer. Soc., 27, 4425-4435, 2007.

[27] Y. Späck-Leigsnering, *Electrothermal Modeling, Simulation and Optimization of Surge Arresters*, TU Darmstadt, 2019.

[28] F. Greuter, R. S. Perkins, M. Rossinelli and F. Schmückle, *The Metal-Oxide Resistor - At the Heart of Modern Surge Arresters*, ABB Review, 1, 1, 1989.

[29] R. S. Perkins, *The Impact of Metal Oxide Disk Performance on Surge Arrester Operation*, Proc. World Conf. and Exhibition on Insulators, Arresters and Bushings, 193, 2003.

[30] Wikimedia Commons, *Crystal structure of ZnO (wurtzite) with coordination polyhedra*, 2008.

[31] C. G. Van de Walle, *Hydrogen as a Cause of Doping in Zinc Oxide*, Phys. Rev. Lett., 85, 1012-1015, 2000.

[32] D. C. Look, G. C. Farlow, P. Reunchan, S. Limpijumnong, S. B. Zhang and K. Nordlund, *Evidence for Native-Defect Donors in n-Type ZnO*, Phys. Rev. Lett., 95, 225502, 2005.

[33] V. Srikant and D. R. Clarke, *On the Optical Band Gap of Zinc Oxide*, J. Appl. Phys., 85, 5447, 1998.

[34] W. Heywang, K. Lubitz and W. Wersing, *Piezoelectricity: Evolution and Future of a Technology*, Springer, 2008.

[35] B. Jaffe, W. R. Cook and H. L. Jaffe, *Piezoelectric Ceramics*, Academic Press, 1971.

[36] C. Wood and D. Jena, *Polarization Effects in Semiconductor: From Ab Initio Theory to Device Applications*, Springer, 2007.

[37] K. Eda, *Progress in Fabrication Technology of Zinc Oxide Varistors*, Advances in Varistor Technology, 10-21, 1988.

[38] F. Stucki and F. Greuter, *Key Role of Oxygen at Zinc Oxide Varistor Grain Boundaries*, Appl. Phys. Lett., 57, 446-448, 1990.

[39] J. Wong, *Sintering and Varistor Characteristics of ZnO-Bi_2O_3 Ceramics*, J. Appl. Phys., 51, 4453-4459, 1980.

[40] H. Schaumburg, *Werkstoffe und Bauelemente der Elektrotechnik, Keramik*, Teubner, Stuttgart, 5th Edition, 1994

[41] T. Klein, *Einflüsse auf das Energieaufnahmevermögen von Metalloxidableitern*, Dissertation, Universität Stuttgart, 2004.

[42] T. Asokan, G. R. Nagabhushana and G. Iyengar, *Improvement of Non-Linear Characteristics of Multicomponent ZnO-Based Ceramics Containing Nb_2O_5*, IEEE Transactions on Electrical Insulation, 23, 279-286, 1988.

[43] Y. M. Chiang, H.Wang and J. R. Lee, *HREM and STEM of Intergranular Films at Zinc-Oxide Varistor Grain-Boundaries*, J. of Microscopy, 191, 275-285, 1998.

[44] H. Wang and Y. M. Chiang, *Thermodynamic Stability of Intergranular Amorphous Films in Bismuth-Doped Zinc Oxide*, J. Am. Ceram. Soc., 81, 89-96, 1998.

[45] K. I. Kobayashi, O. Wada, M. Kobayashi and Y. Takada, *Continuous Existence of Bismuth at Grain Boundaries of Zinc Oxide Varistor without Intergranular Phase*, J. Am. Ceram. Soc., 81, 2071-2076, 1998.

[46] Y. Sato, T. Yamamoto and Y. Ikuhara, *Atomic Structures and Electrical Properties of ZnO Grain Boundaries*, J. Am. Ceram. Soc., 90, 337-357, 2007.

[47] F. Stucki, P. Brüsch and F. Greuter, *Electron Spectroscopic Studies of Electrically Active Grain Boundaries in ZnO*, Surf. Sci., 189/190, 294-299, 1987.

[48] M. Elfwing and E. Olsson, *Nanoscale Characterisation of Barriers to Electron Conduction in ZnO Varistor Materials*, Uppsala Dissertations, Faculty of Science and Techn., 686, 2002.

[49] T. D. Chen, J. R. Lee, H. L. Tuller and Y. M. Chiang, *Grain Boundary Dopant and Heat Treatment Effects on the Electrical Properties of Polycrystalline ZnO*, Mat. Res. Soc. Symp. Proc., 411, 295-300, 1996.

[50] H. L. Tuller, *ZnO Grain Boundaries: Electrical Activity and Diffusion*, J. Electroceram., 4, 33-40, 1999.

[51] S. Bernik, M. Podlogar, N. Daneu and A. Recnik, *Tailoring the Microstructure of ZnO-Based Ceramics*, Materials and Technology, 42, 69-77, 2008.

[52] F. A. Selim, T. K. Gupta. P. L. Hower, and W. G. Carlson, *Low-Voltage ZnO Varistor: Device Process and Defect Model*, J. Appl. Phys., 51, 765-768, 1980.

[53] M. Matsuoka, *Non-Ohmic Properties of Zinc Oxide Ceramics*, Jpn. J. Appl. Phys., 10, 736-46, 1971.

[54] L. M. Levinson, *Advances in Varistor Technology*, American Ceramics Society Ceramic Transactions, 3, 1989.

[55] A. C .Caballero, D. Fernández Hevia, J. de Frutos, M. Peiteado and J. F. Fernández, *Bulk Grain Resistivity of ZnO-Based Varistors*, J. Electroceramics, 13, 759-763, 2004.

[56] P. R. Bueno, J. A. Varela and E. Longo, *SnO_2, ZnO and Related Polycrystalline Compound Semiconductors: An Overview and Review on the Voltage-Dependent Resistance (Non-Ohmic) Feature*, J. Eur. Ceramic Soc., 28, 505-529, 2008.

[57] F. Greuter, G. Blatter, *Electrical Properties of Grain Boundaries in Polycrystalline Compound Semiconductors*, Semicond. Sci. Technol., 5, 111-137, 1990.

[58] G. Blatter and F. Greuter, *Carrier Transport Through Grain Boundaries in Semiconductors*, Phys. Rev. B, 33, 3952-3966, 1986.

[59] G. E. Pike, *Electronic Properties of ZnO Varistors: A New Model*, Mater. Res. Soc. Symp. Proc., 5, 369, 1982.

[60] G. E. Pike, *Semiconductor Grain-Boundary Admittance: Theory*, Phys. Rev. B, 30, 795, 1984.

[61] G. Blatter and F. Greuter, *Electrical Breakdown at Semiconductor Grain Boundaries*, Phys. Rev. B, 34, 8555, 1986.

[62] G. Blatter and D. Baeriswyl, *High-Field Transport Phenomenology: Hot-Electron Generation at Semiconductor Interfaces*, Phys. Rev. B, 36, 6446, 1987.

[63] G. E. Pike, S. R. Kurtz, and P. L. Gourley, *Electroluminescence in ZnO Varistors: Evidence for Hole Contributions to the Breakdown Mechanism*, J. Appl. Phys., 57, 5512, 1985.

[64] G. E. Pike, *Comment on 'Conduction Mechanisms and Temperature Dependence of the electroluminescence in ZnO Varistors'*, Semicond. Sci. Technol., 3, 191, 1988.

[65] M. Rossinelli, G. Blatter and F. Greuter, *Grain Boundary Properties of ZnO Varistors*, Br. Ceram. Proc., 36, 1-17, 1985.

[66] F. Greuter, T. Christen and J. Glatz-Reichenbach, *Current Flow and Structural Inhomogeneities in Nonlinear Materials*, Mat. Res. Soc. Symp. Proc., 500, 235, 1998.

[67] A. Cornet, A. Miralles, O. Ruiz and J. R. Morante, *Near Infrared Photoluminescence of ZnO:Co Varistors*, Phys. Stat. Sol. A, 120, 105, 1990.

[68] A. Miralles, A. Cornet and J. R. Morante, *Conduction Mechanisms and Temperature Dependence of the Electroluminescence in ZnO Varistors*, Semicond. Sci. Technol., 1, 230, 1986.

[69] H. Wang, M. Bartkowiak, F. Modine, R. B. Dinwiddie, L. A. Boatner and G. D. Mahan, *Nonuniform Heating in Zinc Oxide Varistors Studied by Infrared Imaging and Computer Simulation*, J. Am. Ceram. Soc., 81, 2013-2022, 1998.

[70] F. A. Modine and H. Wang, *Influence of Ceramic Microstructure on Varistor Electrical Properties*, Dielectric Ceramic Materials Ceramic Transactions, 100, 469-491, 1999.

[71] F. Greuter, G. Blatter, M. Rossinelli and F. Schmückle, *Bulk and Grain Boundary Defects in Polycrystalline ZnO*, Mater. Sci. Forum, 10-12, 235-240, 1986.

[72] F. Greuter, *Electrically Active Interfaces in ZnO Varistors*, Solid State Ionics, 75, 67-78, 1995.

[73] G. D. Mahan, *Intrinsic Defects in ZnO Varistors*, J. Appl. Phys., 54, 3825, 1983.

[74] A.F. Kohan, G. Ceder, D. Morgan and C. G. Van de Walle, *First-Principles Study of Native Point Defects in ZnO*, Phys. Rev. B, 61, 15019, 2000.

[75] J. M. Carlsson, B. Hellsing, H. S. Domingos and P. D. Bristowe, *The Effects of Doping a Grain Boundary in ZnO with Various Concentrations of Bi*, Surf. Sci., 532-535, 351-358, 2003.

[76] J. M. Carlsson, H. S. Domingos, P. D. Bristowe and B. Hellsing, *An Interfacial Complex in ZnO and Its Influence on Charge Transport*, Phys. Rev. Letters, 91, 165506, 2003.

[77] H. S. Domingos, J. M. Carlsson, P. D. Bristowe and B. Hellsing, *The Formation of Defect Complexes in a ZnO Grain Boundary*, Interface Sci., 12, 227-234, 2004.

[78] J. G. M. Furtado, R. Dias, F. B. Barbosa, *A Microstructural Analysis of High Voltage Surge Arrester Varistors*, XXII SBMM Congress, 2009.

[79] A. Kobayashi, O. F. Sankey, S. M. Volz and J. D. Dow, *Semiempirical Tight-Binding Band Structures of Wurtzite Semiconductors: AlN, CdS, CdSe, ZnS and ZnO*, Phys. Rev. B, 28, 935-945, 1983.

[80] G. E. Pike and C. H. Seager, *The DC Voltage Dependence of Semiconductor Grain-Boundary Resistance*, J. Appl. Phys., 50, 3414-3422, 1979.

[81] Y. Lu, N. W. Emanetoglu, Y. Chen, C. Jagadish and S. Pearton, *Zinc Oxide Bulk, Thin Films and Nanostructures*, Springer, 2006.

[82] T. K. Gupta, M. P. Mathur and W. G. Carlson, *Effect of Externally Applied Pressure on Zinc Oxide Varistors*, J. Electron. Mater. 6, 483-497, 1977.

[83] J. E. Schoutens and S. L. Senesac, *Effects of Hydrostatic Pressure up to 25 kbars on Zinc Oxide Varistors*, J. Appl. Phys. 50, 6283-6289, 1979.

[84] O. Dorlanne, Bui Ai, P. Destruel and A. Loubiere, *Electrical Characteristics of Zinc Oxide Varistors Subjected to Hydrostatic Pressure*, J. Appl. Phys. 57, 5535-5538, 1985.

[85] M. Bartkowiak, G. D. Mahan, F. A. Modine and M. A. Alim, *Influence of Ohmic Grain Boundaries in ZnO Varistors*, J. Appl. Phys., 79, 273, 1996

[86] M. Bartkowiak, G. D. Mahan, F. A. Modine and M. A. Alim, *Voronoi Network Model of ZnO Varistors with Different Types of Grain Boundaries*, J. Appl. Phys., 80, 6516, 1996

[87] M. Bartkowiak, G. D. Mahan, F. A. Modine and M. A. Alim, *Multiple-Peaked Structure in the Nonlinearity Coefficient of ZnO Varistors*, Jpn. J. Appl. Phys., 35, 414, 1996.

[88] A. Vojta, Q. W. Wen and D. R. Clarke, *Electrical-Impulse-Induced Fracture of Zinc Oxide Varistor Ceramics*, J. Am. Ceram. Soc., 80, 2086-2092, 1997.

[89] C. W. Nan, D. R. Clarke, *Effect of Variations in Grain Size and Grain Boundary Barrier Heights on the Current-Voltage Characteristics of ZnO Varistors*, J. Am. Ceram. Soc., 79, 3185-3192, 1996.

[90] Q. Wen, D. R. Clarke, *Grain Boundaries and Interfacial Phenomena in Electronic Ceramics*, Ceramic Transactions, 41, 217-230, 1994.

[91] Q. Chen, J. He, K. Tan, S. Chen, M. Yan, J. Tang, *Influence of Grain Size on Distribution of Temperature and Thermal Stress in ZnO Varistor Ceramics*, Sci. in China (Series E), 45, 337, 2002.

[92] Y. Tu, L. Ding, J. He, J. Hu and R. Zeng, *Effect of Nonuniformities of Microstructure and Electrical Property of Grain Boundary to the Global Electrical Characteristics*, IEEE proc. 8th Intern. Conf. Prop. and Applic. Dielectr. Mater., 95-98, 2006.

[93] J. He, J. Hu, Y. Tu, L. Ding, S. Han and H. Cho, *Scattered Phenomenon of Energy Absorption Capabilities of ZnO Varistors*, IEEE proc. 8th Intern. Conf. Prop. and Applic. Dielectr. Mater., 335-338, 2006.

[94] Y. Tu, L. Ding, J. He, S. Han and H. Cho, *Dopant Effects to Pores in ZnO Varistors*, IEEE proc. 8th Intern. Conf. Prop. and Applic. Dielectr. Mater., 967-970, 2006.

[95] J. He, J. Hu, Y. Tu, L. Ding, S. Han and H. Cho, *Inhibition Effect of Twins to Grain Growth in ZnO Varistors*, IEEE proc. 8th Intern. Conf. Prop. and Applic. Dielectr. Mater., 971-974, 2006.

[96] J. He, R. Zeng, Q. Chen, S. Chen, Z. Guan, S. Han and H. Cho, *Nonuniformity of Electrical Characteristics in Microstructures of ZnO Surge Varistors*, IEEE Trans. Power Del., 19, 138, 2004.

[97] G. Zhao, R. P. Joshi, V. K. Lakdawala, *Percolative Breakdown Model for Ceramics Based on a Random Grain-Boundary Network*, IEEE 2005 Annual Report Conf. on Electr. Insulation and Dielectric Phenomena, 544-547, 2005.

[98] R. A. Anderson, G. E. Pike, *Current Concentration at Defects in ZnO Varistor Material*, J. Mater. Res., 18, 994, 2003.

[99] S. Boggs, J. Kuang, H. Andoh, S. Nishiwaki, *Electro-Thermal-Mechanical Computations in ZnO Arrester Elements*, IEEE Trans. Power Del., 15, 128-134, 2000.

[100] S. Boggs, J. Kuang, H. Andoh, S. Nishiwaki, *Increased Energy Absorption in ZnO Arrester Elements Through Control of Electrode Edge Margin*, IEEE Trans. Power Del., 15, 562-568, 2000.

[101] R. Quey, P. Dawson and F. Barbe, *Large-Scale 3D Random Polycrystals for the Finite Element Method: Generation, Meshing and Remeshing*, Comput. Methods Appl. Mech. Engrg., 200, 1729-1745, 2011.

[102] Wolfram Research, Inc., *Mathematica*, Version 11.3, Champaign, IL, 2018.

[103] Linear Technology Corporation, *LTspice XVII*, 2016.

[104] M. Tao, A. Bui, O. Dorlanne, and A. Loubiere, *Different "Single Grain Junctions" Within a ZnO Varistor*, J. Appl. Phys. 61, 1562, 1987.

[105] E. Olsson and G. L. Dunlop, *The Microstructure of a ZnO Varistor Material*, J. Appl. Phys. 66, 3666, 1989.

[106] H. Wang, W. Li, and J. F. Cordaro, *Single Junctions in ZnO Varistors Studied by Current-Voltage Characteristics and Deep Level Transient Spectroscopy*, Jpn. J. Appl. Phys. 34, 1765, 1995.

[107] T. Yao and S. Hong, *Oxide and Nitride Semiconductors*, Springer, 2009.

[108] C. Geuzaine and J. F. Remacle, *Gmsh: A Three-Dimensional Finite Element Mesh Generator with Built-In Pre- and Post-Processing Facilities*, International Journal for Numerical Methods in Engineering, 79, 1309-1331, 2009.

[109] M. Malinena and P. Råback, *Elmer Finite Element Solver for Multiphysics and Multiscale Problems*, Multiscale Model. Methods Appl. Mater. Sci., IAS Ser., 19, 101-113, 2013.

[110] K. Sab, *On the Homogenization and the Simulation of Random Materials*, Eur. J. Mech. Solids, 11, 585-607, 1992.

[111] F. Ménil, H. Debéda and C. Lucat, *Screen-Printed Thick-Films: From Materials to Functional Devices*, J. Eur. Ceramic Soc., 25, 2105-2113, 2005.

[112] M. A. de la Rubia López, M. Peiteado, J. F. Fernández, A. C. Caballero, J. Holc, S. Drnovsek, D. Kuscer, S. Macek and M. Kosec, *Thick Film ZnO Based Varistors Prepared by Screen Printing*, J. Eur. Ceramic Soc., 26, 2985-2989, 2006.

[113] T. Mühl, *Einführung in die elektrische Messtechnik: Grundlagen, Messverfahren, Anwendungen*, Springer, 2014.

[114] C.-W. Nan, D. R. Clarke, *Piezoelectric Moduli of Piezoelectric Ceramics*, J. Am. Ceramic Soc. 79, 2563-2566, 1996.

[115] B.-X. Xu, Z.-Q Zhou, P. Keil and T. Frömling, *An Extended Grain Boundary Barrier Height Model Including the Impact of Internal Electric Field*, AIP Advances, 8, 115126, 2018.

[116] M. Bao, *Analysis and Design Principles of MEMS Devices*, Elsevier, 2005.

[117] M. A. Schofield, L. Wu and Y. Zhu, *Quantitative Measurement of Grain Boundary Potentials on the Nanoscale by Off-Axis Electron Holography*, Phys. Rev. B, 67, 224512, 2003.

[118] T.-Y. Wang and C. C.-P. Chen, *SPICE-Compatible Thermal Simulation with Lumped Circuit Modeling for Thermal Reliability Analysis based on Modeling Order Reduction*, Int. Symp. on Signals, Circuits and Systems, SCS Proceedings, 2003.

[119] T. Ersek, *RootSearch looks for all roots of an equation between xmin and xmax*, Wolfram Library Archive, 2006.

List of Figures

Chapter 5.

Chapter 6.

List of Tables

List of Acronyms and Symbols

Acronyms

1D	one-dimensional
2D	two-dimensional
3D	three-dimensional
AC	alternating current
DC	direct current
FEM	finite element method
IV	current-voltage
MOSFET	metal-oxide-semiconductor field-effect transistor
RVE	representative volume element
SC-PC-SC	single crystal-polycrystal-single crystal
SPICE	simulation program with integrated circuit emphasis

Chemical Symbols

Al_2O_3	aluminium oxide
Ag	silver
BeO	beryllium oxide
Bi	bismuth
Bi_2O_3	bismuth oxide
Co	cobalt
CoO	cobalt oxide
Cr_2O_3	chromium oxide
Ga	gallium
GaAs	gallium arsenide
Mn	manganese
MnO	manganese oxide
Nb_2O_5	niobium pentoxide
Ni	nickel

O	oxygen
Pr_6O_{11}	praseodymium oxide
Sb	antimony
Sb_2O_5	antimony oxide
SiO_2	silicon dioxide
SrO	strontium oxide
TiO_2	titanium dioxide
Zn	zinc
ZnO	zinc oxide
U_3O_8	triuranium octoxide

Physical Symbols

a	First Q_i fitting parameter
a_B	grain boundary area
$A*$	Richardson constant
b	Second Q_i fitting parameter
c	Third Q_i fitting parameter
C	Young's modulus or stiffness constant
d	piezoelectric stress constant
d_g	grain size
D	electric flux density
e	piezoelectric strain constant
E_F	Fermi energy
E_i	peak energy of the Gaussian density of states
E_l	electric field on the left side of the grain boundary
E_r	electric field on the right side of the grain boundary
f	inverse piezoelectric scaling factor
f_m	applied force density
ΔE_i	variance of the Gaussian density of states
GF	gauge factor
I	current
I_0	current from the source in the 4-point sensing method
I_V	current through voltmeter in the 4-point sensing method
k_B	Boltzmann constant
l	first column components of the 3D rotation matrix

m	second column components of the 3D rotation matrix
n	third column components of the 3D rotation matrix
n_{gb}	grain boundary normal
N_i	density of interface states
N_{i0}	density of interface states in the absence of a grain boundary potential
N_v	density of the deep trap states
$\tilde{N}_v$	space charge in the depletion layer
p	Fourth Q_i fitting parameter
P	polarisation
P_l	polarisation on the left side of the grain boundary
P_r	polarisation on the right side of the grain boundary
q	elementary unit charge
Q_i	interface charge
$\tilde{Q}_i$	interface charge including both the direct and inverse piezoelectric effects
Q_P	piezoelectric polarisation charge at the grain boundary
Q'_P	piezoelectric polarisation charge at the grain boundary including the inverse piezoelectric effect
R	electrical resistance
R_b	non-linear grain boundary resistance
R_g	grain bulk resistance
R_I	resistance of the contacts attached to the current source in the 4-point sensing method
R_l	leakage resistance
R_R	rotation matrix for a given set of Euler angles
R_V	resistance of the sample in the 4-point sensing method
R_V	resistance of the contacts attached to the voltmeter in the 4-point sensing method
R_x	rotation matrix about the x-axis
R_y	rotation matrix about the y-axis
R_z	rotation matrix about the z-axis
S	deformation or strain
T	temperature
V	voltage
V_B	Fifth Q_i fitting parameter
V_c	critical breakdown voltage
x_{lv}	width of the left depletion layer
x_{rv}	width of the right depletion layer

Greek Symbols

α	non-linearity coefficient
α_T	tensor transformation matrix
β	coefficient of thermal expansion
γ	total charge in the deep trap states
δ	Dirac delta function
ϵ_ν	deep trap energies relative to the conduction band
ϵ_ξ	bulk Fermi level relative to the conduction band
ε	permittivity
ε_r	relative permittivity of the material
ε_0	permittivity of vacuum
θ	Euler angle about the y-axis
Θ	Heaviside step function
λ_g	electrical conductivity of bulk ZnO
λ_l	specific leakage conductivity of the grain boundary
λ_o	specific conductivity of the Ohmic grain boundary surface
ξ_i	quasi Fermi level of the interface
ξ_i^n	Fermi level of the neutral interface
$\rho(x)$	charge distribution
ρ_P	polarisation space charge density
σ	mechanical stress
ϕ	Euler angle about the x-axis
$\phi(x)$	potential
ϕ_B	potential barrier height
ψ	Euler angle about the z-axis

“There is a way out of every box,
a solution to every puzzle;
it’s just a matter of finding it.”

— Captain Jean-Luc Picard

Acknowledgements

I would like to take this opportunity to thank everyone whose professional and personal support made this thesis possible.

First and foremost, I would like to thank PD Dr. rer. nat. Erion Gjonaj, who was the first to offer me the opportunity to pursue a doctoral degree at the Institute for Accelerator Science and Electromagnetic Fields (TEMF). It has been a lifelong dream of mine to earn a doctorate, and this thesis would not have been possible without his constant support and astute critique. In all the time that I have worked with Erion, he has always pushed me to be a better scientist.

I would also especially like to thank Prof. Dr.-Ing Herbert De Gersem for accepting me into his institute and providing a warm and welcoming environment of colleagues. It has been a pleasure to work at TEMF, and this is in no small part thanks to his own open door and candid advice. Thank you for all of your guidance and support along the way.

Another door that has always been open to me throughout my time at TEMF is that of Yun Ouédraogo. Through the good times, and the bad, he has always been available to turn to, and I would like to thank him, my office-mate Steffen Schmid, and all my colleagues at TEMF for their companionship, both professional and personal, over the last three years. A special mention goes to TEMF's extensive network of support staff, who make the work we do here possible: Heike Koch, Dr. phil. nat. Wolfgang Müller, Dragos Munteanu and Achim Wagner. Thank you all for what you do behind the scenes to keep TEMF running.

Furthermore, I would like to thank my extended family here in Germany for their ever present support, especially in the care of my beloved daughter Elisabeth. We simply could not have managed without you.

Finally, and most importantly, I would like to thank my wife, Dr. Nadine Taylor, without whom I would have never made it through my undergraduate degree, let alone all the way to a completed doctoral thesis. Her support and encouragement along the way have been invaluable to me.

Kyle Aaron Taylor
Darmstadt, March 2020